

## ABSTRACT

DALDEGAN PADUANI, VICTOR. Real-Time Modeling and Control of DERs with Advanced Grid-Support Functionalities. (Under the direction of Dr. Ning Lu).

Due to the urgent need to reduce carbon emissions, in recent years, there has been a significant increase in the integration of renewable energies in power systems. Increasing solar and wind generation has environmental benefits; however, these resources impose several challenges for the robust and reliable operation of the grid because of their power output intermittency. To address these issues, this work focuses on the modeling and control of photovoltaic (PV) systems, and on the development of tools that allow the simulation of distribution grids with high number of distributed energy resources (DERs).

In Chapter 2, the modeling and control of a utility-scale PV system is introduced, followed by a power curtailment algorithm for PV systems without power reserves capabilities. The algorithm addresses two weaknesses from available methods: large output power overshoot during irradiance swings, and excessive power output ripple when the power setpoint is higher than the maximum power available.

Chapter 3 introduces a more complex algorithm that includes both fast power setpoint tracking and maximum power point estimation. The method is developed so that the PV can quickly adjust its dispatch while maintaining robust power reserves. The power setpoint tracking is achieved by utilizing information from a non-linear curve fitting technique that is used to extract information from the PV parameters in real-time. Results demonstrate that the algorithm allows PV plants to maintain power reserves for fast frequency response (FFR) applications to increase grid resiliency to disturbances.

In order to properly account for the fast control response and the phase-locked loop performance of inverter-based resources (IBRs), their models must be simulated in the electromagnetic-transient (EMT) domain. However, simulating large grids with many

IBRs in the EMT domain requires excessive computational power, limiting the size of the grid that can be built. To address that issue, in Chapter 4, a modeling architecture is proposed, in which the distribution grid is modeled in the phasor domain, whereas IBRs are modeled in the EMT domain. The testbed can be used to communicate with external energy management systems and allows the implementation of multiple EMT-TS coupling points. A testbed is built, and transient steps are carried to compare the proposed framework against a model fully developed in the EMT domain.

Finally, in Chapter 5, an optimal control of a hybrid PV plant for tracking power setpoints while maintaining robust power reserves for regulation and/or FFR services is proposed. Furthermore, the PV systems are built including the advanced power curtailment algorithm proposed in Chapter 3. The work demonstrates that by adding a high-power/low-storage battery-energy-storage system to a utility-scale PV system, the hybrid PV plant can properly provide fast regulation services even during days of high irradiance intermittency.

Real-Time Modeling and Control of DERs with Advanced Grid-Support Functionalities

by  
Victor Daldegan Paduani

A dissertation submitted to the Graduate Faculty of  
North Carolina State University  
in partial fulfillment of the  
requirements for the Degree of  
Doctor of Philosophy

Electrical Engineering

Raleigh, North Carolina  
2022

APPROVED BY:

---

Dr. Ning Lu

---

Dr. David Lubkeman

---

Dr. Mesut Baran

---

Dr. Anderson de Queiroz

---

Dr. Ning Lu  
Chair of Advisory Committee

## **DEDICATION**

To my family, Ana Maria Daldegan Paduani, Clederson Paduani, and Ana Laura  
Daldegan Paduani.

## BIOGRAPHY

Victor Daldegan Paduani received the B.S. degree in electrical engineering from the Federal University of Santa Catarina, Florianopolis, Brazil, and the M.S. degree in electrical engineering from Villanova University, Villanova, USA, in 2017 and 2019, respectively. He is currently working toward the Ph.D. degree in electrical engineering with the Future Renewable Electric Energy Delivery and Management (FREEDM) Systems Center, North Carolina State University, Raleigh, USA. His research interests include modeling distributed energy resources, microgrid controller design, and developing real-time, hardware-in-the-loop test systems that co-simulate power electronic systems, power system networks, and energy management systems.

## ACKNOWLEDGEMENTS

First, I would like to thank my Ph.D. advisor, Dr. Ning Lu. I can confidently say I have never met anyone as dedicated as she is to her work and her students in my entire life. I have learned so much from her, especially on the aspect of how to be a researcher and how to become a critical thinker. I feel very lucky to have chosen her as my advisor. I also would like to thank Dr. David Lubkeman, for sharing his expertise in the area of electromagnetic transients and for giving me valuable feedback every week in our meetings, and the committee members Dr. Mesut Baran and Dr. Anderson de Queiroz for reviewing my work and giving me constructive feedback to improve it.

I am also thankful for the labmates I have met during my time in the FREEDM center at NC State: Bei Xu, Lidong Song, Si Zhang, Rongxing Hu, Fuhong Xie, Hui Yu, Ashwin Shirsat, Qian Long, Mingzhi Zhang, Jiyu Wang, Ming Liang, Meng Yao, David Mulcahy, Asmaa Alrushoud, Catie McEntee, Ken Crawford, Qi Xiao, and Charles Kelly. I will never forget our long hours working together on our research projects. Our discussions and collaborations were key factors that allowed me to progress in my research.

I am also very thankful for some of the friends I have met during my time at NC State: Rafael Silva, Juliana Pin, Victor Duraes, Leonardo Cella, Dana Johnson, Oscar Montes, Michael Billups, Asya Atik, and Lars Sandvoll. You have helped me to maintain my mental health in place, and I will never forget the good times we have had.

Finally, I would like to thank my family, for their eternal love and support, and Meghan Cioci, for all her love and support since my first year in Graduate School. She was my rock when all else seemed to fail.

## TABLE OF CONTENTS

<b>List of Tables . . . . .</b>	<b>vii</b>
<b>List of Figures . . . . .</b>	<b>viii</b>
<b>Chapter 1 Introduction . . . . .</b>	<b>1</b>
1.1 Motivation and the Need for Renewables . . . . .	1
1.2 The Need for PV Power Curtailment . . . . .	5
1.3 The Need for Maximum Power Point Estimation . . . . .	8
<b>Chapter 2 Power Curtailment Functionality . . . . .</b>	<b>11</b>
2.1 State-of-the-art in Power Curtailment . . . . .	11
2.1.1 PV System Modeling . . . . .	13
2.2 Proposed Power Curtailment Algorithm . . . . .	15
2.2.1 Accumulator for Overshoot Suppression . . . . .	17
2.2.2 Adaptive Gain Adjustment . . . . .	19
2.3 Real-Time Simulation Results . . . . .	21
2.3.1 Overshoot Suppression . . . . .	22
2.3.2 Smoothing DC-link Voltage Oscillations . . . . .	24
2.3.3 Power Reference Tracking . . . . .	25
2.4 Conclusion . . . . .	27
<b>Chapter 3 Unified Power Curtailment Algorithm . . . . .</b>	<b>28</b>
3.1 PV Array Modeling . . . . .	29
3.2 Maximum Power Point Estimation . . . . .	32
3.3 Proposed Unified Algorithm . . . . .	35
3.3.1 Power Tracking at Steady-State . . . . .	37
3.3.2 Irradiance Decoupling Technique . . . . .	39
3.3.3 Rapid Setpoint Tracking . . . . .	42
3.4 Real-Time Simulation Results . . . . .	46
3.4.1 MPPE Performance . . . . .	46
3.4.2 Irradiance Decoupling Performance . . . . .	49
3.4.3 Rapid Setpoint Tracking Performance . . . . .	51
3.4.4 PV-Based Fast Frequency Response Service . . . . .	52
3.5 Conclusion . . . . .	57
<b>Chapter 4 Novel Real-Time EMT-TS Modeling Architecture . . . . .</b>	<b>58</b>
4.1 Proposed EMT-TS Testbed Framework . . . . .	60
4.2 EMT-TS Co-Simulation Coupling . . . . .	62
4.2.1 Time Interpolation Coupling . . . . .	62
4.2.2 Phasor Extraction . . . . .	64

4.3	EMT Domain Benchmark Model . . . . .	64
4.4	Simulation Results . . . . .	65
4.4.1	Transient Performance During Load Steps . . . . .	66
4.4.2	Influence of Coupling Delay and Time Interpolation . . . . .	69
4.4.3	Capacitor Switching Transients . . . . .	70
4.4.4	Computational Cost Analysis . . . . .	74
4.5	Conclusion . . . . .	74
<b>Chapter 5 Optimal Control of a Hybrid PV Plant</b>	. . . . .	<b>76</b>
5.1	Methodology . . . . .	79
5.1.1	PV Plant Model . . . . .	79
5.1.2	Grid-Following BESS Model . . . . .	80
5.1.3	Lithium-Ion Battery Model . . . . .	81
5.1.4	Hybrid PV Plant State-Space . . . . .	86
5.1.5	Model Predictive Control Design . . . . .	89
5.2	Real-Time Simulation Results . . . . .	103
5.2.1	Extended Kalman Filter Performance . . . . .	105
5.2.2	Power Regulation Performance . . . . .	109
5.2.3	Comparison Against a Thermal Unit . . . . .	119
5.3	Conclusion . . . . .	121
<b>Chapter 6 Summary and Future Work</b>	. . . . .	<b>123</b>
6.1	Future Work . . . . .	125
<b>References</b>	. . . . .	<b>126</b>

## LIST OF TABLES

Table 2.1	Testbed Simulation Parameters . . . . .	22
Table 2.2	DC-link Voltage Oscillations . . . . .	25
Table 4.1	Power Flow Error at Steady-state . . . . .	65
Table 4.2	Setup of Load Steps . . . . .	66
Table 6.1	Testbed Parameters from Chapter 3 . . . . .	135
Table 6.2	Required CPU cycles for one LM iteration. . . . .	136
Table 6.3	Testbed Parameters From Chapter 5 . . . . .	137

## LIST OF FIGURES

Figure 1.1	Full record of measurements from Mauna Loa. . . . .	2
Figure 1.2	Measurements from past 800,000 years (with ice-core data). . . . .	3
Figure 1.3	Examples of GSFs now required by grid standards. . . . .	5
Figure 1.4	PV power-voltage relation. . . . .	6
Figure 1.5	Example of inaccurate MPPE from PV plant. From [1]. . . . .	8
Figure 1.6	Rotating reference strategy from [1], in which N corresponds to the number of reference inverters. . . . .	9
Figure 2.1	Adaptive FPPT operation mode classification. From [2]. . . . .	12
Figure 2.2	Circuit and control system block diagrams of a grid-scale PV system.	14
Figure 2.3	Flowchart of a basic P&O power curtailment algorithm. . . . .	17
Figure 2.4	Example of the adaptive $K_{tr}$ adjustment. . . . .	20
Figure 2.5	Overshoot response comparison. . . . .	23
Figure 2.6	Comparison of DC-link voltage oscillations: (a) method 1, (b) method 2, (c) method 3. . . . .	24
Figure 2.7	$P_{ref}$ tracking comparison: (a) method 1, (b) method 2, (c) method 3. . . . .	26
Figure 2.8	Tracking error comparison. . . . .	26
Figure 3.1	Circuit and control system block diagrams of a utility-scale PV system equipped with the proposed unified power curtailment algorithm.	30
Figure 3.2	Single-diode PV model circuit. . . . .	30
Figure 3.3	Flowchart of the unified power curtailment algorithm proposed. . . . .	36
Figure 3.4	Illustration of the steady-state voltage step calculation strategy for a 612 kW PV system: (a) Power-voltage curve, (b) PV slope curve, (c) Steady-state voltage steps, (d) Expected output power ripples when using $V_{step-ss}$ with $\Delta P_{max} = 5$ kW. . . . .	38
Figure 3.5	(a) Relation between $K_{ph}$ and voltage for irradiance curves in steps of $40\text{ W/m}^2$ (0.04 p.u.). (b) Power-voltage curves of a 500 kVA PV system under different irradiance levels. . . . .	41
Figure 3.6	Sequence of steps of the RST algorithm. Note that slope at $V_\delta$ is used for calculating $V_{step,n+3}$ . The figure is not to scale. . . . .	44
Figure 3.7	Calculation of $V_{ref}$ in the first step of the RST algorithm. . . . .	44
Figure 3.8	Performance of the MPPE algorithm in a sunny day (Sampling rate: 10 Hz). . . . .	47
Figure 3.9	Performance of the MPPE algorithm in a cloudy day with estimated irradiance threshold set to $1100\text{ W/m}^2$ . . . . .	48
Figure 3.10	Comparison between the actual MPP and the estimated MPP for a cloudy day. (Sampling rate: 40 Hz) . . . . .	49
Figure 3.11	Performance of the MPPE algorithm in a cloudy day considering PV model parameter errors (Sampling rate: 10 Hz). . . . .	50

Figure 3.12	Irradiance estimation error with respect to: (a) temperature and irradiance, (b) irradiance changes ( $\Delta G$ ) and irradiance. . . . .	51
Figure 3.13	Performance of irradiance decouple method under 5% parameter error. (Sampling rate: 40 Hz) . . . . .	52
Figure 3.14	Comparison of the power setpoint tracking performance under irradiance intermittency between (a) the proposed RST method and (b) the adaptive FPPT (state-of-the-art). . . . .	53
Figure 3.15	Configuration of a feeder-level microgrid. . . . .	54
Figure 3.16	Frequency and voltage plots during microgrid cold-load pickup. . .	54
Figure 3.17	Short caption . . . . .	56
Figure 4.1	Proposed EMT-TS co-simulation testbed framework. . . . .	61
Figure 4.2	Time interpolation coupling technique from [3]. . . . .	63
Figure 4.3	A comparison of the nodal voltage magnitude between the full EMT and EMT-TS testbeds. . . . .	65
Figure 4.4	Short caption . . . . .	68
Figure 4.5	Voltage and frequency transient responses during Step III from Table 4.2 due to: (a) increasing the communication delay between EMT and phasor domains; (b) utilizing the time interpolation coupling technique . . . . .	70
Figure 4.6	Capacitor bank switching event: (a) peak-voltage energization (worst-case scenario); (b) Zero-voltage-crossing energization. . . . .	71
Figure 4.7	Proposed EMT-TS co-simulation testbed framework with capacitor bank moved to EMT domain. . . . .	72
Figure 4.8	Current injection of the capacitor bank: (a) EMT testbed; (b) EMT-TS testbed with the shunt capacitors modeled in EMT domain. .	73
Figure 4.9	Feeder bus voltages during capacitor bank switching: (a) EMT model; (b) EMT-TS model with shunt capacitors modeled in phasor domain; (c) EMT-TS model with shunt capacitors modeled in EMT domain. . . . .	73
Figure 5.1	BESS circuit and control system diagram. . . . .	80
Figure 5.2	Second-order equivalent lithium-ion battery model. . . . .	82
Figure 5.3	Modeling accuracy of the battery output voltage for linearizations at different equilibrium points. . . . .	85
Figure 5.4	Illustration of MPC prediction and control horizons. From [4]. . .	90
Figure 5.5	Proposed control strategy. . . . .	95
Figure 5.6	Basic steps in sky image processing: (a) raw masked image, (b) binary cloud detection, (c) cloud tracking with final cloud motion path, and (d) projected irradiance map. From [5]. . . . .	97
Figure 5.7	Google maps picture of the Sempra US Gas and Power CMS1 Solar Plant near Henderson, NV. From [6]. . . . .	98

Figure 5.8 Illustration of how the nowcasting performance is replicated in real-time. . . . .	99
Figure 5.9 Example of nowcasting simulated error estimating 60-seconds ahead for a 2 MW plant. . . . .	100
Figure 5.10 Extended Kalman Filter block diagram. . . . .	101
Figure 5.11 Configuration of a hybrid PV plant. . . . .	103
Figure 5.12 One-second resolution irradiance and temperature data utilized (day 1). . . . .	105
Figure 5.13 One-second resolution irradiance and temperature data utilized (day 2). . . . .	106
Figure 5.14 SOC estimation performance from a 9-hour long real-time simulation.	106
Figure 5.15 Modeling accuracy of the battery SOC estimation. . . . .	107
Figure 5.16 SOC estimation performance under parameter errors. . . . .	109
Figure 5.17 PV maximum available power for day 1. . . . .	110
Figure 5.18 PV maximum available power for day 2. . . . .	111
Figure 5.19 PJM regulation D signal: (a) day 1, (b) day 2. . . . .	111
Figure 5.20 Hybrid PV Plant performance in day 1: (a) power output, (b) battery SOC, (c) power output error. . . . .	113
Figure 5.21 Hybrid PV Plant performance in day 1: (a) PV output power, (b) BESS output power, (c) power reserves. . . . .	113
Figure 5.22 Hybrid PV Plant performance in day 1 with a lower power request: (a) power output, (b) battery SOC, (c) power output error. . . . .	115
Figure 5.23 Hybrid PV Plant performance in day 1 with a lower power request: (a) PV output power, (b) BESS output power, (c) power reserves. . . . .	115
Figure 5.24 Hybrid PV Plant performance in day 2: (a) power output, (b) battery SOC, (c) power output error. . . . .	117
Figure 5.25 Hybrid PV Plant performance in day 2: (a) PV output power, (b) BESS output power, (c) power reserves. . . . .	117
Figure 5.26 Moment of power reserves violations (a) PV and BESS output power, (b) power reserves and regulation D signal. . . . .	118
Figure 5.27 Battery measurements in day 2: (a) Voltage, (b) Current. . . . .	119
Figure 5.28 Hybrid PV Plant performance in day 2 with a regulation signal of 1.5 MW: (a) power output, (b) power output error. . . . .	120
Figure 5.29 Thermal generator performance following same power setpoint from day 2 with a regulation signal of 1.5 MW: (a) power output, (b) power output error. . . . .	121

# Chapter 1

## Introduction

### 1.1 Motivation and the Need for Renewables

Despite all the efforts currently being made to promote the adoption of renewable technologies to reduce carbon emissions, there is still a long and arduous road ahead of us. Figure 1.1 displays atmospheric measurements of carbon dioxide ( $\text{CO}_2$ ) concentration in parts per million collected daily from an observatory in Mauna Loa, Hawaii. The graph is known as ‘The Kneeling Curve,’ and it is updated daily by Scripps Institution of Oceanography at UC San Diego. Notice the last measurement corresponds to May 10th, 2022.

The measurements reveal a steady-state rise in the  $\text{CO}_2$  concentration in the last century. It is curious to observe that due to the enormous inertia of our planets’ environment, the effects of the ongoing pandemic goes imperceptible in the carbon concentration measurements. This yields the interpretation that even if the carbon emissions were instantly significantly reduced, it could take years for such event to start stabilizing the carbon build-up in the atmosphere. Figure 1.2 displays even more alarming results. Ice-core data measurements reveal the steady rise of  $\text{CO}_2$  concentrations observed in the last century

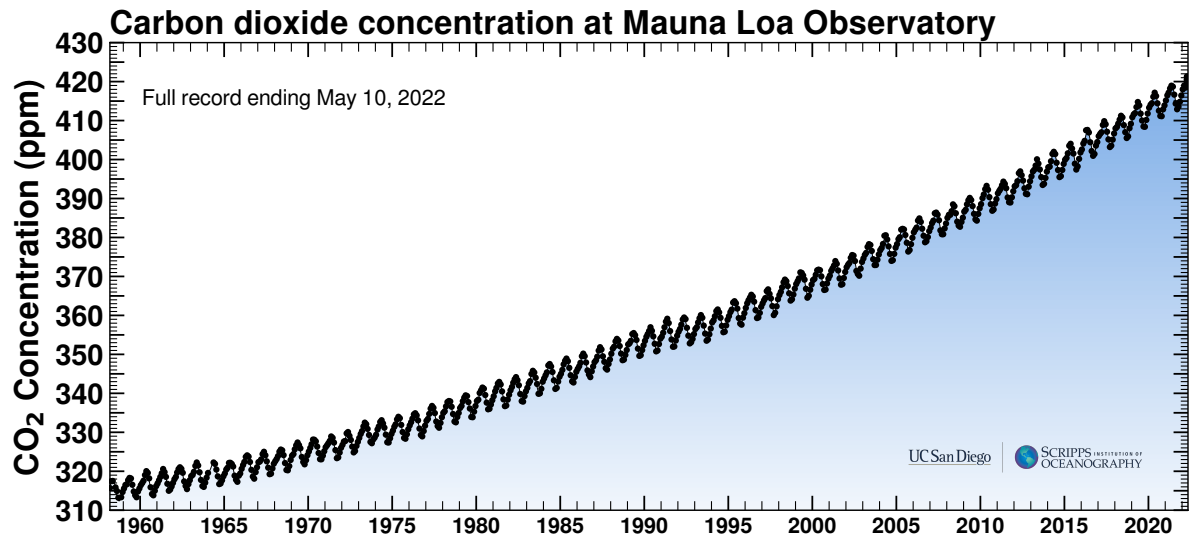


Figure 1.1: Full record of measurements from Mauna Loa.

have reached unprecedented peaks.

Unfortunately, no one knows how far this continuous increase of CO<sub>2</sub> can go before an irreversible condition is reached (considering there is still time). Nevertheless, under the right perspective, this bleak reality can also be interpreted as a source of motivation. It is up to us, scientists and engineers, to devise new technologies that can be leveraged to stop the climate change. With a future grid composed mainly by renewable energy sources (RES), and a transportation system transformed from combustion engines into electric drives, there is still hope that someday we may observe a decline in the Kneeling Curve.

Due to the greenhouse effect caused by excessive emissions of CO<sub>2</sub> into the atmosphere [7], it is imperative to eradicate (or significantly reduce) fossil-fuel based electric power generation. Consequently, in recent years, several projects envisioning the development and implementation of RES have been put into practice by governments worldwide. For instance, the SunShot Initiative [8] seeks to achieve a utility-scale solar energy at \$0.03 per kilowatt hour by 2030. Beyond the environmental concerns, another driving factor

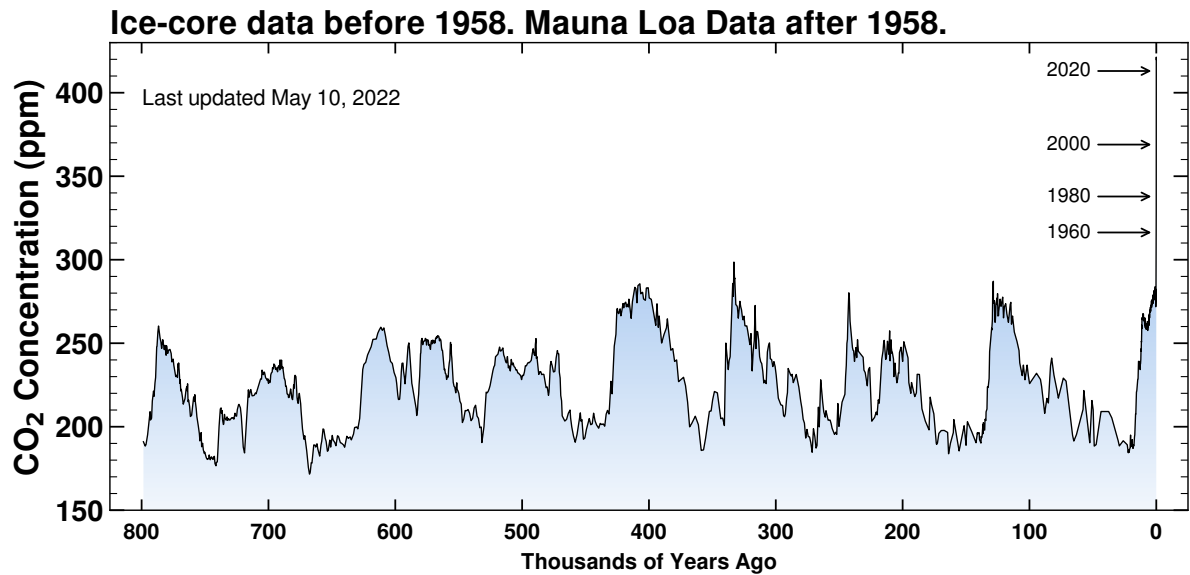


Figure 1.2: Measurements from past 800,000 years (with ice-core data).

for the increased integration of photovoltaic (PV) systems into the grid is their price reduction over the years [9].

Incentives in the form of tax credits provided by the U.S. government combined with a growing political awareness towards the future environmental challenges have greatly accelerated the integration of solar and wind energy into the grid. Nevertheless, due to the uncertain and unreliable power output from wind and solar, the electric grid as we once knew is experiencing a complete transformation, bringing many new challenges for electrical engineers to solve. Moreover, because PV systems can be installed at the customer side, another topic of great interest is the capability of operating the grid with a high participation of distributed energy resources (DERs). For instance, by adding PV generation at the customer level, zero-energy buildings can be achieved, selling energy back to support the grid when needed [10].

Even though operating a grid under high DER generation can be beneficial and more efficient, there are also major challenges associated with the volatility of PV systems. During moments of fast irradiance intermittency, the output from a PV array may reduce

from its rated value down to its minimum in a matter of seconds. In addition, if not properly accounted for, the reverse power flow caused by the excess of PV injection can threaten the system's volt-var control, potentially damaging electrical equipment due to overvoltage or unexpected operating modes.

Another important (arguably, the most critical!) challenge for increasing the PV penetration in our power grid is the need for grid-forming technology. For example, whenever a load step is applied to our grid, the synchronous machines distributed across the system are responsible for generating that energy. After the load step, the machines' governors are responsible for readjusting the injection of power into their rotating axes to re-stabilize the system's frequency back to its nominal value. However, governors have inherent time delays, and are unable to supply the instantaneous change in the load. Before the governor can respond, the machine's inertia is the source of energy during the load step transient (and obviously, that is why the frequency drops during the transient). As more synchronous machines are being retired and substituted by renewables, the overall system inertia is reducing, which makes the system more 'brittle', since disturbances (such as the loss of a generator) will cause higher frequency drops, possibly triggering under frequency load shedding (UFLS) conditions.

Therefore, there is a high interest both from power system utilities and research institutions to study the behavior of grids operating under high participation of inverter-based resources (IBRs). This work is focused on two main topics: (1) advanced control methods for IBRs to improve the capability of PV systems to assist the grid, and (2) the development of simulation tools that can be used to analyze power grid operating under a very high number of DERs.

## 1.2 The Need for PV Power Curtailment

In grids with high penetration of PV systems, there is an increasing need to employ inverters with superb controllability to provide grid-support functionalities (GSFs). Recent grid standards such as the IEEE Standard 1547-2018 [11] and the California Rule 21 [12] have raised the demands placed on PV inverters. Both standards now impose new operational requirements for enabling PV systems at all levels to provide high quality services. Among the main GSFs, can be mentioned the power curtailment, frequency-watt/volt-var droop, and disturbance ride-through capabilities. These functionalities are displayed in Fig. 1.3.

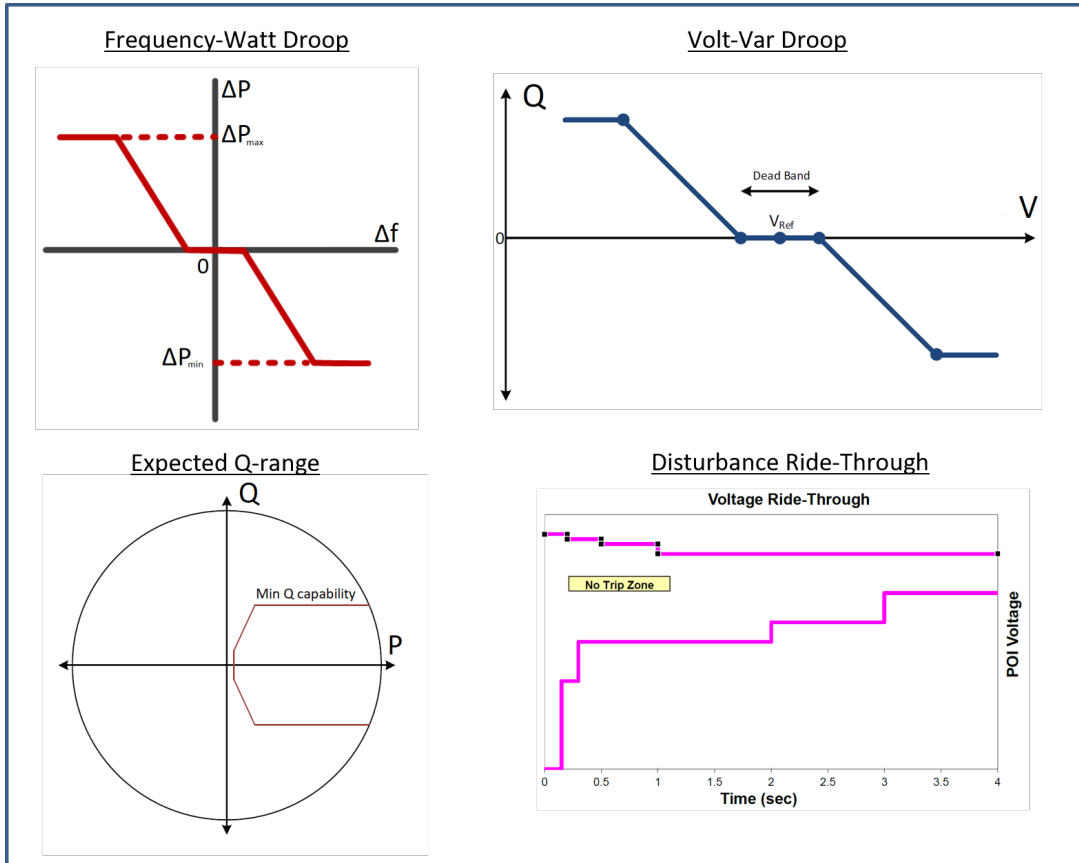


Figure 1.3: Examples of GSFs now required by grid standards.

As shown in Fig. 1.4, a PV system is able to curtail its output power to follow power

setpoints by regulating the voltage applied to its solar panels [13], [14]. The PV can be designed to operate either on the left or the right side of the maximum power point (MPP). By adjusting the voltage applied to the panels ( $V_n$ ), a controller can adjust the PV output power. Note that as the irradiance changes, the point corresponding to the desired power reference can present large deviations. Therefore, in order to track the setpoint accurately while the solar irradiance is constantly changing, two major functionalities are needed: the ability to predict accurately the voltage reference corresponding to the desired power setpoint, and to estimate the MPP available while operating in power curtailment mode. If both the aforementioned functionalities are achieved, then the PV system can be controlled similarly to a battery-energy-storage system (BESS).

By operating below its MPP, it can maintain headroom for providing power reserves.

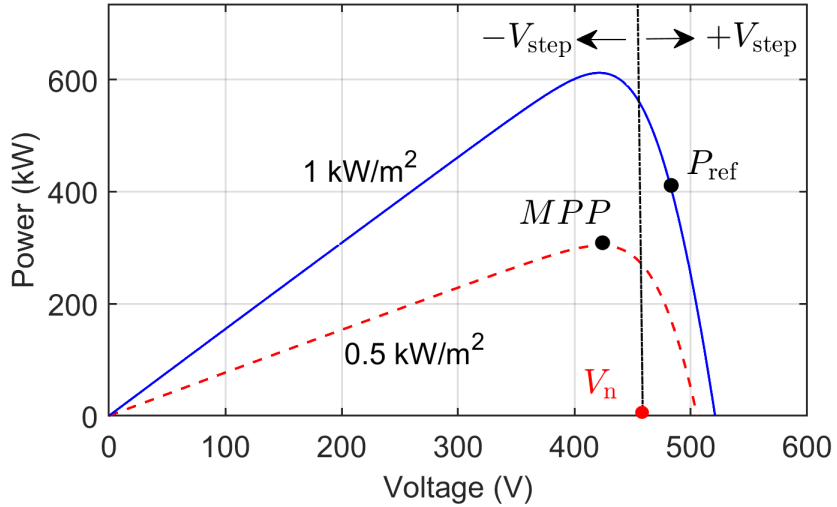


Figure 1.4: PV power-voltage relation.

Although maximum power point tracking (MPPT) algorithms for improving irradiance tracking are well researched in the literature, power curtailment algorithms remained under-examined until the last decade. In [15], Whandare and Agarwal introduced a power curtailment algorithm for single-staged PV systems, in which the dc-link voltage is con-

trolled by the inverter in fixed voltage steps based on the perturb and observe (P&O) algorithm. Meanwhile, other power limiting strategies based on proportional-integral controllers were introduced by Cao et al. in [16].

In [17], Sangwongwanich *et al.* compare P&O-based constant power generation (CPG) strategies with PI-based approaches. They show power and current controller PI-based CPGs can provide better tracking error, however, they can reach instability during moments of fast irradiance intermittency. On the other hand, P&O-based CPG achieved the highest robustness at the cost of worse dynamic response. In [2], Tafti *et al.* introduced an adaptive algorithm, in which the voltage step size during transients is proportional to the difference between the output power and the power reference. Their results confirmed less overshoot and faster convergence during irradiance changes. However, as the error increases drastically during sudden irradiance drops caused by passing clouds, the calculated variable voltage step size from the adaptive algorithm may become too big and cause large oscillations in the dc-link voltage, adding unwanted ripple to the output power and extra stress to circuit components.

Furthermore, despite the successful classification between transient and steady-state conditions, the issue of large power overshoots remains as noted in [18]. In normal operation, when solar irradiance increases, the PV output power also increases. Thus, as the system approaches its setpoint, the step size becomes smaller and smaller due to the diminishing power tracking error. This leads to a slower system response until the error becomes large again, eventually leading to overshoots. Consequently, there is a trade-off between the size of the adaptive gain and the power overshoot. To address those issues, two new functionalities to improve the adaptive FPPT are introduced in Chapter 2, focused on PV systems without maximum power point estimation (MPPE) or power reserves. The MPPE functionality is discussed next.

### 1.3 The Need for Maximum Power Point Estimation

The capability to accurately estimate what the MPP is while a PV system operates in power curtailment mode, denominated as MPPE in the literature, has drawn an increasing attention in recent years. In a study conducted by NREL [19], Gevorgian et al. demonstrated the capability of a large solar farm from Puerto Rico to provide GSF such as power curtailment, reactive power support, and participation in automatic generation control (AGC). However, as displayed in Fig. 1.5, the plant was incapable of properly following AGC commands due to errors in its MPPE. In that case, the approach for MPPE was based on irradiance sensors, which can lack in accuracy. One of the main conclusions of their work was that there is a need for more elaborate and accurate methods for estimating the available power of a PV plant while it operates in curtailment mode.

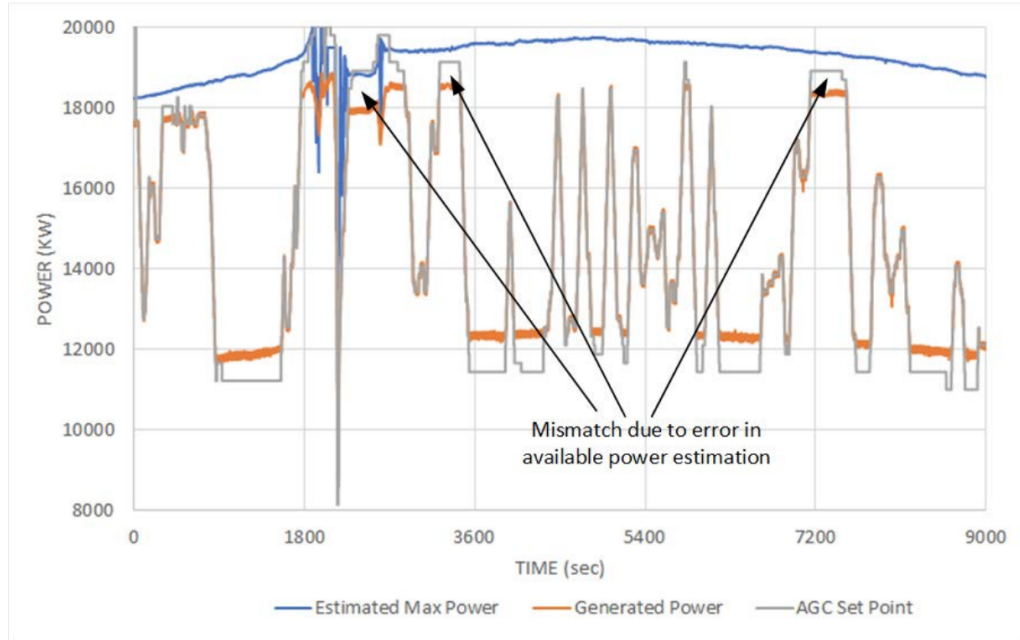


Figure 1.5: Example of inaccurate MPPE from PV plant. From [1].

In [20], it is proposed to monitor only some of the arrays of a PV farm, keeping them at their MPP to be used as an example for other arrays. However, that method

only works for large plants with many identical arrays. A similar approach is discussed in [1], but instead of utilizing the same reference inverter to find the MPP, the authors introduce a rotation strategy that continuously switches which inverter should operate in the MPP as a reference for the others. As shown in Fig. 1.6, the size of the plant will define how many inverters should be used as references at the same time.

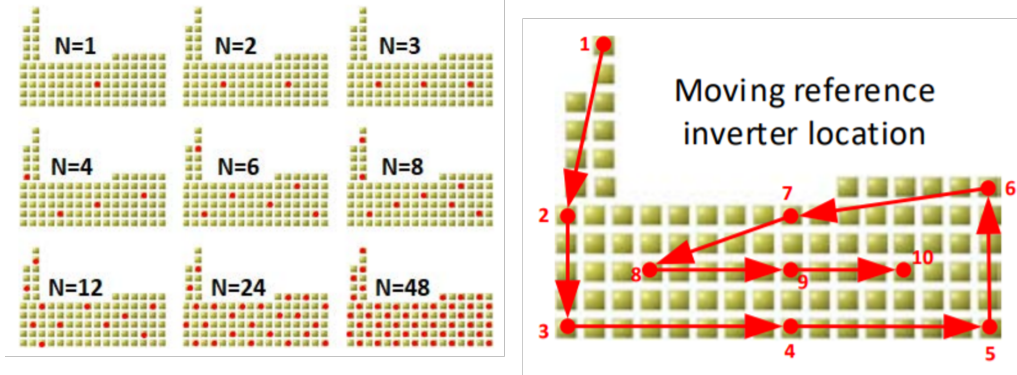


Figure 1.6: Rotating reference strategy from [1], in which  $N$  corresponds to the number of reference inverters.

In [21], the open-circuit voltage of the PV array is periodically measured by storing excess energy in the dc-link, which is then used to estimate the MPP voltage by assuming there is a constant relation between the open-circuit voltage and the voltage at MPP. However, this approximation can introduce significant errors, and the method requires both two-stage topologies and a design with an extra-large dc-link capacitance, making it unviable for large power applications. In [22], a curve-fitting technique via a non-linear least squares optimization is utilized to estimate the temperature and irradiance applied to a PV array based on voltage and current measurements. Yet, the method requires the introduction of an external ripple for proper convergence, and its setpoint tracking method is based on the PI power controller, which cannot provide fast and robust power-setpoint tracking.

Moreover, the integration of MPPE into power curtailment techniques for improving

the tracking capability is still an uncharted research area. As will be presented in Chapter 3, the information obtained from MPPE methods can be harvested not only to provide power reserves, but also to increase the power setpoint tracking speed, even enabling PV systems to provide fast frequency response (FFR). Zhu *et al.* in [23] and Li *et al.* in [24] developed power-setpoint tracking algorithms including MPPE, but the control scheme only functions in a two-stage PV system that operates on the left side of the MPP. This greatly limits the adoption of the algorithm in practice. An algorithm that utilizes MPPE to achieve FFR capabilities is presented in [25], but it relies on irradiance and temperature sensors, which are not accurate.

Within this dissertation, Chapter 2 will introduce two new functionalities to be added to the adaptive FPPT to address its weaknesses. Next, Chapter 3 will present an unified power curtailment algorithm for PV systems with FFR capabilities. Chapter 4 proposes a new architecture for simulating grids with high participation of DERs in real-time, via a EMT-TS Co-simulation testbed. Then, Chapter 5 will present an optimal control strategy for operating a hybrid PV plant that can maintain robust power reserves while being fully dispatchable. Lastly, Chapter 6 summarizes the work with final conclusions, and discusses directions for future research in this topic.

# Chapter 2

## Power Curtailment Functionality

As discussed in the previous chapter, the output power of a PV system can be regulated by controlling the DC voltage applied to its panels. In the past, MPPT algorithms were designed so that PV systems would always output the maximum available power, achieving excellent efficiency. However, with the reducing cost of PV, the need for power output dispatchability, and the challenges of reverse power flow, there has been a growing interest in the power curtailment functionality. In this chapter, a quick introduction to the state-of-the-art of PV power curtailment will be given, followed by an algorithm proposed to improve on the limitations of the state-of-the-art. Note that the algorithms from this chapter are focused on PVs without power reserves (or MPPE), which are more applicable to simpler systems due to a lower complexity both in computational cost and implementation.

### 2.1 State-of-the-art in Power Curtailment

One of the first evaluations of power curtailment methods, denominated constant power generation, or flexible power point tracking (FPPT) in the literature, was presented by

Sangwongwanich *et al.* in [17]. The authors demonstrated that the voltage tracking could be achieved either via current or power PI controllers, or based on the P&O technique. Moreover, an extensive comparison of eleven of the most prominent FPPT methods published in the literature was introduced in [26]. The analysis classified the FPPT algorithms into two main types: (i) type A, in which the control system of the converter is modified, while the irradiance tracking MPPT algorithm is maintained the same; and (ii) type B, in which the control system of the converter is maintained, but the irradiance tracking algorithm is modified. The study found that Type B methods present the best overall performance, and it concluded that one of the most prominent options is the adaptive FPPT due to its high robustness.

In the adaptive FPPT, a variable step size is used both for steady-state or transient operating conditions. The flowchart presented in Fig. 2.1 displays the logic utilized to classify the operation mode. It has been found that the operation mode classification proposed by the authors presents excellent performance. However, the adaptive FPPT still struggles with large power overshoots during irradiance swings, and too large steps during moments of lower irradiance conditions.

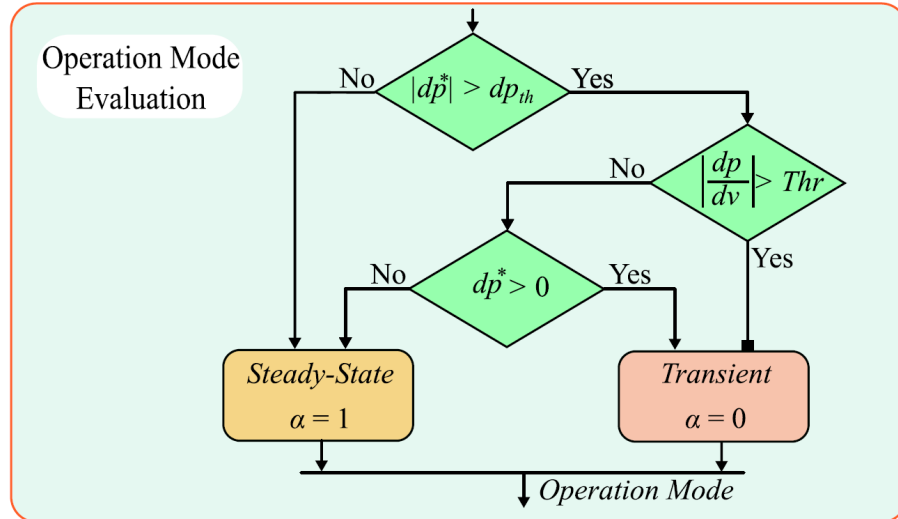


Figure 2.1: Adaptive FPPT operation mode classification. From [2].

Note that these weaknesses are directly related to the method how the adaptive FPPT updates the voltage step utilized to update the PV voltage reference. Because the step is proportional to the error between the output power and the power reference during transients, the step can become too small during moments when the irradiance is increasing back after a sudden drop. In addition, the step can also become too large when the irradiance reduces too much, during which the power reference (sometimes a fixed value) will present a large error from the actual available output power, causing unwanted oscillations. These problems and the proposed solutions to solve them will be discussed in detail in this Chapter. In the following sections, we will present the modeling of a PV system with power curtailment including two new functionalities to improve on the weaknesses of the adaptive FPPT.

### 2.1.1 PV System Modeling

Figure 2.2 shows the circuit diagram of a single-stage, centralized inverter found in a grid-scale PV farm. The circuit is composed by a PV array connected via a dc-link to a three-phase inverter, which is connected to the grid via a step-up Y/Yg transformer. The PV array is modeled with a 5-parameter model from [27]. To reduce the computational burden for real-time or faster-than-real-time applications, the inverter is modeled with an averaged model of a two-level voltage source converter (VSC) developed in [28]. The inverter is controlled by a three-phase modulation signal,  $\vec{m}$ . A saturation block is added to the modulation signal to ensure that the limitations imposed by the instantaneous dc-link voltage are considered for the generation of the three-phase output voltage.

The voltage of the two-level VSC before its output filter,  $\vec{v}_t$ , is given by

$$\vec{v}_t = \frac{v_{dc}}{2} \vec{m} \quad (2.1)$$

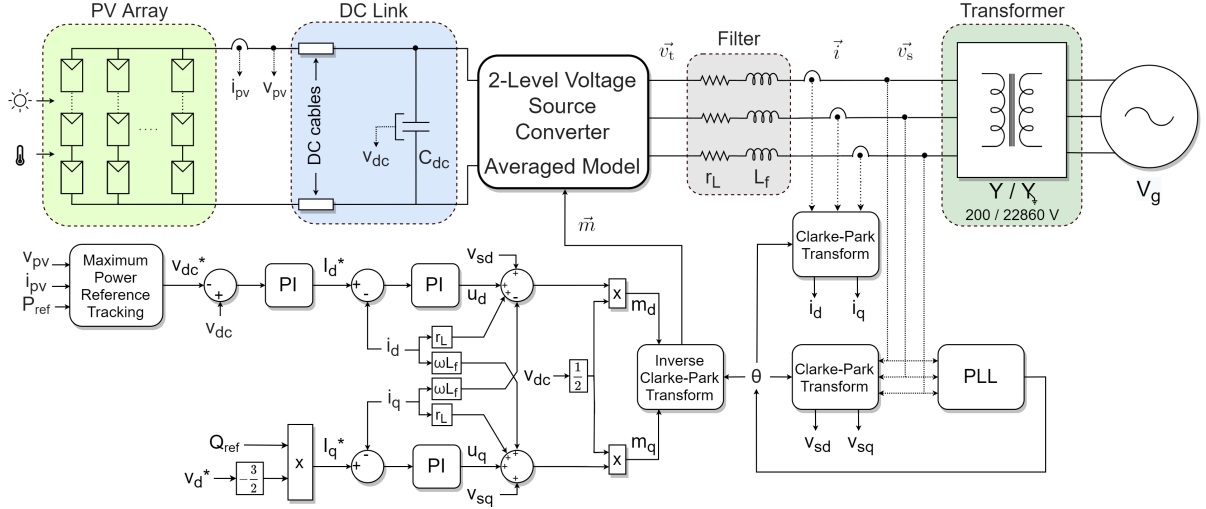


Figure 2.2: Circuit and control system block diagrams of a grid-scale PV system.

where  $\vec{m}$  is the modulation signal and  $v_{dc}$  is the dc bus voltage.

Then, using KCL, the secondary voltage of the transformer, ( $\vec{v}_s$ ), is expressed as

$$\vec{v}_s = \vec{v}_t - r_L \vec{i} - L_f \frac{d\vec{i}}{dt} \quad (2.2)$$

where  $i$  is the output current of the converter;  $r_L$  and  $L_f$  are the filter resistance and inductance, respectively.

As shown in the control system block diagram in Fig. 2.2, the PV farm is operated in the grid-following mode, and the PV inverter controller will regulate the output current so that the power supplied from the dc-link to the grid follows the real and reactive power reference signals,  $P_{ref}$  and  $Q_{ref}$ . The Clarke-Park transformation is used to convert the 3-phase voltage measurements to dq0 coordinates whereas a phase-locked loop (PLL) is used to extract the phase of the grid.

In dq0 coordinates, a phasor  $\vec{x}$  can be defined as  $x_d + jx_q$ , and its derivative can be represented as

$$\frac{d\vec{x}}{dt} = \frac{dx_d}{dt} + j \frac{dx_q}{dt} + j\omega(x_d + jx_q) \quad (2.3)$$

where  $\omega$  is the nominal angular frequency of the system.

By separating the real and imaginary parts, Eq. (2.3) can be rewritten as

$$L \frac{di_d}{dt} = m_d \frac{v_{dc}}{2} + \omega L_f i_q - r_L i_d - v_{sd} \quad (2.4)$$

$$L \frac{di_q}{dt} = m_q \frac{v_{dc}}{2} - \omega L_f i_d - r_L i_q - v_{sq} \quad (2.5)$$

where  $i_d$  and  $i_q$ ,  $v_{sd}$  and  $v_{sq}$ ,  $m_d$  and  $m_q$ , are the direct and quadrature components of  $i$ ,  $v_s$ , and  $m$ , respectively. To decouple the currents and remove  $v_{sd}$  and  $v_{sq}$  from the control system,  $m_d$  and  $m_q$ , are calculated as

$$m_d = \frac{2}{v_{dc}} \left( v_{sd} - \omega L_f i_q + r_L i_d + u_d \right) \quad (2.6)$$

$$m_q = \frac{2}{v_{dc}} \left( v_{sq} + \omega L_f i_d + r_L i_q + u_q \right) \quad (2.7)$$

where  $u_d$  and  $u_q$  are the outputs of the current controllers. Notice that the filter resistance is also included as a feed-forward term to improve the control performance. The three-phase modulation signal,  $\vec{m}$ , is then generated by  $m_d$  and  $m_q$  using the inverse Clarke-Park transformation. The control parameter design is not the focus of this work, but further detail regarding the cascaded voltage and current controllers design can be found in [15].

## 2.2 Proposed Power Curtailment Algorithm

As seen in the P-V characteristic curve of a solar panel displayed in the previous chapter, the power delivered by the panels at a given irradiance can be controlled via the dc-link voltage. Therefore, the objective of the power curtailment algorithm is to find the voltage

reference that will extract the desired power from the panels based on the ongoing irradiance and temperature conditions. In a P&O-based strategy, the algorithm constantly updates its output reference in positive or negative steps depending on the effect of the previous step on the output power of the system. Whenever a step reduces the output power when it was actually desired to increase the output power, for example, the sign of the next step added to the reference will be opposite, and thus the model is able to eventually converge to the MPP.

According to the flowchart in Fig. 2.3, when the output power of the panels,  $P_{\text{pv}}$ , is below a given reference,  $P_{\text{ref}}$ , the system operates as the P&O method; when  $P_{\text{pv}}$  is above  $P_{\text{ref}}$ , the voltage reference,  $v_{\text{dc}}^*$ , is adjusted to curtail  $P_{\text{pv}}$ . Whether the current operation point is on the right side or the left side of the MPP can be determined by increasing or decreasing  $v_{\text{dc}}^*$ , respectively, with a step size of  $V_{\text{step}}$ , whenever  $P_{\text{pv}}$  is above  $P_{\text{ref}}$ . In a single-stage PV system, because of inherent limitations of inverters [29], the dc-link voltage,  $V_{\text{dc}}$ , should always be kept above a minimum voltage threshold, so operation on the right side of the MPP is necessary.

The algorithm's convergence speed is primarily determined by  $V_{\text{step}}$  at each iteration. Ideally,  $V_{\text{step}}$  should be small in steady-state operation to reduce power oscillations around  $P_{\text{ref}}$ , and large during transients for a rapid response to changes in  $P_{\text{ref}}$  or irradiance. As introduced in [2], a fast convergence during transient operation can be achieved by making  $V_{\text{step}}$  a function of the error from the power reference  $P_{\text{err}}$ , so we have

$$\begin{aligned} V_{\text{step},n} &= \alpha \times V_{\text{step}}^{\min} + (1 - \alpha) \times K_{\text{tr}} |P_{\text{err},n}| \\ P_{\text{err},n} &= P_n - P_{\text{ref},n} \end{aligned} \tag{2.8}$$

where  $\alpha$  is used to switch between the power error consideration in the transient operation and the fixed minimum step change in the steady-state operation, and  $K_{\text{tr}}$  is a constant

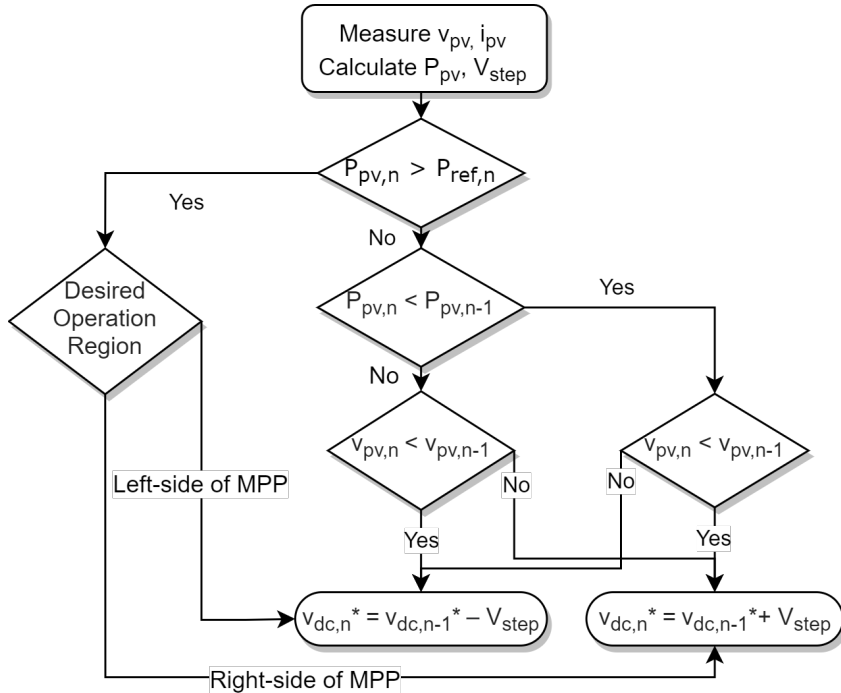


Figure 2.3: Flowchart of a basic P&O power curtailment algorithm.

gain for considering  $P_{\text{err}}$ .

It is important to highlight here that in the adaptive FPPT, the step at steady-state is not fixed, as it will vary based on the measured output PV slope. However, here the step at steady-state is maintained the same since this algorithm is analyzing the improvements made during the transient operating condition. For details on how to design the FPPT step at steady-state, please refer to [2]. Furthermore, in Chapter 3, a new straightforward method will be proposed for the steady-state step of the adaptive FPPT, which can be used to maintain the output power ripple within specified boundaries.

### 2.2.1 Accumulator for Overshoot Suppression

Overshoot is still a critical issue found in P&O-based power curtailment algorithms (see Fig. 16c in [17]). The common cause of an overshoot is the rapid increase of solar irradiance after a passing cloud. If a controller cannot curtail  $P_{\text{pv}}$  fast enough, an overshoot

over  $P_{\text{ref}}$  will occur. Recall that when we adjust  $V_{\text{step}}$  based on  $P_{\text{err}}$  in (8),  $V_{\text{step}}$  becomes smaller as  $P_{\text{pv},n}$  moves closer to  $P_{\text{ref}}$ . Thus, with a reducing  $V_{\text{step}}$  and an increasing solar irradiance,  $P_{\text{pv}}$  will overshoot  $P_{\text{ref}}$  and the overshoot can be long-lasting unless  $V_{\text{step}}$  can be increased accordingly. To suppress the overshoots, we introduce an accumulator,  $\gamma$ , into the  $V_{\text{step}}$  calculation.

At the beginning of each iteration, the moving average of the absolute error variation,  $\overline{\Delta P_{\text{err},n}}$ , is calculated by

$$\begin{aligned}\Delta P_{\text{err},n} &= |P_{\text{err},n}| - |P_{\text{err},n-1}| \\ \overline{\Delta P_{\text{err},n}} &= \frac{1}{M} \sum_{i=0}^{M-1} \Delta P_{\text{err},n-i}\end{aligned}\tag{2.9}$$

Then, if  $\overline{\Delta P_{\text{err},n}} > 0$  and  $P_{\text{pv},n} > P_{\text{ref}}$ , marking the detection of an overshoot, we will add  $\gamma_n$  to the  $V_{\text{step},n}$  calculated from (8). If there is no overshoot detected, but variations in  $P_{\text{pv},n}$  have been positive in the previous two iterations, then  $\gamma_n$  is increased by (2.10). Otherwise,  $\gamma_n$  is multiplied by a resetting rate,  $\lambda_r$ .

$$\gamma_n = \gamma_{n-1} + K_{\text{acc}} \times K_{\text{base}} \times |P_{\text{err},n}| \tag{2.10}$$

The overshoot suppression is presented in Algorithm 1. The accumulator's behavior can

---

**Algorithm 1** Accumulator  $\gamma_n$ 


---

```

Calculate  $\overline{\Delta P_{\text{err},n}}$  ▷ (2.9)
2: if  $\overline{\Delta P_{\text{err},n}} > 0$  and  $P_{\text{pv},n} > P_{\text{ref}}$  then
    $V_{\text{step}} = V_{\text{step}} + \gamma_n$ 
4: else if  $P_{\text{pv},n} > P_{\text{pv},n-1} > P_{\text{pv},n-2}$  then
   Increase  $\gamma_n$  ▷ (2.10)
6: else
    $\gamma_n = \lambda_r \gamma_n$ 

```

---

be summarized as follows: while it is being added to  $V_{\text{step}}$ , its inner value is frozen, whereas

at every iteration in which it is not added to  $V_{\text{step}}$ , its value is either increased by (12) (if  $P_{\text{pv}}$  is increasing) or it is reduced by  $\lambda_r$ . It is important to notice that a saturation should be applied to the accumulator so that its maximum value stays within acceptable ranges of voltage step sizes at all times.

### 2.2.2 Adaptive Gain Adjustment

There is a major limitation when using Eq. (2.8) to calculate  $V_{\text{step}}$ . When the irradiance suddenly drops to a level where it is impossible for the PV system to converge to  $P_{\text{ref}}$ ,  $V_{\text{step}}$  will be too large, causing the DC link voltage to oscillate rapidly, adding unnecessary stress to the electrical components. To attenuate this issue, in [2], a mode classification method for separating steady-state and transient modes is used to switch  $V_{\text{step}}$  to a smaller value when the irradiance is low. However, the tuning method for the operation mode classification is not clearly defined, and if it is not well designed, the issue can be further aggravated. Besides, irradiance variations happen very often amid the region of lower irradiance, which causes the system to switch to transient mode frequently.

Therefore, in this paper, we introduce a compensation factor for adjusting  $K_{\text{tr}}$  in real-time to provide a robust solution to this issue. First, we calculate the moving average of the power output of the system at time interval  $n$  over a window of length  $N$ , by (2.11). Note that after each iteration, the oldest output power value is substituted by a new one.

$$\overline{P_{\text{pv},n}} = \frac{1}{N} \sum_{i=0}^{N-1} P_{\text{pv},n-i} \quad (2.11)$$

Then, by comparing  $\overline{P_{\text{pv},n}}$  with  $P_{\text{ref}}$ ,  $K_{\text{tr}}$  is calculated as

$$K_{\text{tr}} = \text{Max} \left[ C_{\min} K_{\text{base}}, K_{\text{base}} \left( \frac{\overline{P_{\text{pv},n}}}{P_{\text{ref}}} \right)^2 \right] \quad (2.12)$$

where  $C_{\min}$  defines the lower boundary related to the minimum  $K_{\text{tr}}$  acceptable, and  $K_{\text{base}}$  is the original gain. Note that from (2.12), the adaptive gain  $K_{\text{tr}}$  will never be above its base value  $K_{\text{base}}$ , since the update is only taken place during regions of lower irradiance conditions, when the output power  $P_{\text{pv}}$  will be smaller than the power reference  $P_{\text{ref}}$ . The pseudo code for adaptively adjusting  $K_{\text{tr}}$  is shown in Algorithm 2.

---

**Algorithm 2** Adaptive  $K_{\text{tr}}$  adjustment

---

```

1: Calculate  $\overline{P}_{\text{pv},n}$  ▷ (9)
2: if  $(P_{\text{pv},n} - \overline{P}_{\text{pv},n})(P_{\text{pv},n-1} - \overline{P}_{\text{pv},n}) > 0$  then
3:    $C_t = 0$ 
4: else
5:    $C_t += 1$ 
6: if  $P_{\text{pv},n} > P_{\text{ref}} - \tau_1$  or  $|P_{\text{pv},n} - \overline{P}_{\text{pv},n}| > \tau_2$  then
7:    $K_{\text{tr},n} = K_{\text{base}}$ 
8: else if  $C_t \geq C_{t,\max}$  then
9:   Update  $K_{\text{tr}}$  ▷ (10)
10: else
11:    $K_{\text{tr},n} = K_{\text{tr},n-1}$ 

```

---

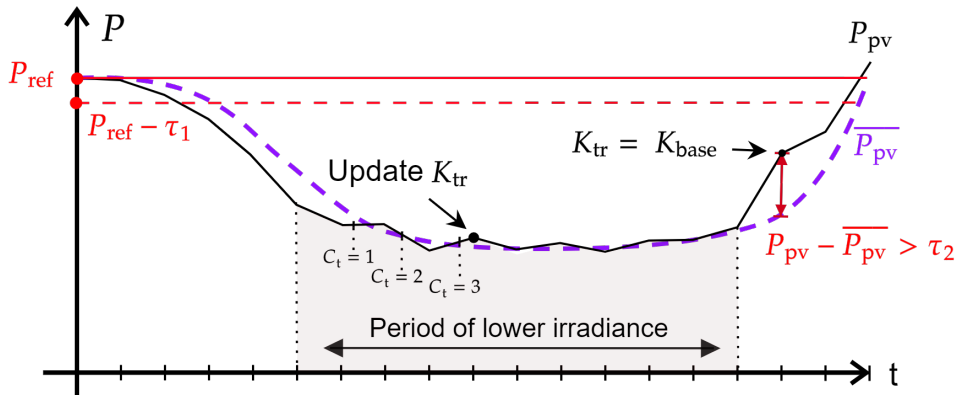


Figure 2.4: Example of the adaptive  $K_{\text{tr}}$  adjustment.

When  $P_{\text{pv}} < P_{\text{ref}}$ , the steady-state operation point is the MPP corresponding to the solar irradiance, which can vary constantly, causing the system to switch to the transient operating mode. As illustrated in Fig. 2.4, to determine whether or not an MPP is reached, a counter,  $C_t$ , is used to count the number of continuous crossings between  $P_{\text{pv}}$

and  $\overline{P_{\text{pv},n}}$ . If  $P_{\text{pv},n}$  crosses  $\overline{P_{\text{pv},n}}$ ,  $C_t$  is incremented; otherwise  $C_t$  is reset to zero. Once the counter threshold,  $C_{t,\max}$ , is reached,  $K_{\text{tr}}$  will be adjusted. In this paper, we set  $C_{t,\max} = 3$  to balance the adjustment speed of  $K_{\text{tr}}$  and the MPP detection accuracy. Once adjusted,  $K_{\text{tr}}$  will maintain its new value. If  $C_t = C_{t,\max}$  again, another adjustment will be made. If irradiance increases quickly either (i) causing a large increase in  $P_{\text{pv},n}$  when compared to  $P_{\text{ref}} - \tau_1$  or (ii) entering the control deadband so that  $|P_{\text{pv},n} - \overline{P_{\text{pv},n}}| > \tau_2$ ,  $K_{\text{tr}}$  will be reset to  $K_{\text{base}}$ , as shown in operation 6 of Algorithm 2 and Fig. 2.4.

## 2.3 Real-Time Simulation Results

To test the proposed adaptive gain adjustment and accumulator algorithms, we set up a testbed of a 500 kVA PV system on an OPAL-RT real-time simulation platform. One-second irradiance data collected from a 1.04 MW solar farm by EPRI [30] is used. To demonstrate the power following capability in a realistic application, we apply a unidirectional 200 kW PJM regulation signal to the estimated available power of the system to generate the power reference command. In this case, the estimated power is obtained by applying a low-pass filter to the irradiance. The simulation timestep is 100  $\mu\text{s}$ . To account for measurement noise due to sensor imperfections, a Gaussian noise was added to  $v_{\text{pv}}$ ,  $i_{\text{pv}}$ , and  $v_{\text{dc}}$ , creating a signal-to-noise-ratio of 71 dB. The list of simulation parameters for the testbed implementation are listed in Table 2.1.

The performance of three control methods are compared. In method 1,  $V_{\text{step}} = 0.3 \text{ V}$  in steady-state and  $V_{\text{step}} = 4 \text{ V}$  in transient operation. In method 2,  $V_{\text{step}} = 0.3 \text{ V}$  in steady-state, and (8) proposed by [2] is used to compute  $V_{\text{step}}$  during transients. Method 3 is the proposed algorithm. Since the focus of the functionalities proposed in this work resides on the transient operating mode, the step at steady-state is fixed at a constant value for all three methods for a fair comparison, even though the adaptive FPPT design

Table 2.1: Testbed Simulation Parameters

PV Array	Power	612 kW
	Module	CS6P-250P
	Size (parallel $\times$ series)	153 $\times$ 16
	$V_{mpp}$ , $I_{mpp}$	481.6 V, 1270 A
Inverter	Power, Frequency	500 kVA, 60 Hz
	$L_f$ , $r_L$	100 $\mu$ H, 3 m $\Omega$
	$C_{dc}$	5000 $\mu$ F
	PI ( $v_{dc}$ )	$K_p = 1$ , $K_i = 250$
	PI ( $i_d$ , $i_q$ )	$K_p = 0.7$ , $K_i = 50$
Transformer	Power, Frequency	500 kVA, 60 Hz
	$V_{LL}$ (rms)	200 V / 22.86 kV
	$X_{leak}$ , $r_{loss}$ (pu)	0.06, 0.0024
	$L_m$ , $r_m$ (pu)	200, 200
	Core type	Three-limb
MPRT	Sampling frequency	5 Hz
	$K_{base}$ , $K_{acc}$ , $C_{min}$	0.00006, 0.3, 0.2
	$V_{step}^{\min}$ / $V_{step}^{\max}$	0.3 / 12 V
	$\tau_2, \tau_1$	7.5 / 10 kW
	$N, M, C_{t,max}, \lambda_r$	4, 3, 3, 0.5

includes a variable step at steady-state.

### 2.3.1 Overshoot Suppression

In this section, we demonstrate the advantage of utilizing the overshoot suppression functionality from the proposed power curtailment algorithm. Figure 2.5 demonstrates the efficacy of employing an accumulator mechanism for calculating  $V_{step}$  during large irradiance variations. Because the initial irradiance increase makes  $P_{pv}$  approach  $P_{ref}$ ,

$V_{\text{step}}$  calculated by Eq. (2.8) (method 2) will continuously decrease even though the irradiance may still be rapidly increasing. Since the step will remain small until a large output power error is achieved, this can cause a large output power overshoot. In method 3, the accumulator internal value,  $\gamma$ , accumulates while the irradiance increases. Once an overshoot is detected (based on the moving average of the derivative of the output power error), the accumulator is activated and its value is added to  $V_{\text{step}}$ , providing a faster response to suppress the overshoot, as shown in the first plot in Fig. 2.5. Because the resetting rate of the accumulator is greater than zero, it can be activated multiple times throughout one overshoot event, as shown in the second plot of Fig. 2.5.

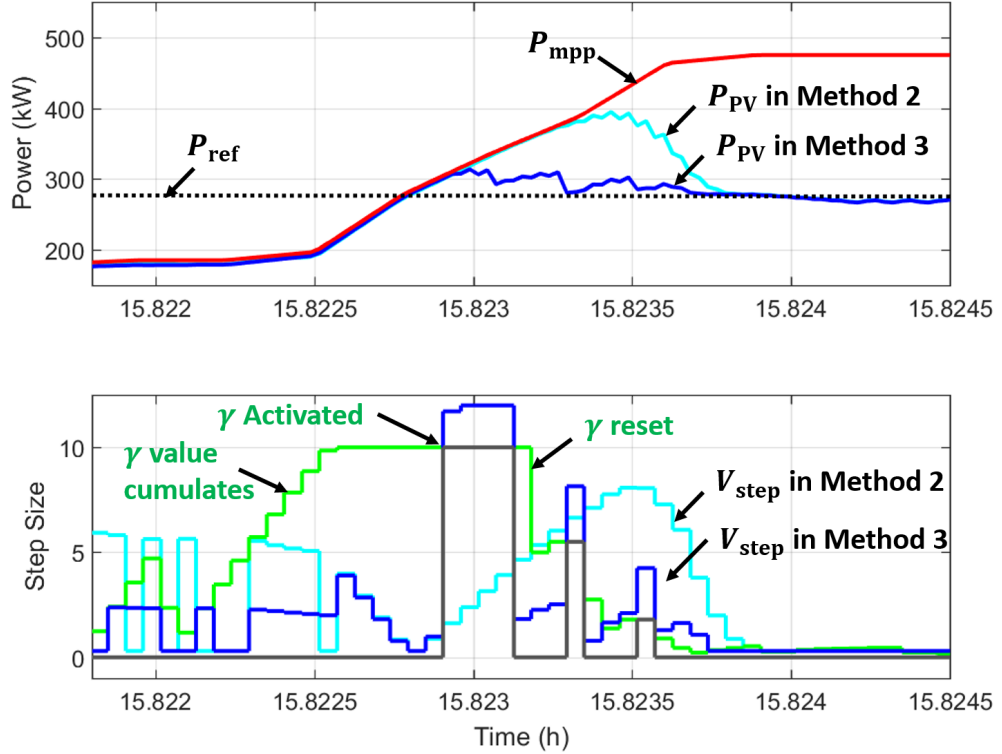


Figure 2.5: Overshoot response comparison.

### 2.3.2 Smoothing DC-link Voltage Oscillations

Figure 2.6 displays the operation of each method during periods of low irradiance conditions. By adjusting  $K_{tr}$  in real-time, method 3 can reduce the oscillations in  $v_{dc}$  during low-irradiance conditions when  $P_{ref} > P_{mpp}$ , making the system more stable and applying less unnecessary stress on the electrical components. In Table 2.2, we use the cumulative voltage oscillations ( $\sum |V_{dc(t)} - V_{dc(t)}|$ ) for three consecutive days to compare the performance of each method at different irradiance levels. Note that lower  $V_{dc}$  values ( $V_{dc} < 450$  V) corresponds to lower irradiance periods, since the P-V curve that correlates the output power with the operating PV panel voltage ‘shrinks’ as the irradiance decreases (observe Fig. 1.4). It can be clearly seen that method 3 outperforms methods 1 and 2 in low irradiance cases.

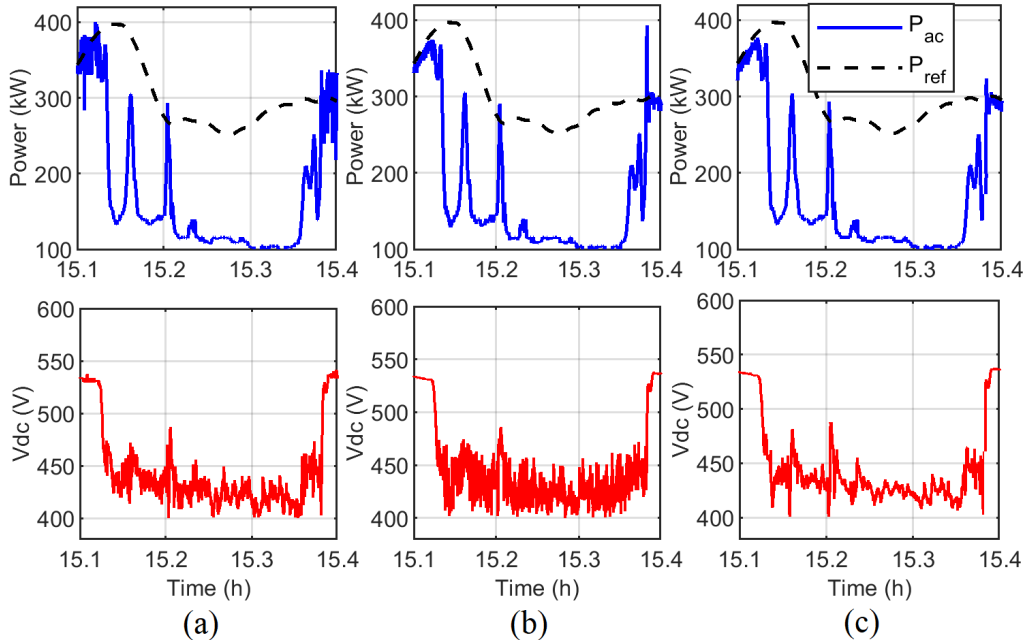


Figure 2.6: Comparison of DC-link voltage oscillations: (a) method 1, (b) method 2, (c) method 3.

The effects of the overshoot suppression algorithm can also be noticed in Fig. 2.6. While the irradiance swing caused a large output power spike when utilizing method 2,

Table 2.2: DC-link Voltage Oscillations

Method	$V_{dc} < 450 \text{ V}$	$450 \leq V_{dc} < 500 \text{ V}$	$V_{dc} \geq 500 \text{ V}$
1	121k	69k	417k
2	149k	63k	171k
3	77k	50k	171k

the overshoot was significantly suppressed in method 3. Furthermore, due to the fixed large voltage step in method 1, the overshoot was avoided, but large output power ripples are observed due to an excessively large transient step.

### 2.3.3 Power Reference Tracking

The performance of the three methods when tracking  $P_{\text{ref}}$  for providing regulation signals is shown in Fig. 2.7. Method 1 presents large oscillations during transients because of its large fixed transient  $V_{\text{step}}$ . Method 2 can mitigate the oscillations, but it is susceptible to overshoots caused by large irradiance changes. On the other hand, method 3, equipped with adaptive  $K_{\text{tr}}$  adjusted by the accumulator value  $\gamma$ , can suppress overshoots during the irradiance recovery process.

Tracking errors with a 0.1s resolution are calculated for three days of operation. When  $P_{\text{ref}} \leq P_{\text{mpp}}$ , the error is calculated as  $P_{\text{err}} = |P_{\text{pv}} - P_{\text{ref}}|$ ; when  $P_{\text{ref}} > P_{\text{mpp}}$ , the error is calculated as  $P_{\text{err}} = |P_{\text{pv}} - P_{\text{mpp}}|$ . The cumulative percentage of tracking error,  $E_{\text{sum}}$  is calculated by

$$E_{\text{sum}} = \frac{\int |P_{\text{err}}|}{\int |P_{\text{pv}}|} \quad (2.13)$$

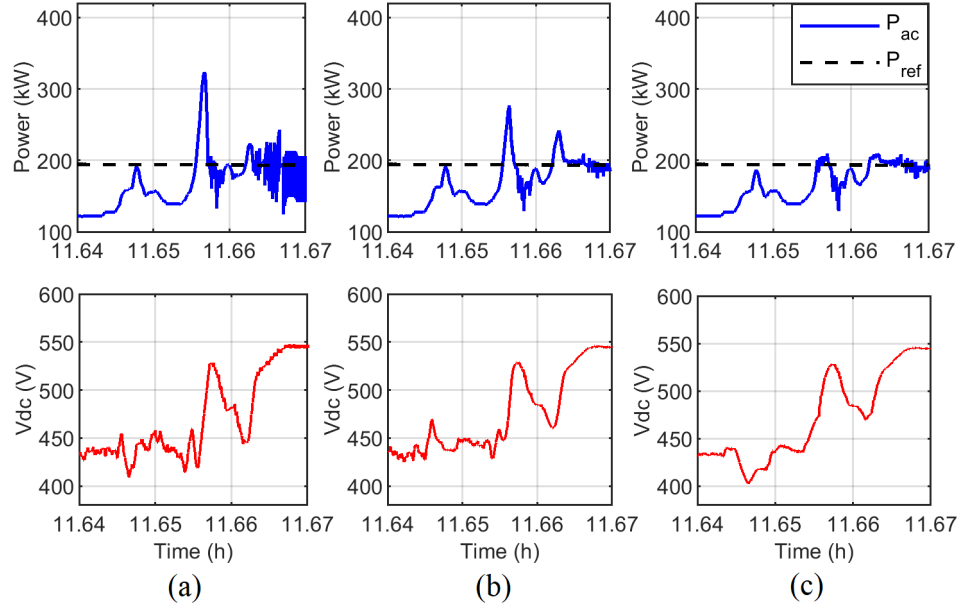


Figure 2.7:  $P_{\text{ref}}$  tracking comparison: (a) method 1, (b) method 2, (c) method 3.

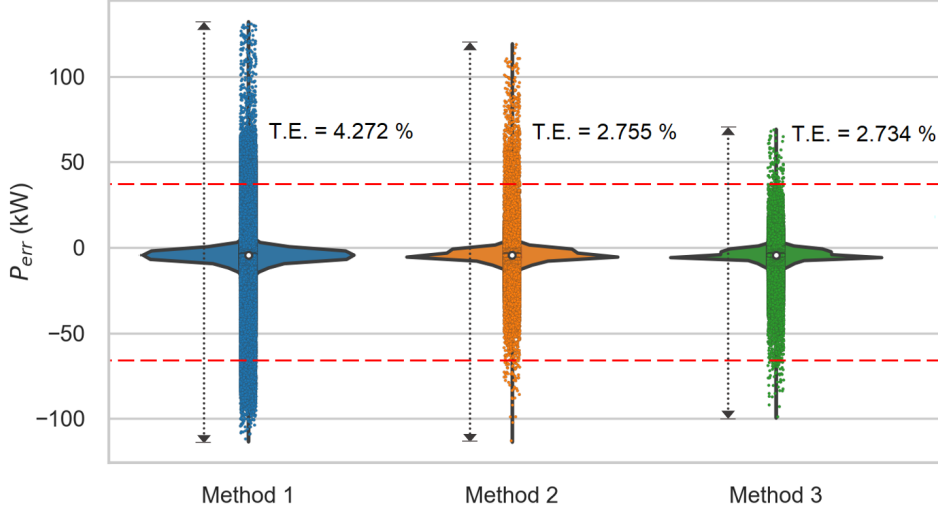


Figure 2.8: Tracking error comparison.

Figure 2.8 displays violin plots overlaid by scatter plots of  $P_{\text{err}}$  for the three methods. The scatter plot is used to highlight how the operating data is concentrated. The dashed red lines indicate the region of concentrated data points from scatter plot of method 3. Furthermore, it is important to note that in this analysis, the adaptive gains in methods

2 and 3 are kept the same for a fair comparison. Yet, the real-time adjustment of the adaptive gain introduced in method 3 permits its system to be designed with an even higher adaptive gain base value, which can be leveraged to reduce the tracking error even further.

## 2.4 Conclusion

In this chapter, a new method to control the dc-link voltage of a PV system to achieve a better power reference tracking capability is presented. The proposed algorithm adds two new mechanisms for controlling the PV panels voltage. First, by comparing the PV power output with its average output power, the controller can identify the operating conditions when the MPP is below the power reference. Then, the gain to adjust the voltage step size can be reduced in real-time so that it is only large when needed. Second, an overshoot detection mechanism is used to trigger an accumulator for suppressing overshoots. Simulation results demonstrate a dc-link with reduced oscillations in lower irradiance conditions, and an improved overshoot response when compared to existing P&O-based methods in the literature.

The proposed algorithm is focused on PV systems without power reserves, which means lower complexity and lower computational cost to process the algorithm. In the following Chapter, we move forward from the basic power curtailment into a more elaborate method that included MPPE. As will be discussed, by combining MPPE with fast-tracking power curtailment techniques, a PV system can be operated similar to a BESS unit, by becoming fully dispatchable while maintaining headrooms, and even able to provide FFR.

# Chapter 3

## Unified Power Curtailment Algorithm

This chapter presents an algorithm that combines a modified robust P&O-based FPPT technique with a real-time, curve-fitting based MPPE that can be applied to both single-stage and two-stage topologies. In this unified method, the oscillatory nature of the P&O is leveraged to provide a good measurement window for the curve-fitting, hence discarding the need for an external ripple. Furthermore, in this model, the estimation algorithm's results are used not only to provide power reserves, but also to improve the dynamic performance of the power setpoint tracking, enabling the PV system to provide FFR for enhanced grid support. One major advantage of this work compared to another well-known FFR algorithm in the literature [25] is that it does not require irradiance or PV cell temperature sensors as inputs. The main contributions of the work to the literature are summarized as:

- A unified power curtailment algorithm combining the robust setpoint-tracking performance from P&O-based FPPT methods with an accurate power reserves estimation via real-time curve-fitting, which can be used on both single and two-stage systems.

- A fast-convergence technique to adjust the PV power reserves within three iterations of the setpoint tracking algorithm.
- A mechanism to decouple the impact of irradiance changes from the iterations of the P&O technique, so that the relation between PV voltage and power is properly measured when under irradiance intermittency.
- A straightforward new design for the steady-state step of the adaptive FPPT to limit the output power ripple.

### 3.1 PV Array Modeling

The circuit and control system of a single-stage, three-phase PV system equipped with the proposed unified power curtailment algorithm is displayed in Fig. 3.1. The control structure and electrical components of this model are the same from the model introduced in Chapter 2. However, in this case, the power setpoint tracking algorithm is composed by a combination of a modified adaptive FPPT and a real-time, curve-fitting MPPE.

A PV array can be represented by the single-diode model introduced in [31] as shown in Fig. 3.2. The model can be described by the following equations as presented in [32].

$$I_{\text{pv}} = I_{\text{ph}} - I_{\text{D}} - I_{\text{Rsh}} \quad (3.1)$$

$$I_{\text{pv}} = I_{\text{ph}} - I_s \left( e^{\frac{V_{\text{pv}} + I_{\text{pv}} R_s}{a}} - 1 \right) - \left( \frac{V_{\text{pv}} + I_{\text{pv}} R_s}{R_{\text{sh}}} \right) \quad (3.2)$$

$$a = \delta_0 V_{\text{oc}0} \lambda T \quad (3.3)$$

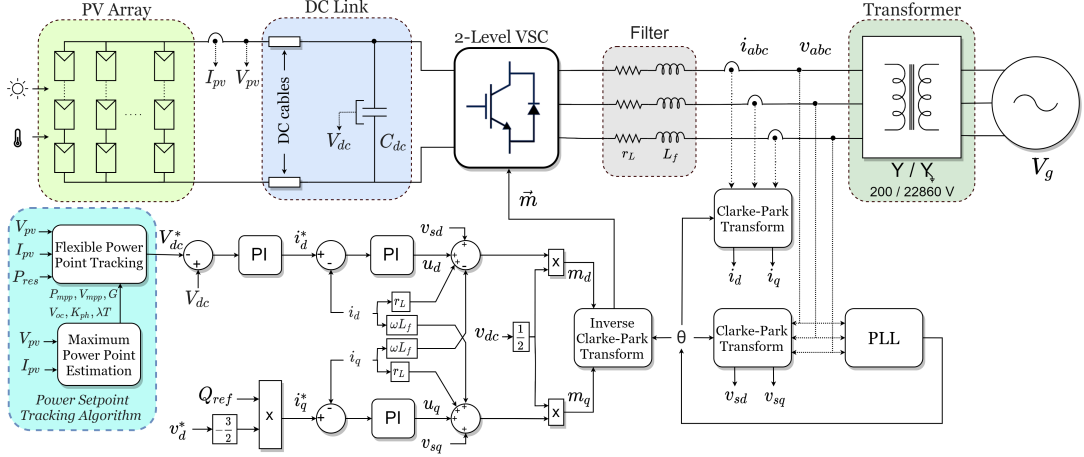


Figure 3.1: Circuit and control system block diagrams of a utility-scale PV system equipped with the proposed unified power curtailment algorithm.

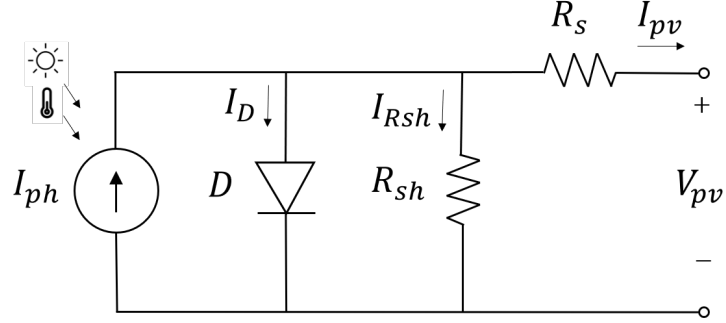


Figure 3.2: Single-diode PV model circuit.

$$R_s = [a_0(w_0 - 1) - V_{mp0}] / I_{mp0} \quad (3.4)$$

$$R_{sh} = \delta_0 V_{oc0}(w_0 - 1) / [I_{sc0}(1 - 1/w_0) - I_{mp0}] / G \quad (3.5)$$

$$I_{ph} = (1 + R_{s0}/R_{sh0}) I_{sc0} G [1 + \alpha_{Isc} T_0 (\lambda T - 1)] \quad (3.6)$$

$$I_s = I_{ph0} e^{-1/\delta_0} \lambda T^3 e^{47.1(1-1/\lambda T)} \quad (3.7)$$

$$\delta_0 = (1 - \beta_{\text{Voc}} T_0) / (50.1 - \alpha_{\text{Isc}} T_0) \quad (3.8)$$

$$w_0 = W\{e^{1/\delta_0 + 1}\} \quad (3.9)$$

$$a_0 = \delta_0 V_{\text{oc}0} \quad (3.10)$$

$$R_{\text{sh}0} = a_0(w_0 - 1) / [I_{\text{sc}0}(1 - 1/w_0) - I_{\text{mp}0}] \quad (3.11)$$

$$I_{\text{ph}0} = (1 + R_{\text{s}0}/R_{\text{sh}0})I_{\text{sc}0} \quad (3.12)$$

$$I_{\text{s}0} = I_{\text{ph}0} e^{-1/\delta_0} \quad (3.13)$$

By applying KCL to the circuit, the PV output current is defined as (3.2). The five parameters of the model are the ideality factor ( $a$ ), the series resistance ( $R_s$ ), the shunt resistance ( $R_{\text{sh}}$ ), the photocurrent ( $I_{\text{ph}}$ ), and the diode saturation current ( $I_s$ ). The five PV model parameters,  $a_0$ ,  $R_{\text{s}0}$ ,  $R_{\text{sh}0}$ ,  $I_{\text{ph}0}$ , and  $I_{\text{s}0}$ , are the baseline values calculated under the standard test conditions (STC). The equation for the series resistance at STC ( $R_{\text{s}0}$ ) is omitted since  $R_s = R_{\text{s}0}$ . From the manufacturer datasheet or measured in field at STC, the short-circuit current ( $I_{\text{sc}0}$ ), the open-circuit voltage ( $V_{\text{oc}0}$ ), and the voltage and current at MPP ( $V_{\text{mp}0}$ ,  $I_{\text{mp}0}$ ) can be obtained to calculate the five baseline parameters at STC and used in (10)-(13). After that, the five parameters at any irradiance and temperature can be calculated using (3)-(7). Note that  $G$  is the normalized irradiance, and  $\lambda T$  is the ratio between the cell temperature and its temperature at STC ( $T_0$ ),

corresponding to 298.15 K. Moreover,  $\delta_0$ , given by (3.8), is a ratio between the ideality factor and the open circuit voltage ( $V_{oc}$ ), whereas  $w_0$  is an auxiliary parameter related to  $\delta$  via the Lambert  $W$  function (3.9). In this work, the Lambert  $W$  function is solved with the method from [33]. In addition,  $\beta_{Voc}$  and  $\alpha_{Isc}$ , in (3.8), correspond to the temperature coefficient of the open-circuit voltage and short-circuit current, respectively.

## 3.2 Maximum Power Point Estimation

In this section we present a modified MPPE algorithm based on the methods introduced in [22] and [34]. By inserting (3.3)-(3.7) in (3.2), we obtain (3.14), which correlates the output voltage and current of a PV system with irradiance and temperature values. Then, by applying a non-linear least squares method to (3.14), it is possible to estimate the incident irradiance and temperature on the PV array from voltage and current measurements. In [22], good convergence was obtained via Levenberg-Marquardt (LM). Thus, the same algorithm is utilized in this work.

$$a_0 \lambda T \ln \left[ \frac{GI_{ph0} [1 + \alpha_{Isc} T_0 (\lambda T - 1)] - I_{pv} - G(V_{pv} + \frac{I_{pv} R_{s0}}{R_{sh0}})}{I_{s0} \lambda T^3 e^{47.1(1-1/\lambda T)}} \right] - V_{pv} - I_{pv} R_{s0} = 0 \quad (3.14)$$

The LM algorithm utilizes the damping parameter ( $\eta$ ) to adaptively vary the parameter updates between the gradient descent and the Gauss-Newton methods [35]. In (3.15),  $\mathbf{W}$  is the weighting matrix,  $(\mathbf{y} - \hat{\mathbf{y}})$  is the error between the measured data and the curve-fit function, defined by (3.14),  $\mathbf{J} = [\frac{\partial y}{\partial G} \quad \frac{\partial y}{\partial \lambda T}]^T$  is the Jacobian, and  $\boldsymbol{\delta}$  is the vector of parameters updates in each LM iteration. For each  $(V_{pv}, I_{pv})$  measurements added to the measurement window, the partial derivatives from the Jacobian are calculated. Once the measurement window is full, one iteration of the LM is performed with (3.16) and

(17).

$$\left[ \mathbf{J}^T \mathbf{W} \mathbf{J} + \eta \text{diag}(\mathbf{J}^T \mathbf{W} \mathbf{J}) \right] \boldsymbol{\delta} = \mathbf{J}^T \mathbf{W} (\mathbf{y} - \hat{\mathbf{y}}) \quad (3.15)$$

$$\boldsymbol{\Omega}_i = \begin{bmatrix} (1 + \eta) \sum_{n=1}^N \frac{\partial^2 y_n}{\partial \lambda T^2} & \sum_{n=1}^N \frac{\partial y_n}{\partial G} \frac{\partial y_n}{\partial \lambda T} \\ \sum_{n=1}^N \frac{\partial y_n}{\partial \lambda T} \frac{\partial y_n}{\partial G} & \sum_{n=1}^N (1 + \eta) \frac{\partial^2 y_n}{\partial G^2} \end{bmatrix} \quad (3.16)$$

$$\boldsymbol{\delta}_i = \begin{bmatrix} \Delta G_i \\ \Delta \lambda T_i \end{bmatrix} = \boldsymbol{\Omega}_i^{-1} \begin{bmatrix} \sum_{n=1}^N \frac{\partial y_n}{\partial G} (y_n - \hat{y}_n) \\ \sum_{n=1}^N \frac{\partial y_n}{\partial \lambda T} (y_n - \hat{y}_n) \end{bmatrix} \quad (3.17)$$

$$|\Delta G_i| \leq \Delta G_{\max}, |\Delta \lambda T_i| \leq \Delta T_{\max}$$

Because this is a real-time non-linear curve-fitting, irradiance intermittency and measurement noise can impact the algorithm's convergence. Therefore, this work proposes the addition of saturation factors ( $\Delta G_{\max}$ ,  $\Delta T_{\max}$ ) and a maximum irradiance threshold to the parameter updates from each LM iteration. The saturation factors and the irradiance threshold help to maintain the curve-fitting convergence in case of a poor measurement window. The saturation factors are defined based on the maximum expected changes in irradiance and temperature that may be experienced by the solar array, whereas the irradiance threshold is based on the maximum expected irradiance. References [36], [30], and [37] can be used for finding appropriate values. In this work, the estimated irradiance threshold is set to the nominal value of 1000 W/m<sup>2</sup>. However, this value can be boosted to higher limits such as 1100 or 1200 W/m<sup>2</sup> to account for edge-of-cloud lens effects.

Here, the following strategy is proposed for the update of the damping parameter

$(\eta)$ . First, the squared residual  $(\mathbf{y}_i - \hat{\mathbf{y}}_i)^2$  is compared for three different sets of damping values:  $a\eta$ ,  $\eta/a$ , and  $\eta$ . If the smallest residual is obtained by updating the parameters with a higher damping value, then the new damping value is set as  $a\eta$ . If the smallest is obtained by decreasing the damping, then the new damping is set as  $\eta/a$ . Otherwise, the damping value is maintained. Finding the best strategy for updating the LM damping parameter is a well-researched topic in the literature. The approach is normally heuristic-based. The strategy presented in this paper is similar to approaches found in [35], [38], and [39]. Besides, note that in this work the MPPE does not need an external ripple for achieving satisfactory curve-fitting performance. This is because the model is combined with a P&O-based technique, which naturally provides the necessary oscillation around the operating point for a measurement window with enough curve-length coverage.

Due to the high computational effort demanded by the curve-fitting, its period ( $T_{LM}$ ) must be large (e.g., 2-10 s). Consequently, the irradiance estimation may not provide adequate convergence when irradiance varies rapidly. To address this problem, we adopt an improved real-time curve-fitting technique introduced by Batzelis *et al.* in [34]. Assuming that changes in temperature are much slower than changes in irradiance,  $\lambda T$  can be considered as a constant between LM iterations. Thus, the irradiance can be directly calculated from voltage and current measurements using (3.18). With the estimated  $G$  and  $\lambda T$ , the PV voltage and current at MPP can be calculated by (3.19) and (3.20) [40], in which  $w$ , given by (3.21), is calculated with the Lambert  $W$  function.

$$G = \frac{I_{pv} + I_{s0}\lambda T^3 e^{47.1\left(1-\frac{1}{\lambda T}\right)} e^{\frac{V_{pv}+I_{pv}R_{s0}}{a_0\lambda T}}}{I_{ph0}\left[1 + \alpha_{Isc}T_0(\lambda T - 1)\right] - \frac{V_{pv}+I_{pv}R_{s0}}{R_{sh0}}} \quad (3.18)$$

$$V_{mp} = \left(1 + \frac{R_s}{R_{sh}}\right)a(w - 1) - R_s I_{ph} \left(1 - \frac{1}{w}\right) \quad (3.19)$$

$$I_{\text{mp}} = I_{\text{ph}} \left( 1 - \frac{1}{w} \right) - \frac{a(w-1)}{R_{\text{sh}}} \quad (3.20)$$

$$w = W \left\{ I_{\text{ph}} \frac{e}{I_s} \right\} \quad (3.21)$$

Figure 3.3 displays a flowchart of the proposed algorithm with the MPPE functionality highlighted in blue. Note that the proposed algorithm has three distinct iterative loops. The fast sampling loop runs every  $T_s$ , in which  $(V_{\text{pv}}, I_{\text{pv}})$  are sampled and added to a measurement window for calculating  $G$ , updating the sums from (3.16), and computing the residual (3.14). The medium-speed updating loop runs every  $T_{\text{step}}$ , in which the voltage reference for power setpoint tracking is updated. The slow updating loop runs every  $T_{\text{LM}}$ , in which the LM parameters in (17) are updated. In the first LM iteration, the temperature is initialized using its STC value obtained at 25°C ( $\lambda T = 1$ ). Note that the slow updating loop is triggered once the window storing  $(V_{\text{pv}}, I_{\text{pv}})$  measurements is full. It is worth mentioning that the matrix inversion from (17) can be algebraically derived beforehand to alleviate the computational burden.

Moreover, in each medium-speed updating loop, the irradiance decoupling method proposed in this work and the operating mode classification method introduced in [2] are executed. Then, the voltage reference is updated either by the rapid setpoint tracking (RST) technique, or by the P&O method (i.e., using the  $V_{\text{step}}$  introduced in [41]). The functionalities developed for the medium speed iteration will be explained in detail next.

### 3.3 Proposed Unified Algorithm

For the curve-fitting to converge, the data added to the measurement window must be distributed across a sufficient curve length; therefore, in [22], a duty-cycle ripple is added to the output of the dc-dc converter. For a small two-stage system this may have negligible

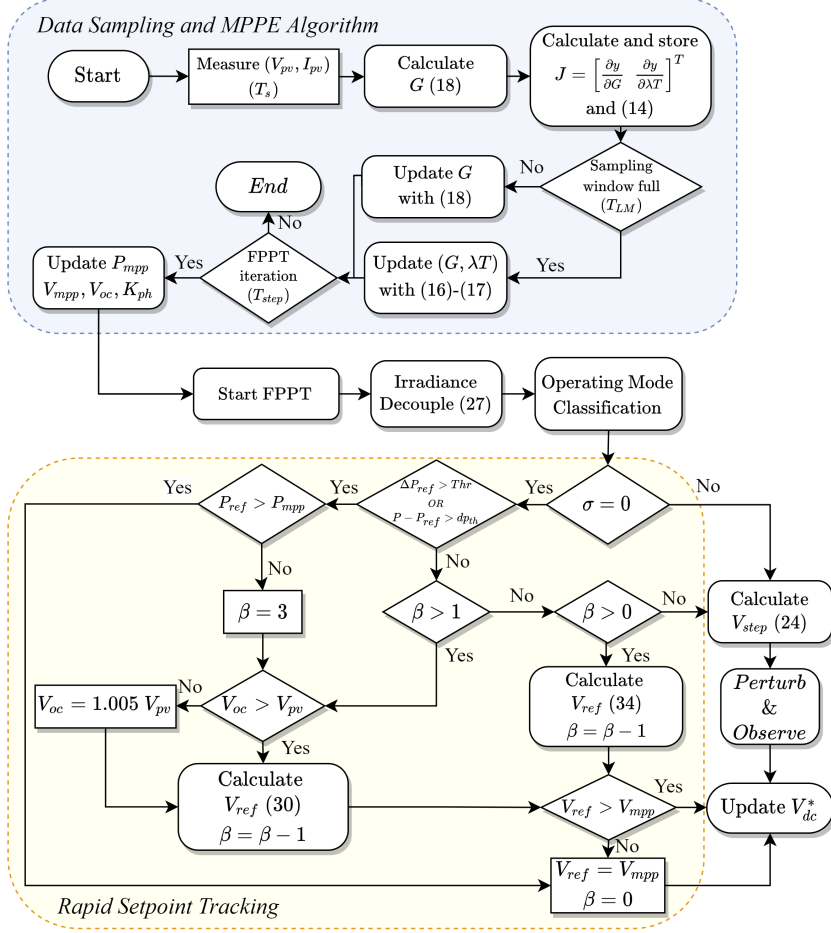


Figure 3.3: Flowchart of the unified power curtailment algorithm proposed.

impact, however, in larger systems with single-stage topologies, the ripple would need to be added directly to the dc-link, hence generating unwanted output power ripple that would reduce the power quality. As an alternative, here we propose the usage of a P&O-based method because it naturally perturbs the operating point to provide a variety of  $V_{pv}$  and  $I_{pv}$  for the measurement window. Furthermore, as discussed in the introduction, P&O based models present higher robustness over PI-based power controllers [26].

### 3.3.1 Power Tracking at Steady-State

In steady-state operation, the power-reference tracking algorithm normally adopts a small voltage step to reduce the steady-state output power ripple ( $\Delta P_{ss}$ ). However, the slope of the P-V curve (i.e.,  $\Delta P/\Delta V$ ) increases rapidly when the PV operation point passes the MPP and moves towards the right side of the P-V curve, as shown in Figs. 3.4(a) and 3.4(b). Thus, even if a small steady-state voltage step ( $V_{step-ss}$ ) is selected, the system may still experience a large  $\Delta P_{ss}$  due to the increased  $\Delta P/\Delta V$ , especially when a large power curtailment is required. To address this issue, in [2], Tafti *et al.* propose to use a variable voltage step,  $V_{step-ss}$ , which is calculated via a gain applied to the PV slope. This allows  $V_{step-ss}$  to be reduced continuously when the operating point moves further along the right side of the PV curve. However, no clear procedure for the design of the gain was proposed in the paper. Moreover, there is no direct control to reduce  $\Delta P_{ss}$ , leaving it varying with respect to solar irradiance. Therefore, we propose a new method for calculating  $V_{step-ss}$  as

$$V_{step-ss} = \max \left\{ \min \left[ \left| \frac{\Delta V}{\Delta P} \right| \Delta P_{max}, V_{step-b} \right], V_{step-min} \right\} \quad (3.22)$$

where  $V_{step-b}$  is the base voltage step,  $V_{step-min}$  is the minimum voltage step, and  $\Delta P_{max}$  is the maximum acceptable output power ripple.

As illustrated in Figs. 4(c) and 4(d), when  $\Delta P_{ss}$  is below the limit  $\Delta P_{max}$ , the step is fixed at its base value  $V_{step-b}$ . Then, as the voltage increases and the PV slope increases (Fig. 4(b)),  $V_{step-ss}$  is reduced as needed to maintain  $\Delta P_{ss}$  at  $\Delta P_{max}$ . Note that if the voltage step required to regulate  $\Delta P_{ss}$  is lower than the minimum acceptable value ( $V_{step-min}$ ),  $\Delta P_{ss}$  will no longer be maintained at  $\Delta P_{max}$ , causing it to increase as the operation moves further to the right of the PV curve. Therefore, the trade-off between  $V_{step-min}$  and  $\Delta P_{max}$  must be accounted for during implementation.

The main advantage of this method is that it provides a straightforward approach to limit the output power ripple. In contrast, the main disadvantage is that the output power ripple limit may cross  $\Delta P_{\max}$  if  $V_{\text{step-ss}}$  reaches  $V_{\text{step-min}}$ . To maintain control over the output power ripple throughout all ranges of operation, the desired range of  $V_{\text{step-ss}}$ , the PV array dc-ac power ratio, and the maximum acceptable power ripple at steady-state must be accounted during the design. During transients, the voltage step is calculated by the method introduced in Chapter 2 [41] by (3.23).

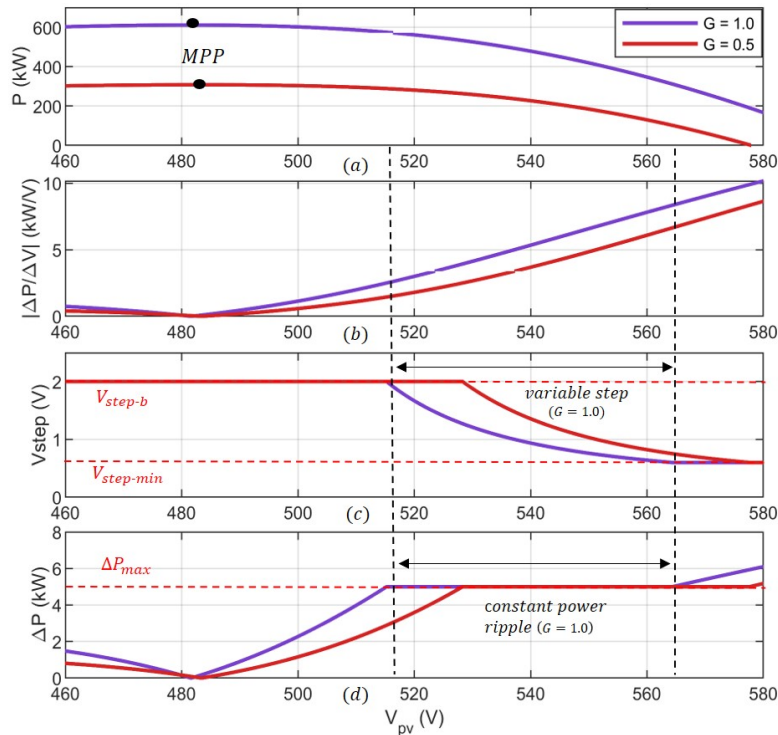


Figure 3.4: Illustration of the steady-state voltage step calculation strategy for a 612 kW PV system: (a) Power-voltage curve, (b) PV slope curve, (c) Steady-state voltage steps, (d) Expected output power ripples when using  $V_{\text{step-ss}}$  with  $\Delta P_{\max} = 5 \text{ kW}$ .

$$V_{\text{step-tr}} = \min \left\{ K_{\text{tr}} |P - P_{\text{ref}}|, V_{\text{step-max}} \right\} \quad (3.23)$$

$$V_{\text{step}} = \sigma V_{\text{step-ss}} + (1 - \sigma) V_{\text{step-tr}} \quad (3.24)$$

$$V_{\text{step}} = \begin{cases} V_{\text{step-ss}}, & \text{if } \sigma = 1 \\ V_{\text{step-tr}}, & \text{if } \sigma = 0 \end{cases}$$

where  $V_{\text{step-max}}$  is the maximum voltage step,  $K_{\text{tr}}$  is the gain applied to the error between the output power,  $P$ , and the specified power reference,  $P_{\text{ref}}$ . The classification between the steady-state and the transient modes is done via an auxiliary variable  $\sigma$ , by which  $\sigma = 1$  corresponds to the steady-state mode. The mode classification follows the strategy introduced in [2].

### 3.3.2 Irradiance Decoupling Technique

The P&O strategy decides what the next voltage step should be based on  $\Delta P$  and  $\Delta V$  measurements between iterations. However, the performance of this strategy is susceptible to irradiance changes. That is because the output power is affected by both the voltage change ( $\Delta V_{pv,n}$ ) and the irradiance change ( $\Delta G_n$ ) between iterations. Consequently,  $\Delta G_n$  will introduce an error when calculating the slope of the P-V curve. To address this issue, we introduce an irradiance decoupling method to remove the impact of  $\Delta G$  from the measured  $\Delta P$ .

When the PV system operates on the left side of the MPP,  $I_{pv}$  increases almost linearly with respect to  $G$ . This can be revealed by the following derivations. First, from (3.6), calculate the partial derivative of the photocurrent,  $I_{\text{ph}}$ , with respect to  $G$  by (3.25).

$$\frac{\partial I_{\text{ph}}}{\partial G} = (1 + R_{\text{s0}}/R_{\text{sh0}}) I_{\text{sc0}} [1 + \alpha_{\text{Isc}} T_0 (\lambda T - 1)] \quad (3.25)$$

Thus,  $\frac{\partial I_{\text{ph}}}{\partial G}$  can be considered as a constant assuming that  $G$  changes much faster than  $T$ .

Second, we define a relation between the photocurrent ( $I_{\text{ph}}$ ) and the PV output current ( $I_{\text{pv}}$ ) as the currents ratio  $K_{\text{ph}}$ , which is given by (3.2) and (3.6).

$$K_{\text{ph}} = \frac{I_{\text{pv}}}{I_{\text{ph}}} \quad (3.26)$$

Figure 3.5 shows the  $K_{\text{ph}}$  of a 500 kVA PV system for a wide range of voltage and irradiance values. According to the figure, for the same  $V_{\text{pv}}$  value, the ratio between  $I_{\text{pv}}$  and  $I_{\text{ph}}$  is nearly constant with respect to  $G$  when the system operates on the left side of the MPP (located around 480V). Thus, as  $I_{\text{ph}} = I_{\text{pv}}/K_{\text{ph}}$ , based on (3.25), we can show that the relationship between  $I_{\text{pv}}$  and  $G$  is approximately linear.

However, once the operation point passes the MPP (i.e., the PV system operates on the right side of the P-V curve),  $I_{\text{pv}}$  no longer linearly increases with respect to  $G$ . This can be observed by noticing that at same  $V_{\text{pv}}$  values,  $K_{\text{ph}}$  changes with respect to  $G$  (remember that  $K_{\text{ph}}$  is the ratio between  $I_{\text{pv}}$  and  $I_{\text{ph}}$ , and that  $I_{\text{ph}}$  is always linearly proportional to  $G$ ).

To address this issue, we first assume that if irradiance perturbations ( $\partial G$ ) are small (e.g., less than 40 W/m<sup>2</sup> per FPPT iteration),  $K_{\text{ph}}$  is constant at a given  $V_{\text{pv}}$  value. Note that for a small PV system with tens of panels, the irradiance change caused by a passing cloud can be 250 W/m<sup>2</sup>/s or more [36]. However, for a large solar farm with hundreds of panels, the irradiance change will be averaged over all panels, making the irradiance perturbations caused by passing clouds much slower than those in a small PV system [37]. Therefore, it is reasonable to assume that  $K_{\text{ph}}$  remains constant between FPPT iterations for larger PV systems.

To decouple the impact of irradiance changes from the PV power output, at iteration  $n$ , we will first calculate how much the photocurrent from the previous iteration would

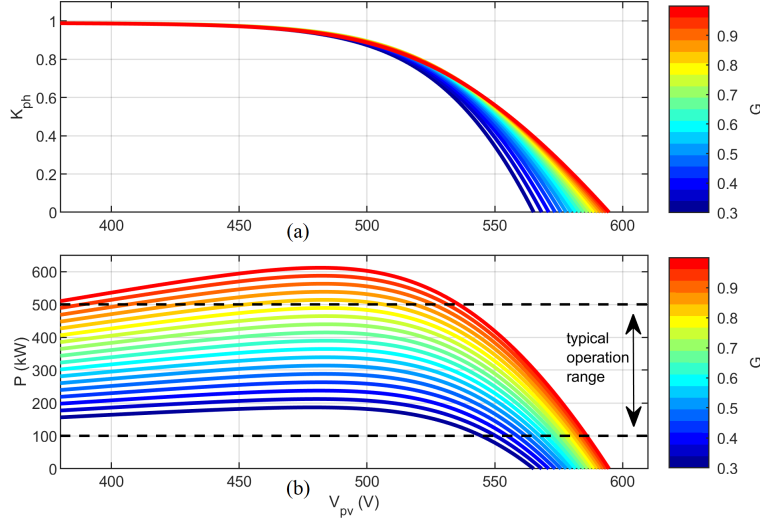


Figure 3.5: (a) Relation between  $K_{ph}$  and voltage for irradiance curves in steps of 40  $W/m^2$  (0.04 p.u.). (b) Power-voltage curves of a 500 kVA PV system under different irradiance levels.

be if subject to the new irradiance  $G_n$  using (3.25). Then, given an irradiance change of  $\Delta G_n = G_n - G_{n-1}$ ,  $\Delta I_{pv}$  can be calculated as

$$\Delta I_{pv}|_{\Delta G_n} \approx K_{ph,n-1} \Delta G_n \left( \frac{\partial I_{ph}}{\partial G} \right) \quad (3.27)$$

Note that it is crucial that  $K_{ph}$  from the previous iteration is used to exclude the impacts of  $\Delta V_n$ . This is because if we use the ratio from the present iteration, this ratio corresponds to  $I_{pv}/I_{ph}$  under a new voltage condition, thus  $I_{ph}$  is already impacted by voltage, and then we cannot find what's the impact of only irradiance. Same goes to  $I_{pv}$  values, by observing impact of  $\Delta G$  on previous  $I_{ph}$ , we can get  $dI_{pv}/dG$ , but if we observe the current iteration, we already have  $I_{pv}$  under a new voltage value.

When using  $V_{pv}$  and  $I_{pv}$  measurements to compute  $\Delta P_n$ , the impact of  $\Delta G$  is included. Thus, to calculate  $\Delta P_n$  without including the impact of irradiance changes,  $I_{pv}$  needs to be adjusted by  $\Delta G$  using (3.27), so we have

$$\Delta P_n = V_{pv,n} \left( I_{pv,n} - \Delta I_{pv}|_{\Delta G_n} \right) - V_{pv,n-1} I_{pv,n-1} \quad (3.28)$$

Simulation results of the method are presented in Section IV. Furthermore, a numerical example to better illustrate how the irradiance decoupling works is given next.

For example, a 500 kVA PV system with a 5 Hz FPPT is following a power setpoint of 200 kW. At iteration  $n$ ,  $G_n$  is calculated as 0.5 p.u. from (3.18), the available PV power (i.e.,  $P_{mpp}$ ) is 307.8 kW,  $V_{pv}$  is 546.6 V,  $\frac{\partial I_{ph}}{\partial G}$  is 1359.0 AW<sup>-1</sup>m<sup>2</sup> calculated from (3.25), and  $K_{ph,n}$  is 0.5386 calculated from (3.26). Then, at iteration  $n + 1$ , the irradiance increases at a rate of 200 Wm<sup>-2</sup>s<sup>-1</sup> (extreme case for a large PV array) so that  $G_{n+1} = 0.54$  p.u.. Then, calculated by (3.27),  $\Delta I_{pv}|_{\Delta G_n} = 29.27$  A. Therefore, the change of power due to irradiance change is calculated by (3.28) as  $\Delta P_n = 16.0$  kW.

Note that the proposed irradiance decoupling method performs better for slower irradiance variations or faster FPPT frequency. Thus, to meet the performance requirement, the minimum FPPT frequency should be designed considering the maximum expected  $\Delta G$  of the PV system. More details regarding the estimation of the maximum expected  $\Delta G$  based on the size of the PV array can be found in [37].

### 3.3.3 Rapid Setpoint Tracking

Next, the Rapid Setpoint Tracking (RST) method for achieving the PV system's voltage reference while maintaining power reserves is presented. This is a novel convergence strategy that can reach the power setpoint given to the PV system within three iterations of the setpoint tracking algorithm, as shown in Fig. 3.6.

At the beginning of each iteration, the open-circuit voltage of the PV system,  $\tilde{V}_{oc}$ , is estimated using the equation introduced in [42] as

$$\tilde{V}_{oc} = ka \ln\left(1 + \frac{I_{ph}}{I_s}\right) \quad (3.29)$$

Note that here we introduce a scaling factor,  $k$ , for enhancing the robustness of the algorithm and reducing the power overshoots. This is because if  $\tilde{V}_{oc}$  is higher than the actual open-circuit voltage of the PV system,  $V_{oc}$ , a large overshoot may occur. In this paper,  $k$  is set at 99%.

Then, as illustrated in Fig. 3.7, the voltage reference setpoint,  $V_{ref}$ , is calculated by (3.30), where  $V_n$  and  $P_n$  are measured PV voltage and power values at step  $n$ .

$$V_{ref,n+1} = V_n + \frac{(\tilde{V}_{oc} - V_n)(P_n - P_{ref})}{P_n} \quad (3.30)$$

Using  $V_{ref}$  calculated by (3.30), we can achieve fast convergence towards  $P_{ref}$  in the first two steps. However, because  $\tilde{V}_{oc}$  will include estimation error, and because the use of  $k$  for improving robustness may introduce additional error, the convergence slows down at the third step. Therefore, a different strategy for calculating  $V_{ref,n+1}$  is needed in the third step to reduce the impact of estimation error and quickly converge to  $P_{ref}$ . Thus, at the beginning of the third step, an artificial step ( $V_\delta$ ) is first calculated using the  $\frac{\Delta P}{\Delta V}$  slope measured in the previous iteration, i.e., iteration  $n + 2$  of the fast-convergence method, as

$$V_\delta = \frac{(V_{n+2} - V_{n+1})(P_{ref} - P_{n+2})}{(P_{n+2} - P_{n+1})} \quad (3.31)$$

Subsequently, to account for the non-linearity on the right side of the P-V curve, we use the first-order Taylor series approximation to estimate the increase in the slope of the P-V curve when the  $V_\delta$  step is applied by

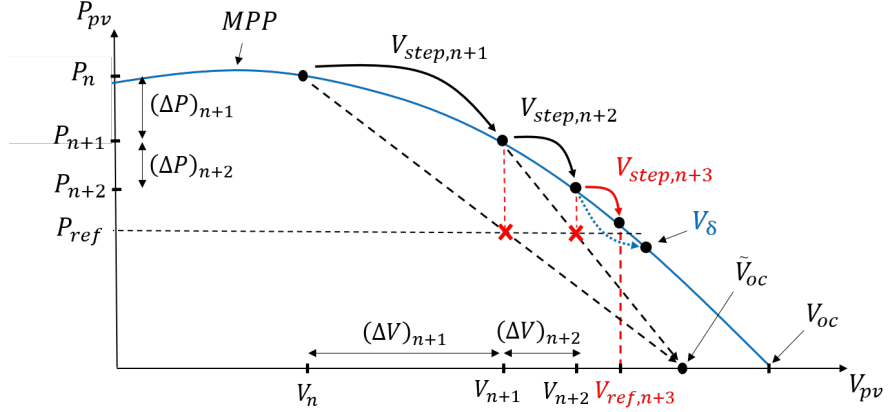


Figure 3.6: Sequence of steps of the RST algorithm. Note that slope at  $V_\delta$  is used for calculating  $V_{step,n+3}$ . The figure is not to scale.

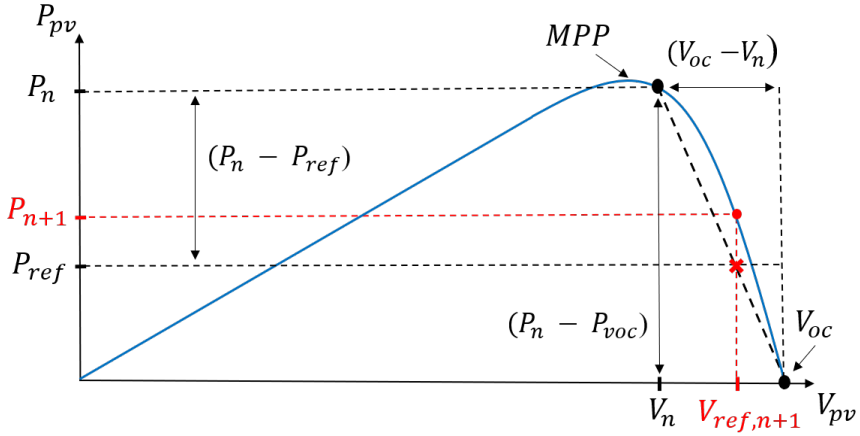


Figure 3.7: Calculation of  $V_{ref}$  in the first step of the RST algorithm.

$$\left(\frac{\Delta P}{\Delta V}\right)_\delta = \left(\frac{\Delta P}{\Delta V}\right)_{n+2} + \left[ \frac{\left(\frac{\Delta P}{\Delta V}\right)_{n+2} - \left(\frac{\Delta P}{\Delta V}\right)_{n+1}}{V_{n+2} - V_{n+1}} \right] V_\delta \quad (3.32)$$

Then, the actual voltage step for iteration three,  $V_{step,n+3}$ , can be calculated by (3.33), and the voltage reference is updated by (3.34).

$$V_{step,n+3} = (P_{n+2} - P_{ref}) \left| \left(\frac{\Delta V}{\Delta P}\right)_\delta \right| \quad (3.33)$$

$$V_{\text{ref},n+3} = V_{n+2} + V_{\text{step},n+3} \quad (3.34)$$

After the third iteration, the RST algorithm will be terminated, and the tracking mechanism returns to the P&O-based technique. The RST algorithm can be terminated before the three-step convergence ends under the following two conditions:

1. At any step, if  $V_{\text{ref}} \leq V_{\text{mpp}}$  (which may happen if the power setpoint is larger than the available PV power), the new voltage reference is set as  $V_{\text{mpp}}$ . This condition is specifically set for a system operating on the right-side of the MPP. Note that for systems designed to operate on the left side, the condition must be changed to  $V_{\text{ref}} \geq V_{\text{mpp}}$ .
2. The operating mode is classified as steady-state (i.e.,  $\sigma = 1$ ).

Moreover, if at any iteration  $V_{\text{pv}}$  is greater than  $\tilde{V}_{\text{oc}}$  because of the safe margin added, which could happen under high irradiance and very high levels of power curtailment (under 0.1 p.u.), then  $\tilde{V}_{\text{oc}}$  is set as  $1.005 \times V_{\text{pv}}$ . This setup will ensure  $\tilde{V}_{\text{oc}} > V_{\text{pv}}$  in order to prevent the algorithm from mistakenly stepping towards higher voltage values and ceasing the power generation of the PV array.

Note that the system should not always be in RST. This is because a good measurement window is needed for the estimator to converge based solely on voltage and current measurements. If all measurements are concentrated within a small operating region, the curve-length coverage will be insufficient, leading to a degradation in convergence performance. Therefore, the algorithm is set to operate under the P&O mode when fast convergence is not needed. By leveraging the oscillatory performance of P&O, we demonstrate that it is possible to maintain a good measurement window to achieve sufficient convergence.

## 3.4 Real-Time Simulation Results

To validate the proposed algorithm, a testbed of a 500 kVA PV system is set up in an OPAL-RT real-time simulation platform. One-second resolution data collected from a 1.04 MW solar farm by EPRI is used [30]. This publicly available data set provides 9 days-long, high-resolution measurement data collected from PV systems ranging from 0.18 to 1040 kW. The simulation timestep is 50  $\mu$ s. To account for measurement noise from the dc sensors, Gaussian noises are added to  $V_{\text{pv}}$ ,  $I_{\text{pv}}$ , and  $V_{\text{dc}}$ , following the SNR ratio from a TI AMC1303 sensor [43]. The simulation parameters are given in Table 6.1, in the appendix.

### 3.4.1 MPPE Performance

To evaluate the performance of the MPPE, the PV system is set to operate for 10 hours with a fixed 200 kW headroom under two different types of environmental conditions: sunny and cloudy days. Figures 3.8 and 3.9 present the performance of the MPPE algorithm from each case. A histogram of the estimation error obtained with a sampling rate of 10 Hz is also displayed for the sunny day test.

An RMSE of 7.1 W/m<sup>2</sup> is obtained for the irradiance estimation during a sunny day, whereas an RMSE of 14.1 W/m<sup>2</sup> is obtained during the cloudy day. As expected, the estimated irradiance and temperature RMSE is greater in cloudy days due to faster environmental changing conditions, yet, the MPPE can successfully maintain an adequate estimation, and more importantly, the estimator does not lose convergence throughout this extreme case. A comparison between the actual MPP and the estimated MPP is displayed in Fig. 3.10.

In practice, the base values of the five parameters of the single-diode PV model ( $a_0$ ,  $R_{\text{s}0}$ ,  $R_{\text{sh}0}$ ,  $I_{\text{ph}0}$ , and  $I_{\text{s}0}$ ), corresponding to STC, are also calculated based on measurements

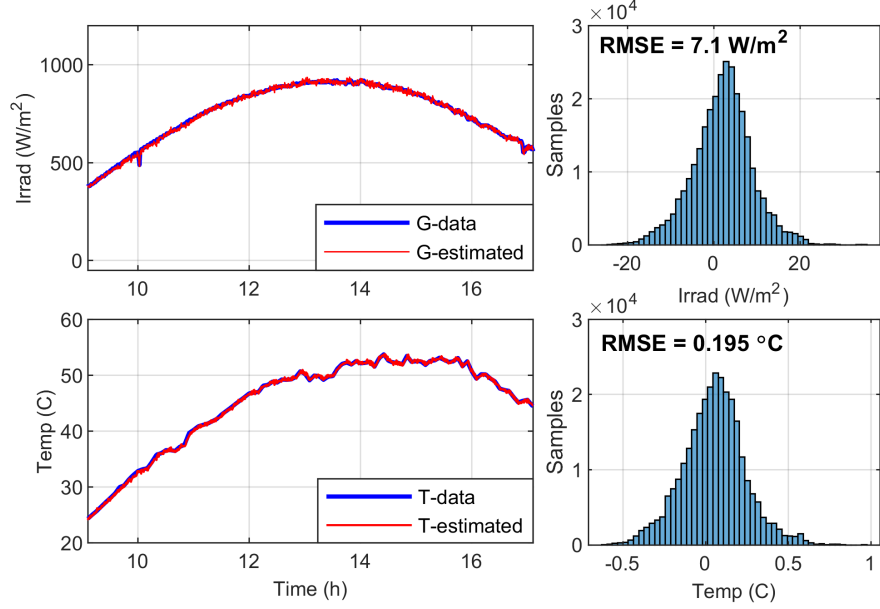


Figure 3.8: Performance of the MPPE algorithm in a sunny day (Sampling rate: 10 Hz).

of short-circuit current ( $I_{sc0}$ ), open-circuit voltage ( $V_{oc0}$ ), voltage at MPP ( $V_{mp0}$ ), and current at MPP ( $I_{mp0}$ ) instead of obtaining ( $I_{sc0}$ ,  $V_{oc0}$ ,  $V_{mp0}$  and  $I_{mp0}$ ) from datasheet information. Therefore, we first add  $\pm 5\%$  error to each PV parameter base value and redo the test for the cloudy days to simulate two worst case scenarios: significantly overestimate and under-estimate.

Furthermore, we also run a scenario in which it is assumed that a higher order optimization algorithm is used to update the PV parameters base values every five minutes, so that the parameter errors are constantly updated and maintained within 2% from the real values. For that case, a uniformly distributed random error of  $\pm 2\%$  is added to the base parameters every five minutes. The results are shown in Fig. 3.11. The results of the irradiance estimation under parameter errors are shown in Fig. 3.11(a).

Clearly, the worst case scenarios are when we over- or under- estimate the PV model parameter by 5% so that the estimated irradiance presents an offset (Fig. 3.11(b)). In such cases, the overall estimation RMSE is higher. However, if the PV model base parameter

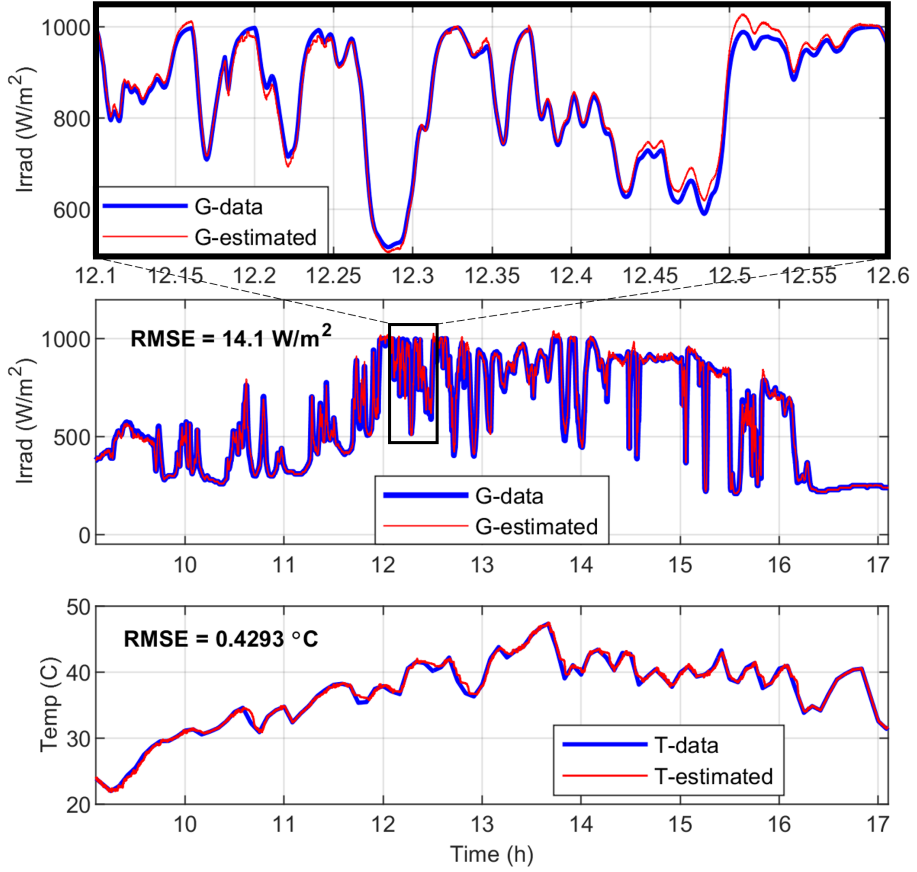


Figure 3.9: Performance of the MPPE algorithm in a cloudy day with estimated irradiance threshold set to  $1100 \text{ W/m}^2$ .

errors are maintained within  $\pm 2\%$ , the RMSE ( $16.2 \text{ W/m}^2$ ) is very close to the ideal parameter case ( $13.7 \text{ W/m}^2$ ). Therefore, it is important to perform PV model parameter correction periodically when applying the proposed algorithm.

In addition, the irradiance estimation error with respect to temperature and irradiance conditions are analyzed using results from six different daily irradiance patterns so that sufficient data points can be collected for different temperature and irradiance levels. As shown in Fig. 3.12, the estimation error is higher at higher irradiance values, and the irradiance change is above  $3 \text{ W/m}^2/\text{s}$ . This is because those time periods with low irradiance changes typically represent overcast and sunny weather conditions, when

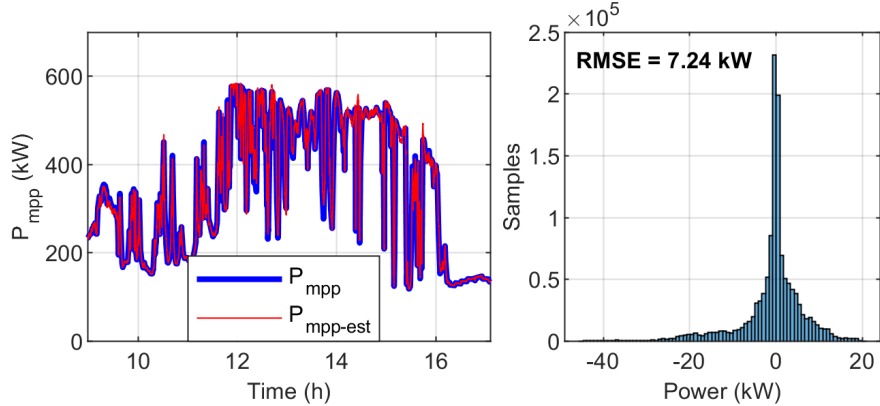


Figure 3.10: Comparison between the actual MPP and the estimated MPP for a cloudy day. (Sampling rate: 40 Hz)

forecasting results are consistent. The results also show that the MPPE estimation error does not have obvious correlation with temperature.

### 3.4.2 Irradiance Decoupling Performance

Next, we evaluate the accuracy of the irradiance decoupling method. As previously explained, the decoupling method is used to estimate how much of the measured  $\Delta P$  at a given iteration corresponds to irradiance changes ( $\Delta G$ ), which can be calculated by  $V_{pv} \Delta I_{pv}|_{\Delta G}$  using (3.28). For this test, the FPPT frequency is set as 4 Hz. Figure 3.13 presents three plots to analyze the performance of the irradiance decoupling technique: (i) a comparison between the calculated  $\Delta P$  caused by  $\Delta G$  in each FPPT iteration with its actual value while the system operates under 5% parameter errors, (ii) a comparison between the estimated irradiance data with the actual irradiance, which presents larger errors due to the 5% parameter error inserted, and (iii) a comparison between the actual constant  $K_{ph}$  and its estimated value. It is worth mentioning that the error in the estimated  $K_{ph}$  is caused by errors in the estimated photocurrent  $I_{ph}$ . Nevertheless, from the histogram of the first plot, it can be seen that overall the decoupling irradiance technique presents a satisfactory performance.

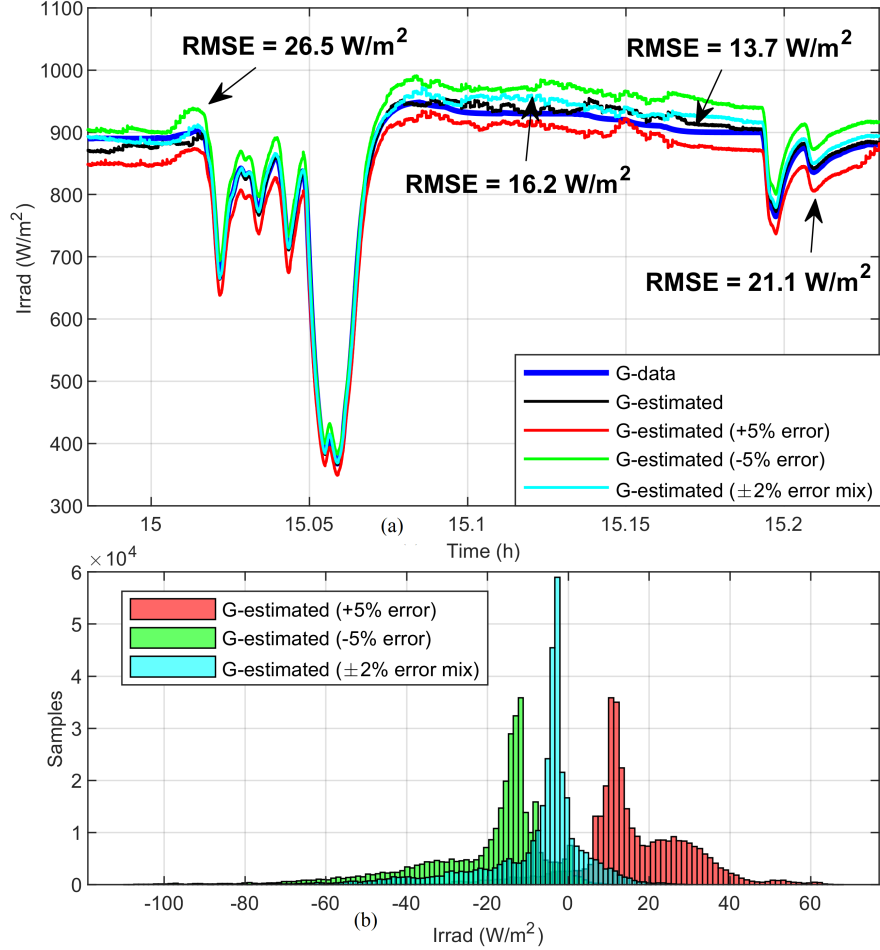


Figure 3.11: Performance of the MPPE algorithm in a cloudy day considering PV model parameter errors (Sampling rate: 10 Hz).

In addition, notice that the errors from the irradiance estimation do not directly affect the decoupling technique. That is because the decoupling method accounts only for the change in irradiance. The accuracy of the results confirms the assumption that  $K_{\text{ph}}$  can be considered constant in the subsequent step due to the small  $\Delta G$  between iterations. It must be mentioned that a low-pass filter is applied to the estimated irradiance and temperature values used by the irradiance decouple technique. Because the temperature update in the LM iteration is much slower than that in the irradiance decouple method, adding the filter can effectively prevent sudden changes caused by step changes in the LM

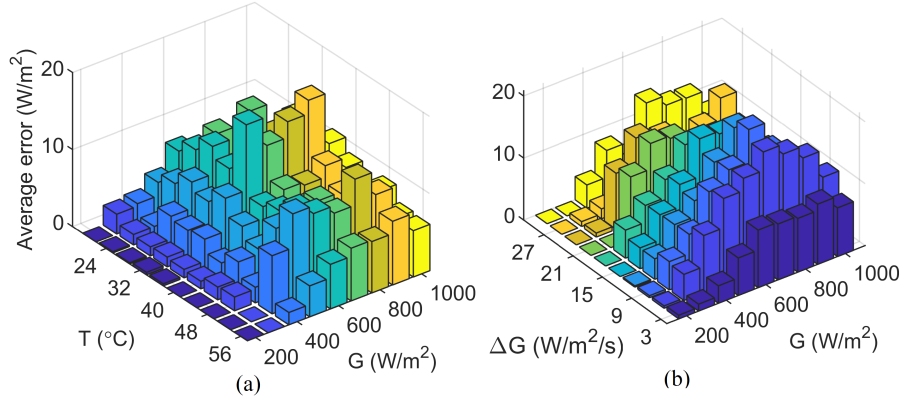


Figure 3.12: Irradiance estimation error with respect to: (a) temperature and irradiance, (b) irradiance changes ( $\Delta G$ ) and irradiance.

iterations from propagating to the irradiance decoupling technique. Therefore, the impact of the last temperature update will not lead to changes in temperature between the last two iterations in the irradiance decouple technique. For the estimated temperature, a filter with bandwidth 1-10 times slower than the frequency of the LM updates provided reasonable results. A good value for the filter utilized for the estimated irradiance can be found in [37].

### 3.4.3 Rapid Setpoint Tracking Performance

To analyze the performance of the RST algorithm when providing regulation services, we let the PV system follow a sequence of power setpoint changes while undergoing irradiance variations (i.e. MPP is varying). The PV system has a power setpoint tracking FPPT with identical settings from Table 6.1. Two cases are modeled: one with the proposed RST and the other with the adaptive FPPT (the state-of-the-art). The tracking errors (T.E.) of the two algorithms are calculated using the method presented in [41] and the power setpoint tracking results are shown in the bottom two plots in Fig. 3.14.

The simulation results demonstrate that RST can closely track power setpoint changes while the adaptive FPPT shows significant delays. This is because the later calculates

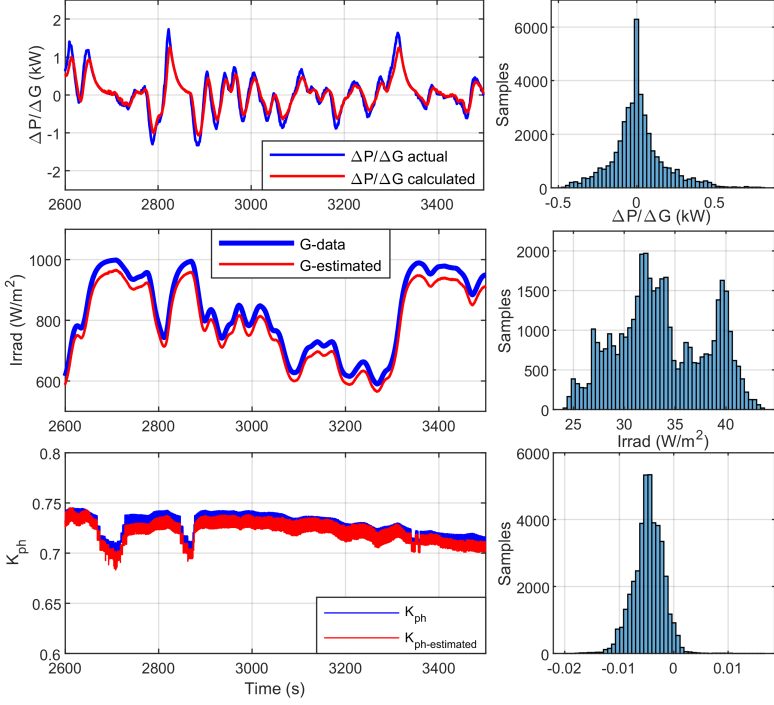


Figure 3.13: Performance of irradiance decouple method under 5% parameter error. (Sampling rate: 40 Hz)

the voltage step in proportion to the error between its output power and the given power setpoint. Therefore, when the error decreases, the step size also decreases, slowing down the convergence towards the end of the process. Using the 3-step convergence strategy, RST achieved a much faster convergence speed.

### 3.4.4 PV-Based Fast Frequency Response Service

One of the main applications of the proposed unified MPPE and FPPT control is to enable PV plants to provide high-quality, FFR services. To demonstrate the performance of the PV-based FFR, the black start process of an islanded feeder-level microgrid is modeled on the OPAL-RT eMEGASIM platform. The microgrid, displayed in Fig. 3.15, is powered by a utility-scale PV plant with 4 identical 612-kW PV arrays and a 3.125-MVA diesel generator. The system parameters are listed in Table 6.1. The feeder is

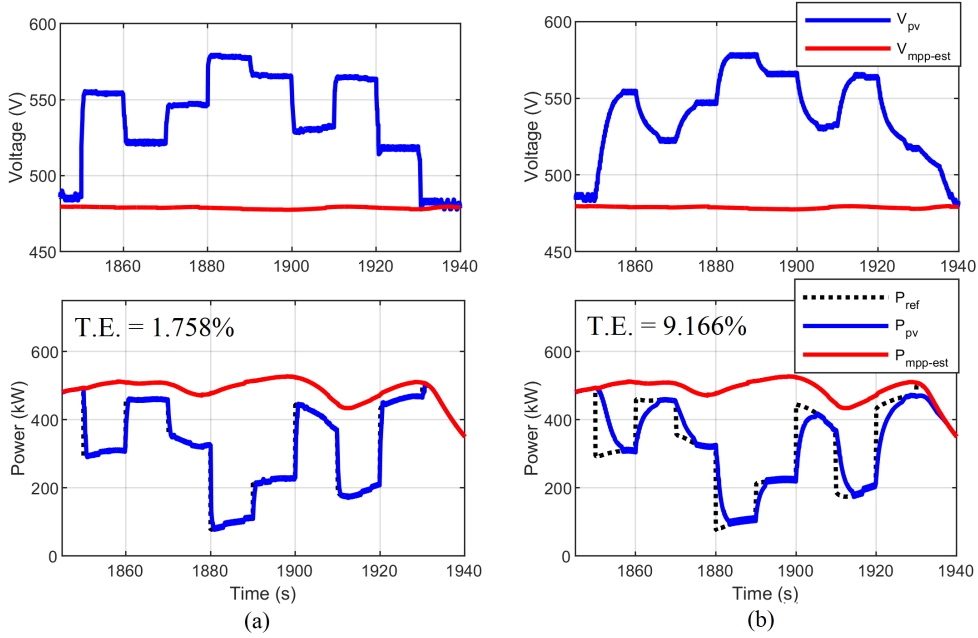


Figure 3.14: Comparison of the power setpoint tracking performance under irradiance intermittency between (a) the proposed RST method and (b) the adaptive FPPT (state-of-the-art).

divided into five load groups, each supplying 0.5 MVA loads. The cold-load pickup effect of each load group is modeled using the delayed exponential method introduced in [44], which can double the load of each load group to 1 MVA during the initial transients. In this case, we set the FPPT frequency to be 10 Hz. Note that typically, to achieve satisfactory performance, the FPPT/MPPT bandwidth is set between 1 to 10 Hz [45]. Moreover, note that the PV plant controller sends individual power commands ( $P_{\text{res}}$  or  $P_{\text{ref}}$ , and  $Q_{\text{ref}}$ ) to each inverter of the plant.

After the first two load groups have been picked up, the PV plant power setpoint is set to be 1 MW to maintain 1 MW of power reserves. Then, the microgrid controller dispatches the 1-MW PV power reserves to reduce the frequency nadir during the second cold-load pickup procedure, in which load groups 3 and 4 are connected to the microgrid. It is assumed that during the load pick-up coordination, the microgrid controller considers the communication delay, i.e., how long it would take between issuing the commands to

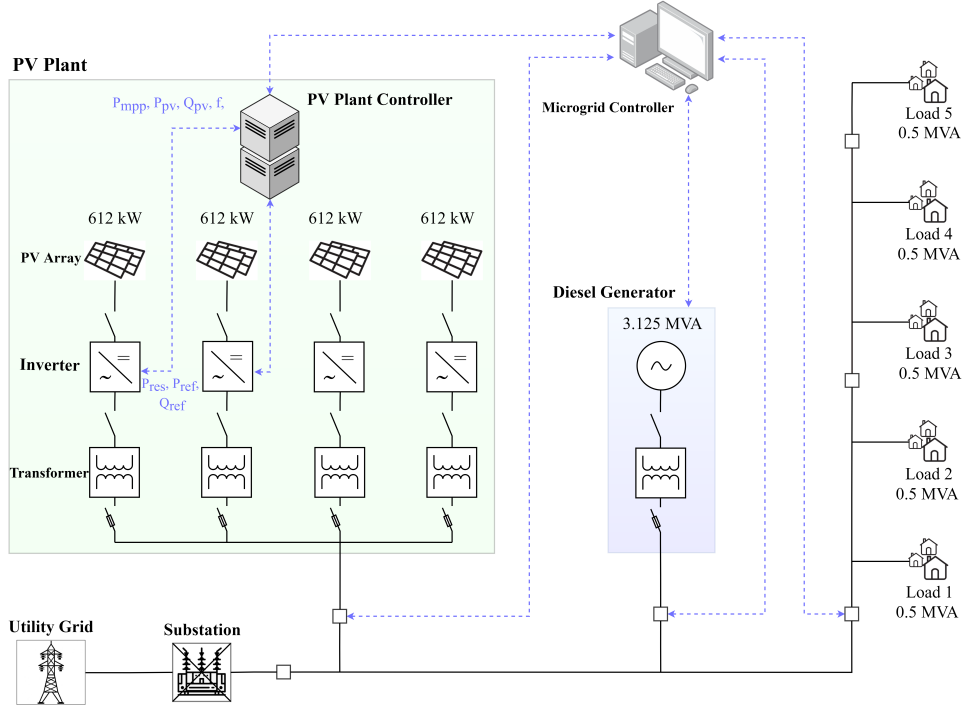


Figure 3.15: Configuration of a feeder-level microgrid.

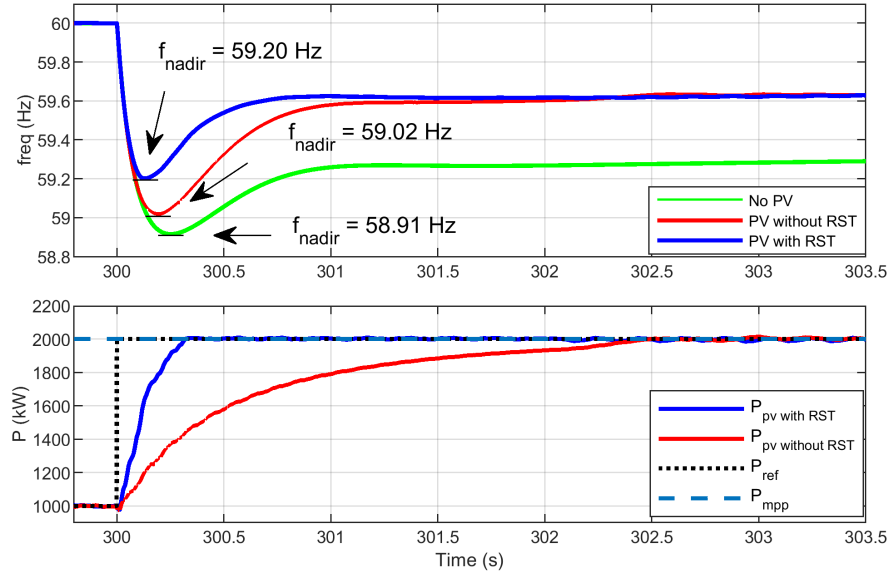


Figure 3.16: Frequency and voltage plots during microgrid cold-load pickup.

the relays and PV plant controller via MODBUS, and their execution time. As shown in Fig. 3.16, the proposed method outperforms the state-of-the-art method by reducing the

frequency nadir during the cold-load pickup.

The IEEE Standard 1547-2018 expects PV inverters to provide frequency ride-through function when the rate of change of frequency (ROCOF) is 2 to 3 Hz per second depending on DER penetration levels. Note that large ROCOF events are uncommon in high-inertia grids but occur more frequently in low-inertia grids dominated by IBRs, as having been seen in the Hawaiian grid [46]. Therefore, in the next analysis we suppose the microgrid from Fig. 3.15 is connected to a low inertia grid susceptible to large ROCOF events with low frequency nadirs.

The frequency-watt droop of each PV inverter is set to 5% without a deadband, which corresponds to a PV power setpoint change of 1/3 p.u. per 1 Hz change in a 60 Hz grid. We test four cases: 1) ROCOF of 1 Hz/s and nadir of 58 Hz, 2) ROCOF of 2 Hz/s and nadir of 59 Hz, 3) ROCOF of 3 Hz/s and nadir of 58 Hz, and 4) droop response under rapid irradiance changes. As shown in Fig. 3.17, the PV farm is able to provide faster power setpoint tracking with the RST function.

The delay observed between  $P_{\text{ref}}$  and  $P_{\text{pv}}$  in Figs. 3.17(a) and 3.17(b) is caused by the low FPPT frequency (10 Hz), which cannot be increased further because of the need for decoupled bandwidths in hierarchical control systems [47]. Note that the delay between second 206 and 207 in Fig. 3.17(c) is caused by the RST activation delay. This is because the RST function is only activated when the operation mode is classified as transient (Fig. 3.3), the threshold of which is determined by the value of  $dp_{\text{th}}$ , given in Table 6.1. Once the RST is activated, the PV system will quickly track the droop command during frequency events. This use case demonstrates the importance of the RST function for improving grid resiliency in high solar participation grids. When operated with power reserves, the proposed algorithm allows utility-scale PV farms to follow frequency-watt droop response curves in high ROCOF events. This function is crucial for reducing the frequency nadir in low-inertia power grids.

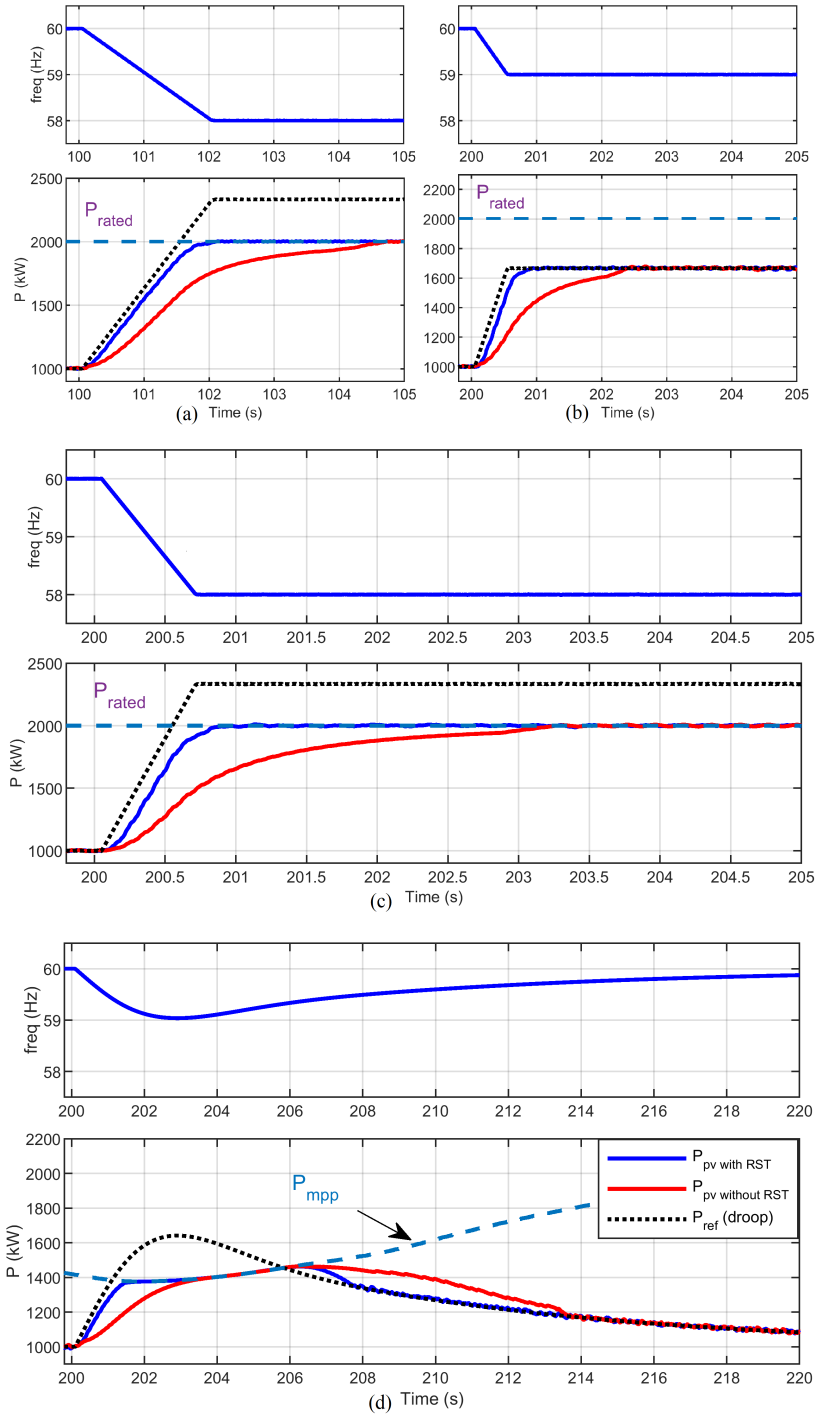


Figure 3.17: Frequency-watt droop responses of a PV plant. (a) Case 1: 1 Hz/s ROCOF and 58 Hz nadir. (b) Case 2: 2 Hz/s ROCOF and 59 Hz nadir. (c) Case 3: 3 Hz/s ROCOF and 58 Hz nadir. (d) Case 4: droop response in a grid disturbance under rapid irradiance changes.

### 3.5 Conclusion

Being able to closely follow power setpoints is an essential function for a PV system to provide grid services such as curtailment, spinning/non-spinning reserves, and FFR. Therefore, in this work, we combine MPPE and FPPT functionalities into a unified fast power setpoint tracking algorithm that significantly improves the performance of each functionality. Simulation results show that the proposed real-time, nonlinear curve-fitting MPPE estimates irradiance and temperature accurately even in the presence of modelling errors and measurement noises without the need for an external ripple. Moreover, the MPPE improves the P&O performance by decoupling the impact of the irradiance change from the PV output power. Finally, aided by MPPE, the proposed rapid setpoint tracking method can follow power setpoint changes in just three iterations, outperforming the state-of-the-art method.

# Chapter 4

## Novel Real-Time EMT-TS Modeling Architecture

As the participation of IBRs in the grid increases, new simulation methods that can integrate the fast response of power electronic devices must be developed [48]. Conventional transient stability (TS) software packages that run at the millisecond level are sufficient to simulate synchronous generator dynamic behaviors in a larger network. However, as synchronous generators are being displaced by energy systems powered by IBRs with advanced GSFs [41], [49], electromagnetic transient (EMT) simulations are required for capturing IBRs dynamic responses at the microsecond level.

EMT tools provide a greater depth of analysis for a wide frequency range, whereas TS is less accurate if there are high frequency dynamics in the grid. Nevertheless, the computational effort associated with EMT simulations make them an unviable solution when simulating realistic distribution networks [50]. Therefore, by integrating EMT-modeled power electronic systems into the TS-modeled power transmission and distribution networks, co-simulations can become a reliable alternative for modeling grids with high penetration of IBRs. As a consequence, the interest in EMT-TS co-simulations have

been growing in both industry and academia in recent years [51].

In addition, by developing co-simulation models in real-time simulators, hardware-in-the-loop (HIL) systems can be used to test protection schemes in large networks while including the dynamics of IBRs spread through the grid. Because an HIL testbed can also represent realistic communication links between distributed controllable devices and their centralized controllers, energy management systems (EMS) coordinating the operation of IBRs can be developed and tested in real-time or faster-than-real-time, day-long settings [52].

In [53], Mongrain *et al.* introduced a real-time simulation test system with established TCP/IP communication links on the eMEGASIM platform from OPAL-RT, but no phasor domain is included. A EMT-TS model built in MATLAB/Simulink is presented by Athaide *et al.* in [54], but it is not a real-time model. Researchers from RTDS Technologies recently presented a model with a real-time EMT-TS coupling via a Dynamic Phasor Line (DPL) [55]. However, the method requires the DPL to have a propagation delay larger than the EMT domain timestep with only a maximum of four coupling points allowed. Most importantly, there is a need for quantitative studies that can highlight how much information is lost by moving from an EMT model into an EMT-TS model, especially for real-time operation. In [56], Song *et al.* compared the co-simulation model with the network reduction model and analyzed the computational costs of the two methods. Still, not enough is presented related to the EMT and EMT-TS performance benchmarking.

To address the above issues, in this chapter, we present a novel real-time EMT-TS co-simulation modeling architecture, and conduct tests to validate the performance of the proposed testbed against an equivalent model built in EMT domain. This work framework presents the following contributions to the literature.

- Introduces for the first time in the literature a real-time EMT-TS testbed in which

the grid-forming unit is modeled in EMT domain, operating as the slack bus of the phasor domain including unbalanced voltage conditions.

- Analyzes the transient performance of the proposed model for different grid operation conditions, and compares the results with an equivalent model developed in EMT domain.
- Presents a coupling method for multiple coupling points between the EMT and phasor domains for moving devices across the feeder into the EMT domain.

## 4.1 Proposed EMT-TS Testbed Framework

Figure 4.1 displays the proposed EMT-TS testbed framework, which consists of a microgrid connected to a distribution feeder via a point of common coupling (PCC). The components are split into two subsystems. The first subsystem includes distributed energy resources, e.g., a grid-forming battery energy storage system (BESS), utility-scale PV systems, diesel generators (DGs), and a grounding transformer. This subsystem is simulated at the microsecond level in eMEGASIM. The second subsystem includes distributed rooftop PVs, shunt capacitor banks, voltage regulators, ZIP load models, and the unbalanced IEEE 123-bus network model [57] used to emulate the operation of realistic distribution feeders. The second subsystem is simulated in ePHASORSIM at the milisecond level. Note that a subsystem can be assigned to more than one core, if needed, but each subsystem requires at least one core for itself.

The EMS algorithms are running externally and can read measurements, set devices status, and send power setpoint commands using Modbus registers. Note that this is a function that a real-time simulation platform will normally provide for modeling communication links between the real-time simulator and an external computer.

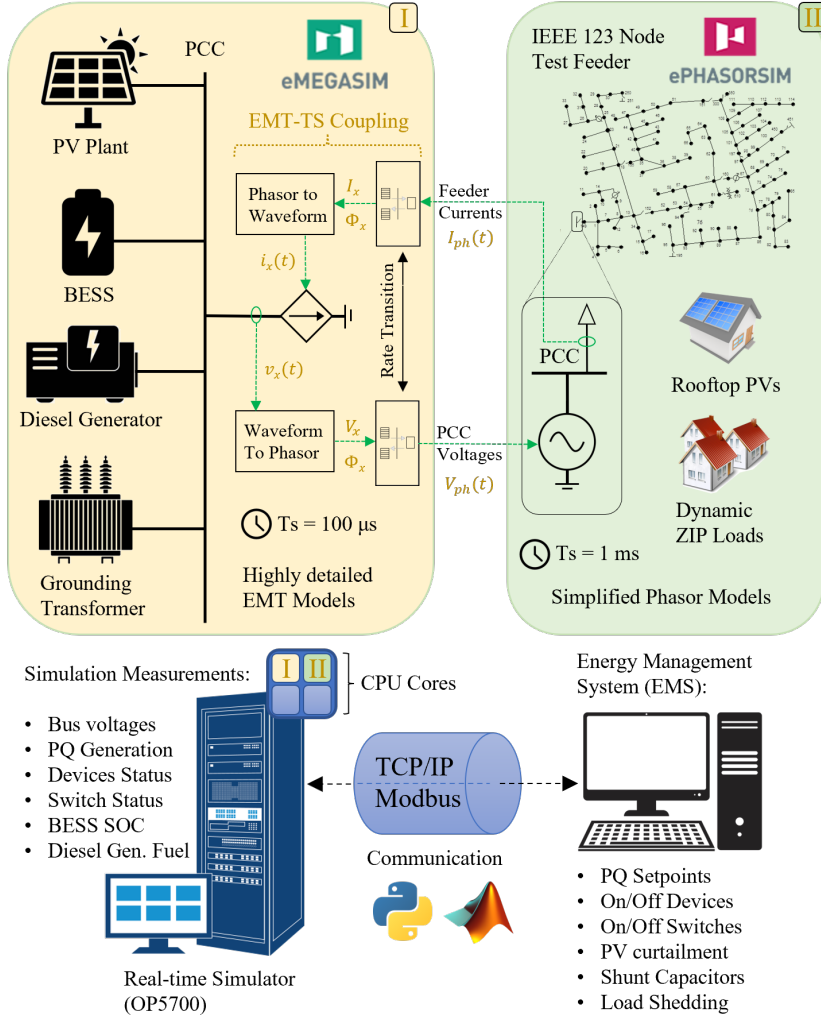


Figure 4.1: Proposed EMT-TS co-simulation testbed framework.

The ePHASORSIM solver allows grid models to be imported from CYME, PSS/E, or PowerFactory softwares. However, if using these imports, only three-phase balanced sources can be implemented in phasor domain for the EMT-TS coupling. Note that the 123-bus system was created in ePHASORSIM using an Excel file as the model file instead of using importing tools. This is because when using importing tools, only three-phase balanced sources can be implemented in phasor domain for the EMT-TS coupling. By describing the entire system with an Excel description file, the system presents a higher

customizability such as the capability of modeling unbalanced voltage sources in the phasor domain.

In the next section, the coupling between waveforms and phasors is explained.

## 4.2 EMT-TS Co-Simulation Coupling

Since both subsystems are simulated in parallel and exchange information with each other in real-time, there is a delay for events to propagate from one subsystem to another. In this paper, we introduce a coupling method in which the microgrid operates as the slack bus of the system, represented as a voltage source in phasor domain. This allows the simulation of feeder blackstart scenarios, in which a microgrid powered by BESS, utility-scale PVs, and/or DGs can be used for picking up sections of the feeder during system restoration.

### 4.2.1 Time Interpolation Coupling

Time interpolation is a commonly used technique for coupling EMT and phasor domains in co-simulations. The method consists of linearly interpolating both magnitude and phases of the signals coming from phasor domain for each EMT domain timestep [3]. Thus, in the proposed EMT-TS testbed, the distribution feeder is represented as a current source, with current magnitude ( $I_x$ ) and angle ( $\phi_x$ ) calculated from the phasor domain current ( $I_{ph}$ ) as follows.

$$I_x(t + nh) = |I_{ph}(t)| + \frac{n}{N} \left( |I_{ph}(t + H)| - |I_{ph}(t)| \right) \quad (4.1)$$

$$\phi_x(t + nh) = \angle I_{ph}(t) + \frac{n}{N} \left( \angle I_{ph}(t + H) - \angle I_{ph}(t) \right) \quad (4.2)$$

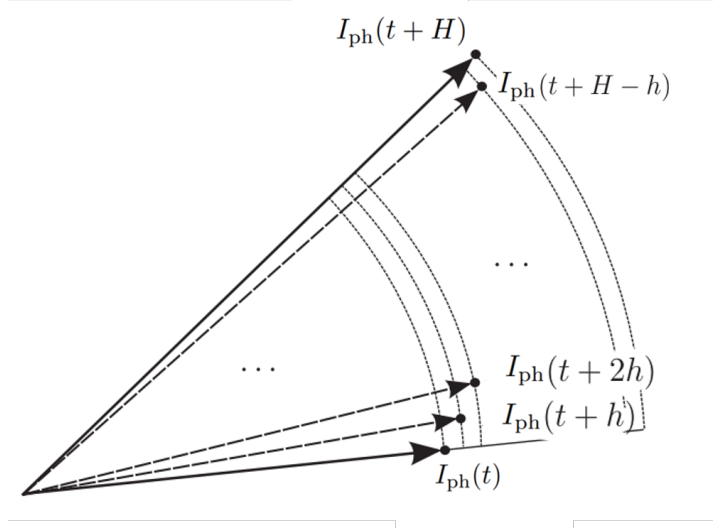


Figure 4.2: Time interpolation coupling technique from [3].

where the index  $x$  represents phases ( $a/b/c$ ),  $h$  and  $H$  correspond to the EMT and phasor timesteps, respectively,  $N = H/h$ , and  $n$  ranges from zero to  $N$ . Thus, the current waveform for each phase is obtained by (4.3).

$$i_x(t + nh) = \sqrt{2}I_x(t + nh) \cos [\omega_{\text{pcc}}(t + nh) + \phi_x(t + nh)] \quad (4.3)$$

where  $\omega_{\text{pcc}}$  is the angular frequency measured at the PCC with a phase-locked loop.

As will be shown in the simulation results section, the time interpolation coupling can smoothen the impact of fast current transients applied in the EMT domain, causing a larger deviation for the response between the EMT and EMT-TS testbeds. Therefore, instead of time interpolation, in this work, we directly update the waveforms with signals coming from the phasor domain with (4.4). In that case, to avoid numerical issues in the solver, a first-order low-pass filter with time constant equal to the EMT timestep ( $T_{s,\text{emt}}$ ) is applied on the recreated current signals. Moreover, due to the delay introduced by the filter, a feedforward compensation ( $T_{s,\text{emt}}$ ) is added to (4.4).

$$i_x(t) = \sqrt{2}I_x \cos [\omega_{\text{pcc}}(t + T_{\text{s,emt}}) + \phi_x] \quad (4.4)$$

### 4.2.2 Phasor Extraction

Phasor domain signals are obtained from the three-phase voltages measured at the PCC at a rate given by the phasor domain timestep ( $T_{\text{s,ph}}$ ). The voltages magnitudes are obtained with the true root mean square (RMS) value of the corresponding waveform, whereas the angles are obtained with its fundamental value, which can be obtained with Fourier analysis (4.7). Both the RMS and phase calculations are performed over a running average window of one cycle of the signal's fundamental period ( $T$ ).

$$a = \frac{2}{T} \int_{(t-T)}^t v(t) \cos(\omega_0 t) dt \quad (4.5)$$

$$b = \frac{2}{T} \int_{(t-T)}^t v(t) \sin(\omega_0 t) dt \quad (4.6)$$

$$\phi_{\text{ph}} = \text{atan}(b/a) \quad (4.7)$$

## 4.3 EMT Domain Benchmark Model

To benchmark the EMT-TS testbed performance, an equivalent EMT model with the same network parameters and loading conditions is built using the combined state-space nodal (SSN) modeling method introduced in [58]. SSN divides the state-space matrix utilized by Simulink's solver into separate matrices based on nodes defined by the user. As shown in Fig. 4.3, the nodal voltage error distribution between the EMT and EMT-TS testbeds is negligible in steady state operation with the maximum error below 0.0006

p.u. and the interquartile range within  $\pm 0.0003$  p.u.. In addition, the active and reactive power flow measured at the PCC (EMT-domain side) between both testbeds has the highest mismatch of 1.0 kW (on phase *b*) and 2.6 kVAR (on phase *a*) when supplying peak load. After the critical step of validating the steady-state operation, the dynamic behavior between the systems can be analyzed.

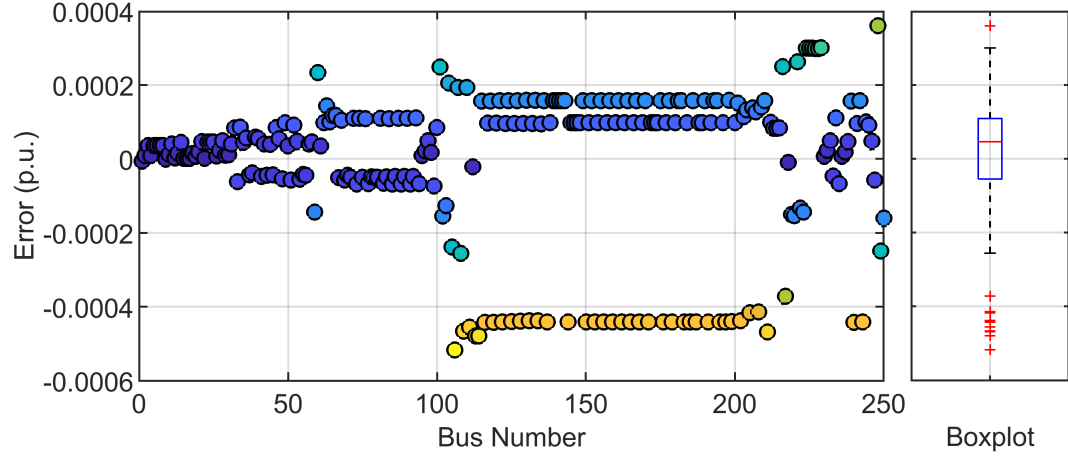


Figure 4.3: A comparison of the nodal voltage magnitude between the full EMT and EMT-TS testbeds.

Table 4.1: Power Flow Error at Steady-state

Load group	P <sub>error</sub> (kW)			Q <sub>error</sub> (kVAr)		
	A	B	C	A	B	C
I	-0.5	-0.37	-0.5	0.61	0.08	0.49
II	-0.7	-0.6	-0.8	1.1	0.52	1.1
III	-0.8	-0.8	-0.8	1.3	0.8	1.3
IV	-0.8	-0.9	-0.9	2.1	1.4	2.0
V	-0.8	-1.0	-0.9	2.6	1.5	2.2

## 4.4 Simulation Results

In this section, we present the following simulation results: (1) transient performance evaluation during load steps, (2) the impact of the TS domain timestep selection on

Table 4.2: Setup of Load Steps

Step	S (kVA)	P (kW)			Q (kVAr)		
		A	B	C	A	B	C
I	448	196	39	166	97	20	81
II	937	379	174	285	191	85	141
III	1978	734	490	640	378	243	324

propagation delays, (3) the impact of the time interpolation coupling, (4) a capacitor bank switching event, and (5) computational cost analysis.

#### 4.4.1 Transient Performance During Load Steps

The load steps applied during testing are presented in Table 4.2. Two different types of grid-forming units are analyzed: a 2-MVA BESS (parameters from [59]) and a 3.125-MVA diesel generator (parameters from [60]). The voltage and frequency transient responses of the proposed EMT-TS and the full EMT model are shown in Fig. 4.4. Note that a delay of 2 ms is added to the load steps in the EMT model so that the disturbances are applied at the same point-on-wave (POW) for both testbeds. The RMS error (RMSE) between EMT and EMT-TS curves is included in the figure of each test, with the highest RMSE value corresponding to the phase with the largest deviation.

Because the response of the DG is above the millisecond level, the modeling error of the EMT-TS testbed is negligible. For the BESS unit, the transient error is also negligible in the first load step-change (approximately 25% of the BESS rated power). In the second load step-change (approximately 50% of the BESS rated power), a maximum error of 0.006 p.u. is observed. During the third load step change (close to the BESS rated power), a maximum RMS voltage error of 0.03 p.u. is observed. Note that this is an extreme scenario and thus, represents the upper bound of the modeling error. It is worth mentioning that for the third load step-change in the diesel generator scenarios,

(Fig. 4.4(c)), phase b (in red) presents a voltage rise at the beginning of the transient. This is because the large, unbalanced load step causes a numerical issue in the DG model. This can be fixed by changing the synchronous machine solver from trapezoidal non-iterative to backward Euler robust (or trapezoidal robust). However, trapezoidal non-iterative was the only solver compatible with the SSN modeling (from the EMT benchmark). Therefore, the solver is kept the same to ensure a consistent comparison between the two testbeds.

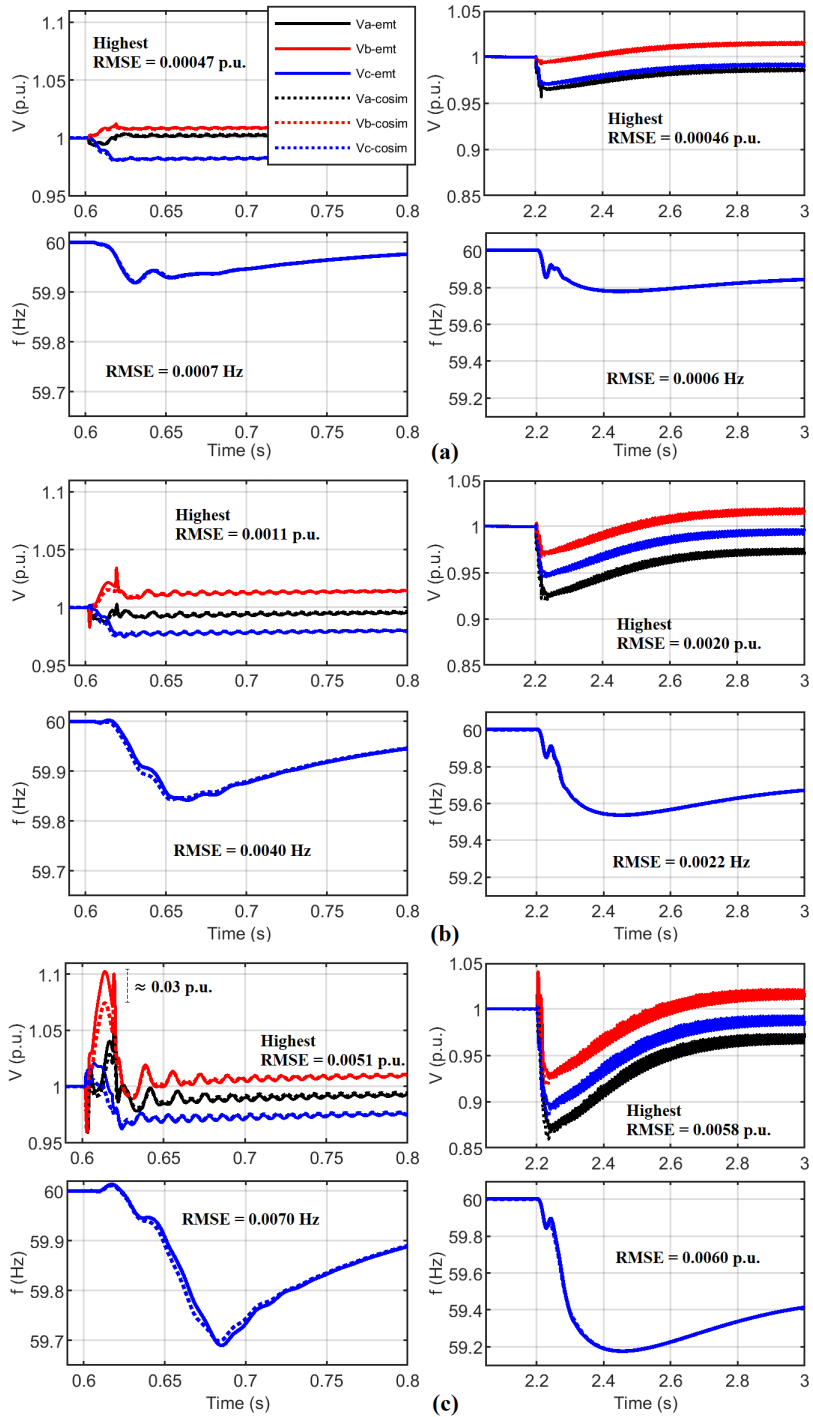


Figure 4.4: Transient response comparison between the EMT-TS and the EMT testbeds. Plots on the left: 2-MVA BESS. Plots on the right: 3.125-MVA diesel generator. (a) Load step change I; (b) Load step change II, and (c) Load step change III.

#### 4.4.2 Influence of Coupling Delay and Time Interpolation

We analyze the impact of (i) increasing the timestep of the phasor domain solver from the EMT-TS co-simulation from 1 to 10 ms, and (ii) utilizing the time interpolation coupling technique when coupling the EMT and phasor domain via voltage and current sources.

As discussed in [61], the propagation delay of events between the EMT and TS domains can be as high as  $(2T_{s,ph} + T_{s,emt})$ , where  $T_{s,ph}$  and  $T_{s,emt}$  are the timesteps of the phasor and EMT domains, respectively. Consequently, when the timestep from 1 to 10 ms, the maximum coupling delay between the EMT and co-simulation testbeds is also increased, reaching a maximum of 20.1 ms (from originally 2.1 ms). The delayed transient can be observed in Fig. 4.5(a). Furthermore, since the transient is affected by the point-on-wave (POW) from when the transient event is applied to the EMT domain, the voltage mismatch between the EMT and co-simulation testbeds will be affected accordingly.

Next, we analyze the impact of including the time interpolation coupling technique from [3] via equations (4.1)-(4.3). Figure 4.5(b) displays the transient response of the co-simulation testbed during the third load step when including the interpolation method described in Section II-C. Clearly, the interpolation considerably smoothed the response, causing a significant reduction of both voltage and frequency transients. This is an important finding that must be considered when developing a co-simulation testbed in which the grid-forming unit (or slack bus) is in EMT domain.

Based on the results, it is decided that the time interpolation coupling should not be used in this proposed testbed. Hence, the waveforms inserted in EMT domain are generated with (4.4).

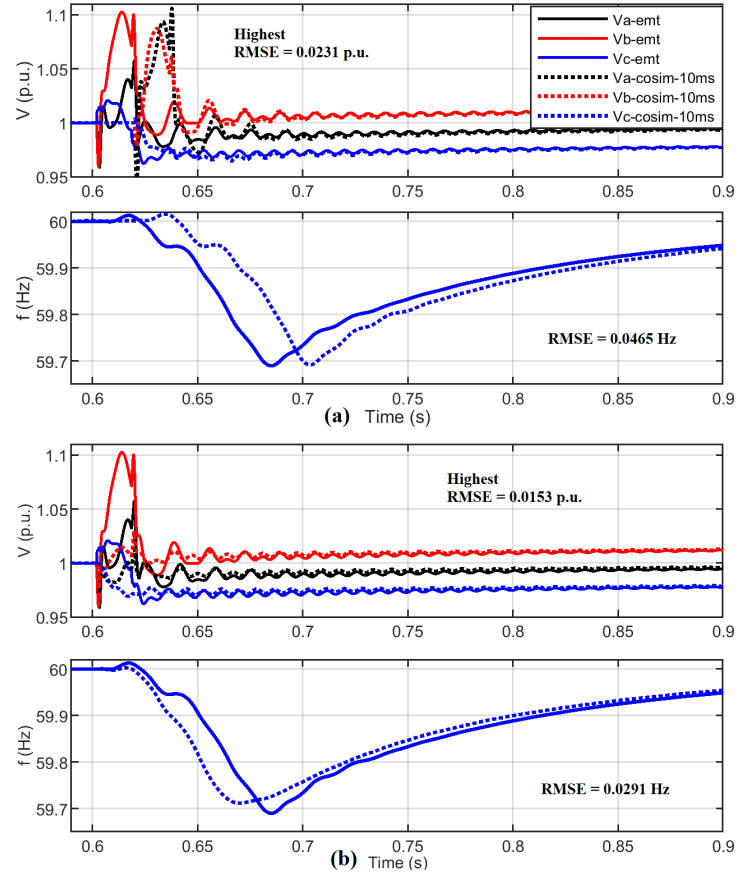


Figure 4.5: Voltage and frequency transient responses during Step III from Table 4.2 due to: (a) increasing the communication delay between EMT and phasor domains; (b) utilizing the time interpolation coupling technique

#### 4.4.3 Capacitor Switching Transients

In this test, we compare the transient performance between the testbeds for a capacitor switching transient event. Therefore, the shunt capacitor bank located at bus 83 from the IEEE 123 node test feeder is switched on. In EMT domain, the bank is modeled as ideal  $Y_g$  capacitances, whereas in the EMT-TS testbed it is modeled inside ePHASORSIM as shunt loads. Figure 4.6 displays the voltages at bus 83 when the capacitors are switched at (a) peak grid voltage (worst-case scenario), and (b) zero-voltage crossing (ZVC).

Evidently, the co-simulation does not capture the peak voltage of 1.6 p.u. observed in the EMT model in case (a). In fact, there is no significant difference between (a) or

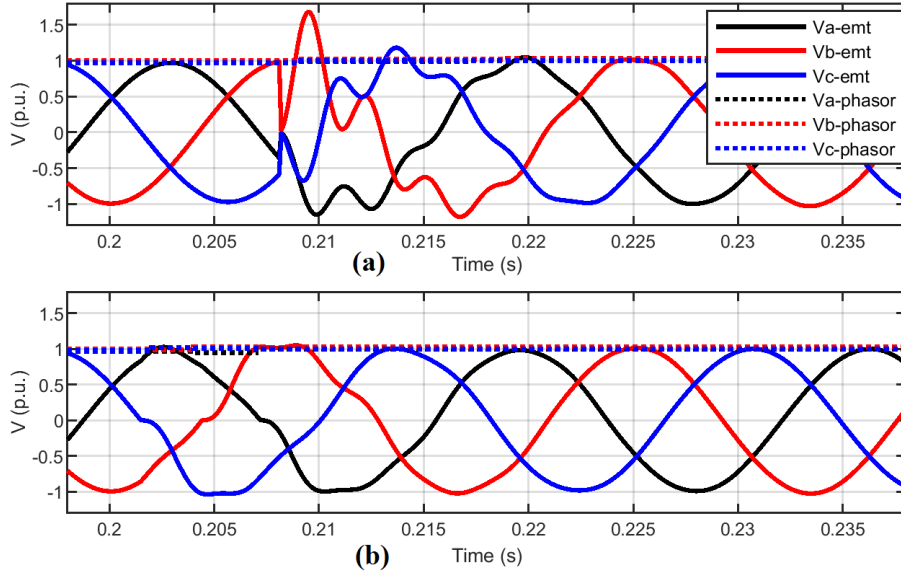


Figure 4.6: Capacitor bank switching event: (a) peak-voltage energization (worst-case scenario); (b) Zero-voltage-crossing energization.

(b) for the EMT-TS model. This is because the phasor domain solver does not simulate the differential equations that govern the electromagnetic transient behavior of capacitors. Nevertheless, if we assume that the capacitor bank of the system in study contains protective measures such as ZVC, the co-simulation can be utilized. This is a reasonable assumption since capacitor switching without protective measures can permanently damage electrical equipment due to overvoltage. Next, we present a method to further improve the performance of the co-simulation for case (b).

By adding a second EMT-TS coupling (at bus 83), the capacitors can be modeled in the EMT domain as  $Y_g$  capacitors, instead of being simulated as shunt loads in the phasor domain of the co-simulation testbed. First, the equivalent impedance between the feeder head and bus 83 is found, and a series RLC circuit is built. Then, the domains are coupled by (i) inserting a voltage source in EMT domain based on voltage phasors measured at bus 83, and (ii) inserting a current source to bus 83 of the phasor domain

corresponding to the capacitors' currents in EMT domain. This multi-EMT-TS coupling strategy is depicted in Fig. 4.7.

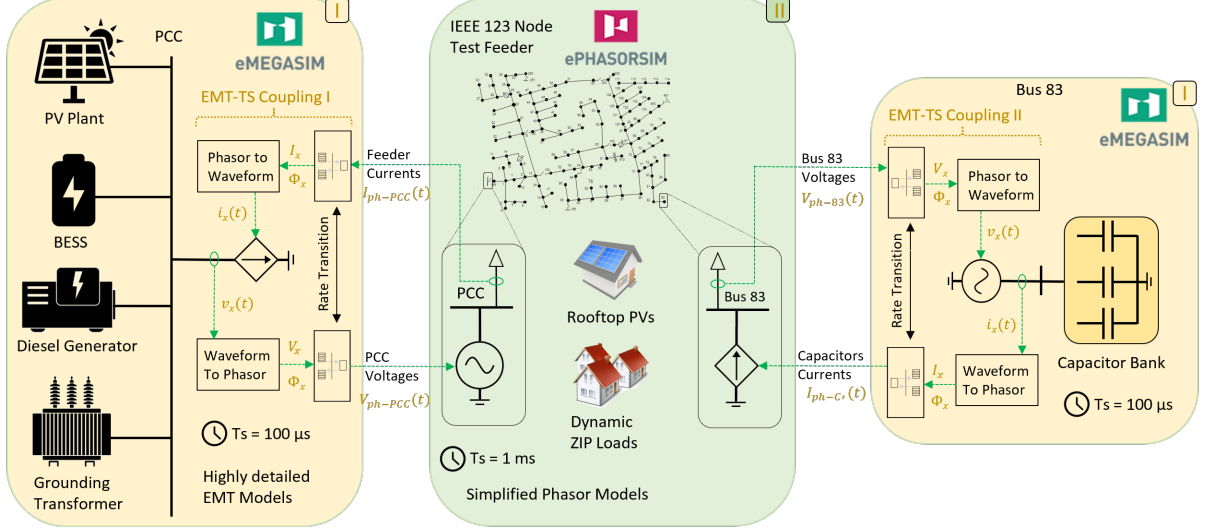


Figure 4.7: Proposed EMT-TS co-simulation testbed framework with capacitor bank moved to EMT domain.

The difference in the multi-EMT-TS testbed is that the transient performance of the capacitors' RMS current injection is simulated in the EMT domain, whereas if the capacitors were simulated in the phasor domain, the current transient would correspond to a step due to the new capacitive load added to bus 83. Figure 4.8 displays a comparison between the RMS currents measured for the EMT and EMT-TS testbeds for case (b), whereas Fig. 4.9 compares the feeder bus voltages during the switching event. Clearly, when simulating the capacitors in EMT domain, their impact on the feeder bus voltages can be better captured. This demonstrates the possibility of utilizing multi-EMT-TS couplings to move devices distributed across the feeder into the EMT domain as needed.

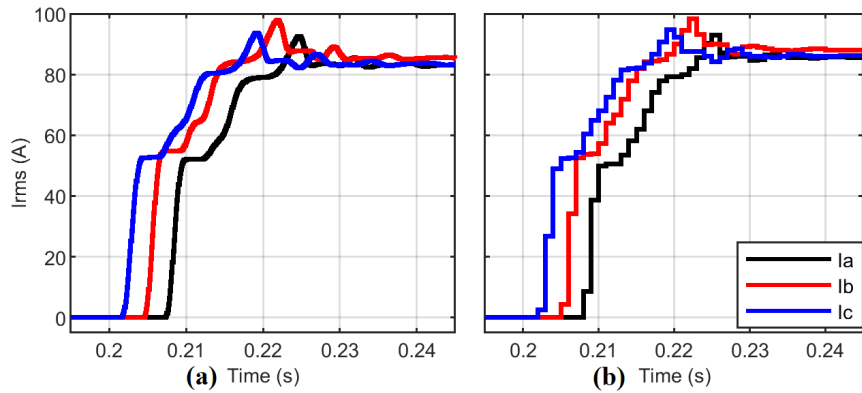


Figure 4.8: Current injection of the capacitor bank: (a) EMT testbed; (b) EMT-TS testbed with the shunt capacitors modeled in EMT domain.

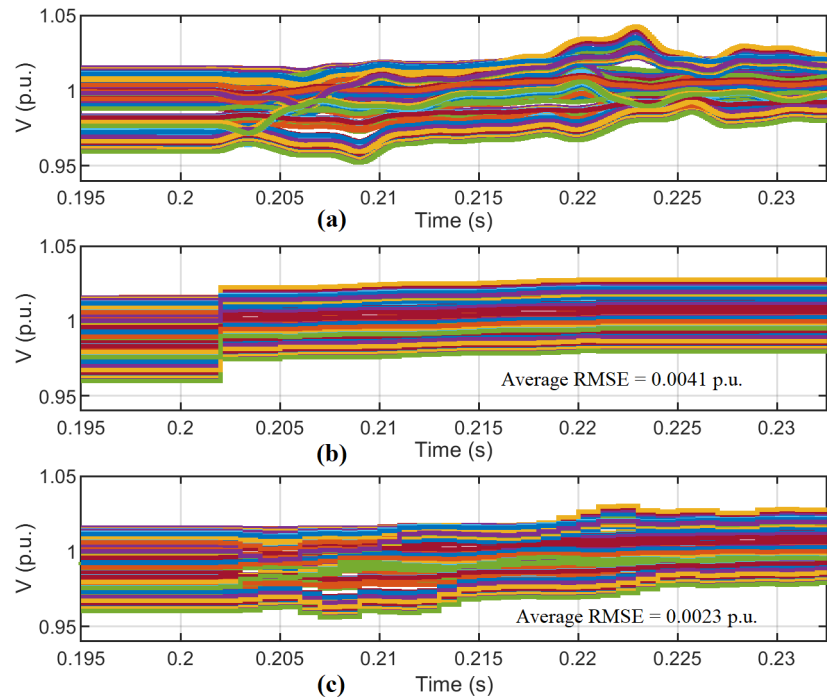


Figure 4.9: Feeder bus voltages during capacitor bank switching: (a) EMT model; (b) EMT-TS model with shunt capacitors modeled in phasor domain; (c) EMT-TS model with shunt capacitors modeled in EMT domain.

#### 4.4.4 Computational Cost Analysis

One of the main advantages of the co-simulation over the full EMT testbed is obviously its much reduced computational cost requirements. For this work, we utilized the OPAL-RT real-time simulator OP5700. Due to a limitation on the available SSN licenses for this work, the full EMT testbed (the benchmark) is simulated on one core, whereas the EMT-TS testbed is simulated on two cores, since the multi-timestep co-simulation environment requires at least one core for each independent subsystem. Since each testbed is simulated on a different number of cores, for a fair comparison, we set the EMT model to run four times slower than real-time in one core, and the EMT-TS testbed to run two times slower than real-time in two cores.

From the results, it is found that the EMT model required an average of  $295.4\text{ }\mu\text{s}$  to process each  $100\text{ }\mu\text{s}$  step, consuming approximately 73% of one core when running four times slower than real-time. Note that in this case, each  $100\text{ }\mu\text{s}$  of simulation time corresponded to  $400\text{ }\mu\text{s}$  in real life. On the other hand, the EMT-TS testbed required an average of  $21.2\text{ }\mu\text{s}$  per  $100\text{ }\mu\text{s}$  step, consuming around 11.4% of two cores when running two times slower than real-time (each  $100\text{ }\mu\text{s}$  of simulation time corresponded to  $200\text{ }\mu\text{s}$  in real life). This demonstrates that the full EMT model consumed about seven times more computational power than the co-simulation, even though the transient responses obtained from each testbed presented very similar results.

### 4.5 Conclusion

A novel real-time EMT-TS co-simulation testbed is presented, in which a grid-forming unit modeled in EMT domain operates as a slack bus in the phasor domain. The proposed testbed is validated against an equivalent EMT model developed as a benchmark. Results demonstrate that the proposed model can capture the transient response of BESS

units for typical load steps. Furthermore, we demonstrate that (i) the major impact of increasing the phasor domain timestep is the POW time-drift due to the propagation delay; (ii) using EMT-TS time interpolation coupling method will cause a smoothing effect when modeling fast changing waveforms, and (iii) the framework can be used for multi-EMT-TS coupling so that devices can be moved to the EMT domain such that their transient responses can be captured in higher detail. The proposed testbed has been used in day-long simulations of the restoration of a distribution feeder under high DER participation, in which an energy management system is utilized to control the DER devices. More details are presented in [62].

# Chapter 5

## Optimal Control of a Hybrid PV Plant

Recent incentives to expand the generation from RES have significantly boosted the amount of IBRs integrated into the grid. Consequently, as conventional synchronous machines are substituted by IBRs, the grid's inertia will be drastically reduced in the upcoming years. In [63], Yuan et al. estimated a reduction of 1% in the system inertia for every 1% increase in the PV penetration for the WECC system. Furthermore, lowering the inertia increases the frequency nadirs during contingencies, which can trigger under frequency load shedding events, or even cause a cascaded tripping of units.

To counter the aforementioned issues, new grid standards have raised their demands on GSFs expected from IBRs, such as power curtailment, stronger disturbance ride-through characteristics, and response to high ROCOF events [11], [12].

Chapter 3 introduced a PV power curtailment algorithm that can provide not only accurate power reserves, but also a fast dispatch that allows FFR services that can assist the grid in maintaining higher frequency nadirs during contingencies. However, even while maintaining headroom for frequency support, PVs are still susceptible to fast clouding events, during which either the power setpoint tracking or the power reserves must yield. As a result, despite including advanced GSFs, PV plants are still not able

to provide robust power reserves, and may consequently fail to follow AGC commands if under severe irradiance intermittency.

In [64], Chang *et al.* propose a coordination among multiple PV plants located in different geographic locations, so that if a shading event is imminent, power reserves are preemptively built up in other plants to help minimize the transient. Nevertheless, the approach is complicated, requiring coordination and communication amongst many PV plants, and by changing the PV injection in different regions, the system may experience volt-var control issues due to PV injection variation. A more tangible approach is to integrate a grid-following battery energy storage system (BESS) that can help the PV plant to follow power setpoints and/or maintain headrooms at all times. Moreover, the BESS can even be used to blackstart the PV plant [65].

There are several methods in the literature that propose the coordination of BESS to address the intermittency from RES. In [66], Teleke et al. proposed the usage of SOC feedback strategy when integrating the BESS into a windfarm, whereas in [67], Daud et al. apply the same strategy to a PV plant without the power curtailment functionality. In [68], the authors improved the performance by substituting the SOC feedback strategy by optimal control techniques. The advantage of optimal control such as model predictive control (MPC) is that it can consider future changes in the control objective, handle inputs and outputs constraints when solving for the optimal performance, and it is robust to modeling errors due to its inherent feedback control characteristic.

In [69], Nair et al. utilize an MPC to regulate PV and BESS in an energy scheduling problem; however, the method operates in steps of 5 minutes, hence ignoring the intra-minute power management that must be maintained for dealing with PV fast intermittency. In [70], Lei et al. present the coordination of PV and BESS via optimal control in a smaller time scale, but the work does not include power reserves.

In addition, most methods in the literature utilize simplified models for either the

BESS, PV, or the battery, which can oversimplify their dynamic performance. BESS and PV intra-minute power coordination with detailed models is presented by Chen et al. in [71]; however, it does not account for PV curtailment or power reserves, and it utilizes a rule-based approach instead of optimal control. An optimal control for intra-minute PV and BESS power management that includes power reserves and accurate EMT models is a topic still missing in existing literature.

Therefore, this Chapter proposes an optimal control with an adaptive MPC for operating a hybrid PV plant while considering its power reserves to provide regulation as well as FFR services. The PV plant is equipped with the advanced power curtailment algorithm recently introduced in [60]. An accurate lithium-ion battery model that has been experimentally validated in the literature is utilized for a more realistic approach, and an extended kalman filter (EKF) is designed for estimating the battery SOC. Detailed EMT models for both the PV plant and the grid-following BESS unit are implemented in a real-time simulator from OPAL-RT. Day-long simulations with high resolution irradiance and temperature data collected by our industry partner Strata Solar are executed to analyze the capability of the hybrid PV plant to maintain power reserves while following a regulation D signal from PJM (RTO).

The main contributions of the work to the literature are summarized as:

- Propose an optimal control strategy for operating a hybrid PV plant that can maintain robust power reserves for regulation services and/or FFR for reducing the grid frequency nadir during events of high ROCOF. The PV systems utilize the novel power curtailment algorithm from [60].
- Propose a state-space model of a hybrid PV plant model composed by an utility-scale PV system, a grid-following BESS unit, and an accurate second-order lithium-ion battery model that has been experimentally validated in the literature.

- Validate the optimal control strategy with detailed EMT models and realistic data sets, in day-long, real-time simulations.

## 5.1 Methodology

### 5.1.1 PV Plant Model

The circuit and control structure of a single-stage, grid-scale PV system was presented in Chapter 2, whereas the PV array equations were discussed in detail in Chapter 3; therefore, only a brief summary of the PV modeling is given in this chapter. Equation (5.1) represents the dynamics of a PV array, in which the five parameters of the model are the ideality factor ( $a$ ), the series resistance ( $R_s$ ), the shunt resistance ( $R_{sh}$ ), the photocurrent ( $I_{ph}$ ), and the diode saturation current ( $I_s$ ).

$$I_{pv} = I_{ph} - I_s \left( e^{\frac{V_{pv} + I_{pv} R_s}{a}} - 1 \right) - \left( \frac{V_{pv} + I_{pv} R_s}{R_{sh}} \right) \quad (5.1)$$

The five main PV parameters are obtained in real-time with the nonlinear least squares LM technique described in the previous chapter. Once the parameters are estimated, the voltage, current, and power at the MPP can be obtained as follows.

$$V_{mp} = \left( 1 + \frac{R_s}{R_{sh}} \right) a(w - 1) - R_s I_{ph} \left( 1 - \frac{1}{w} \right) \quad (5.2)$$

$$I_{mp} = I_{ph} \left( 1 - \frac{1}{w} \right) - \frac{a(w - 1)}{R_{sh}} \quad (5.3)$$

$$P_{mp} = V_{mp} I_{mp} \quad (5.4)$$

$$w = W \left\{ I_{ph} \frac{e}{I_s} \right\} \quad (5.5)$$

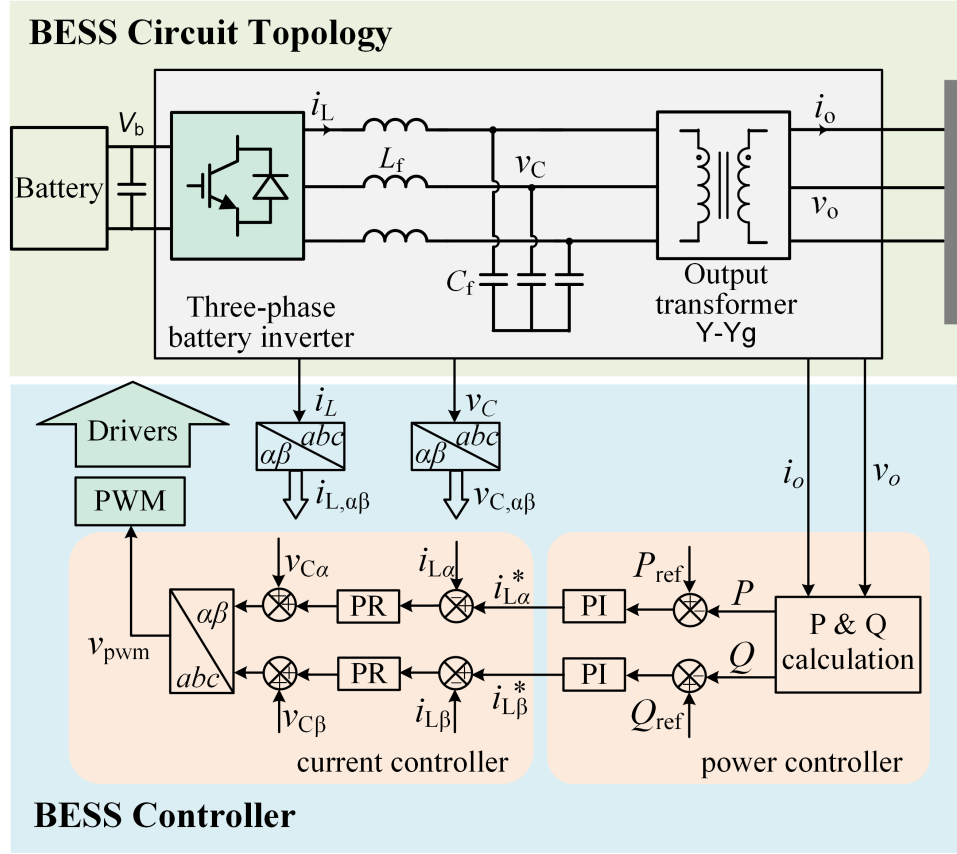


Figure 5.1: BESS circuit and control system diagram.

in which  $w$ , given by (5.5), is calculated with the Lambert  $W$  function. For a further discussion about the PV modeling and dynamics, please refer to Chapter 3.

### 5.1.2 Grid-Following BESS Model

The BESS unit, displayed in Fig. 5.1, consists of (i) a lithium-ion battery, (ii) a three-phase inverter operating in grid-following mode, (iii) an LC output filter, and (iv) an output Y-Yg transformer. Note that an LCL filter is not necessary at the inverters' output because the transformer's inductance is already used as an output inductance to form an LCL filter out of the LC filter. Figure 5.1 displays the BESS circuit and control system diagram.

In this work, the control system is developed in the  $\alpha\beta$  stationary reference frame (SRF), which requires one pair of PI controllers for power setpoint regulation, and one pair of proportional-resonant (PR) controllers for current regulation in the AC domain. The PR controllers transfer function is given by:

$$G_c = K_p + \frac{2K_r\omega_c s}{s^2 + 2\omega_c s + 4\omega_0^2} \quad (5.6)$$

where  $K_r$  is the resonant gain at  $2\omega$ ,  $\omega_c$  is the cut-off frequency, and  $\omega_0$  is the grid's nominal frequency [72].

The modulation signal ( $v_{\text{pwm}}$ ) is generated by adding the output of the PR controllers with a feedforward signal of the output capacitor voltage. More details on the SRF control with an Y-Yg output transformer is discussed in [59]. The inverter is built with an averaged model of a two-level VSC developed in [28]. Efficiency factors ( $\eta_{\text{charge}}$ ,  $\eta_{\text{discharge}}$ ) are used to represent the battery charging and discharging modes, respectively. It is assumed that the BESS efficiency factors for charging and discharging modes are constant.

### 5.1.3 Lithium-Ion Battery Model

Figure 5.2 displays a second-order dynamic model of a lithium-ion battery that has been developed based on the proposed method from [73]. The model is built with a combination of current and voltage sources that are used to recreate a realistic behavior of a lithium-ion battery as its output current is changed.

The battery SOC<sup>1</sup> is represented as the voltage ( $V_{\text{SOC}}$ ) across a capacitor  $C_c$ , with a capacitance that corresponds to the battery total capacity. The battery SOC is in function of the battery output current ( $I_b$ ) as follows:

---

<sup>1</sup>The variables  $V_{\text{SOC}}$  and  $SOC$  are used interchangeably throughout the text. Both refer to the battery state-of-charge.

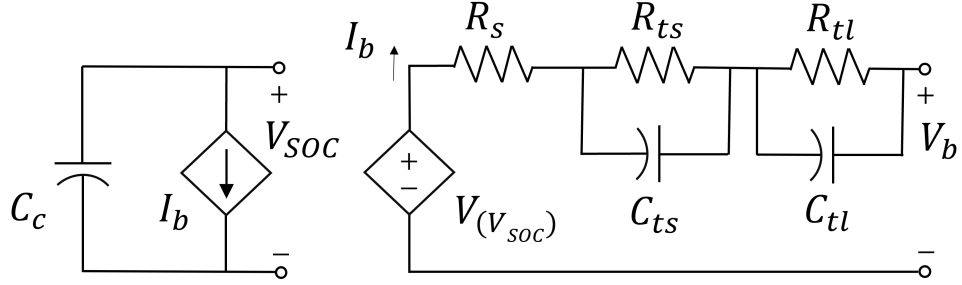


Figure 5.2: Second-order equivalent lithium-ion battery model.

$$SOC(t) = SOC_0 - \int_0^t \frac{I_b}{C^*} dt \quad (5.7)$$

where  $C^*$  is the actual battery capacity, which corresponds to the original capacity  $C_c$  multiplied by an aging factor  $K_{age}$  that represents the number of cycles. In this work, for simplicity, the aging factor is maintained as one, hence  $C^* = C_c$ .

The model contains two RC parallel branches ( $R_{ts}$ ,  $C_{ts}$ ) and ( $R_{tl}$ ,  $C_{tl}$ ) to represent the short-term and long-term voltage drops due to current step responses, respectively. Furthermore, a series resistor  $R_s$  is modeled to represent the instantaneous voltage drop due to a current step response. The dynamic response of the battery circuit internal voltages ( $V_{Cts}$ ,  $V_{Ctl}$ ) are given as follows.

$$\frac{dV_{Cts}}{dt} = \frac{I_b}{C_{ts}} - \frac{V_{Cts}}{R_{ts}C_{ts}} \quad (5.8)$$

$$\frac{dV_{Ctl}}{dt} = \frac{I_b}{C_{tl}} - \frac{V_{Ctl}}{R_{tl}C_{tl}} \quad (5.9)$$

The battery cell open-circuit voltage is a function of the instantaneous SOC value ( $V_{soc}$ ). Experiments can be carried to obtain the relation between the battery internal voltage and its SOC. In [73], the relation is accurately obtained via curve-fitting, and a seventh-order polynomial is built as follows:

$$V_{oc}(V_{SOC}) = a_1 V_{SOC}^7 + a_2 V_{SOC}^6 + a_3 V_{SOC}^5 + a_4 V_{SOC}^4 + \\ a_5 V_{SOC}^3 + a_6 V_{SOC}^2 + a_7 V_{SOC} + a_8 \quad (5.10)$$

Therefore, the battery output voltage ( $V_b$ ) is defined by (5.11).

$$V_b = V_{oc}(V_{SOC}) - V_{Cts} - V_{Ctl} - R_s I_b \quad (5.11)$$

The state-space (SS) representation of the battery open-circuit voltage can be obtained at any operating point by linearizing (5.10) at a given equilibrium point with a first-order Taylor series approximation:

$$V_{oc}(V_{SOC}) = V_{oc}(V_{SOC})\Big|_{V_{SOC}=V_{SOC_0}} + (V_{SOC} - V_{SOC_0}) \left[ \frac{\partial V_{oc}(V_{SOC})}{\partial V_{SOC}} \right] \Big|_{V_{SOC}=V_{SOC_0}} \quad (5.12)$$

where

$$\left[ \frac{\partial V_{oc}(V_{SOC})}{\partial V_{SOC}} \right] \Big|_{V_{SOC}=V_{SOC_0}} = 7a_1 V_{SOC_0}^6 + 6a_2 V_{SOC_0}^5 + 5a_3 V_{SOC_0}^4 + 4a_4 V_{SOC_0}^3 + \\ 3a_5 V_{SOC_0}^2 + 2a_6 V_{SOC_0} + a_7 V_{SOC_0} \quad (5.13)$$

Therefore, the linear model of the battery voltage around a given equilibrium point ( $V_{SOC_0}$ ) can be found with (5.14).

$$\Delta V_b = V_{oc}(V_{SOC_0}) + (\Delta V_{SOC} - V_{SOC_0}) \left[ \frac{\partial V_{oc}(V_{SOC_0})}{\partial V_{SOC}} \right] - \Delta V_{Cts} - \Delta V_{Ctl} - R_s \Delta I_b \quad (5.14)$$

To verify the accuracy of (5.11) to represent the output voltage of the battery dynamic model built in Simulink, a set of simulations are carried in which the battery model is discharged for one hour at 0.8 nominal current, causing its SOC to deplete from 100 to 20%. Figures (5.3a)-(5.3c) display the simulation results, including both the linearized battery voltage  $V_b$  from a SS representation and the actual voltage measured in the dynamic battery model. Clearly, the equation can depict the battery dynamics very well when the battery SOC is close to its equilibrium point utilized for the linearization. However, because of the nonlinearities of the battery model, significant errors emerge as the SOC deviates from the equilibrium point. To maintain modeling accuracy for a wide range of SOC values, subsequent linearizations must be carried in real-time. Figure 5.3d demonstrates a case in which the system is linearized every 100 seconds.

From the results, it can be seen that as long as the battery model is regularly linearized around its new operating point, it can be used as an accurate representation of the battery output voltage.

It is important to mention that the RC parameters of the second-order lithium-ion battery model from [73] are approximately constant over 20% to 100% SOC, but they change exponentially between 0% to 20% SOC. Consequently, the modeling approach presented here is only valid if the SOC is maintained above 20% at all times. Moreover, a self-discharging resistor could be added in parallel to  $C_c$  in Fig. 5.2 to represent the battery self-discharge of 2-10% per month, but this can be neglected for systems that are cycled often and/or do not leave the battery stored for a long time. Furthermore, as pointed in [73], in reality, all parameters from the second-order model are multivariable

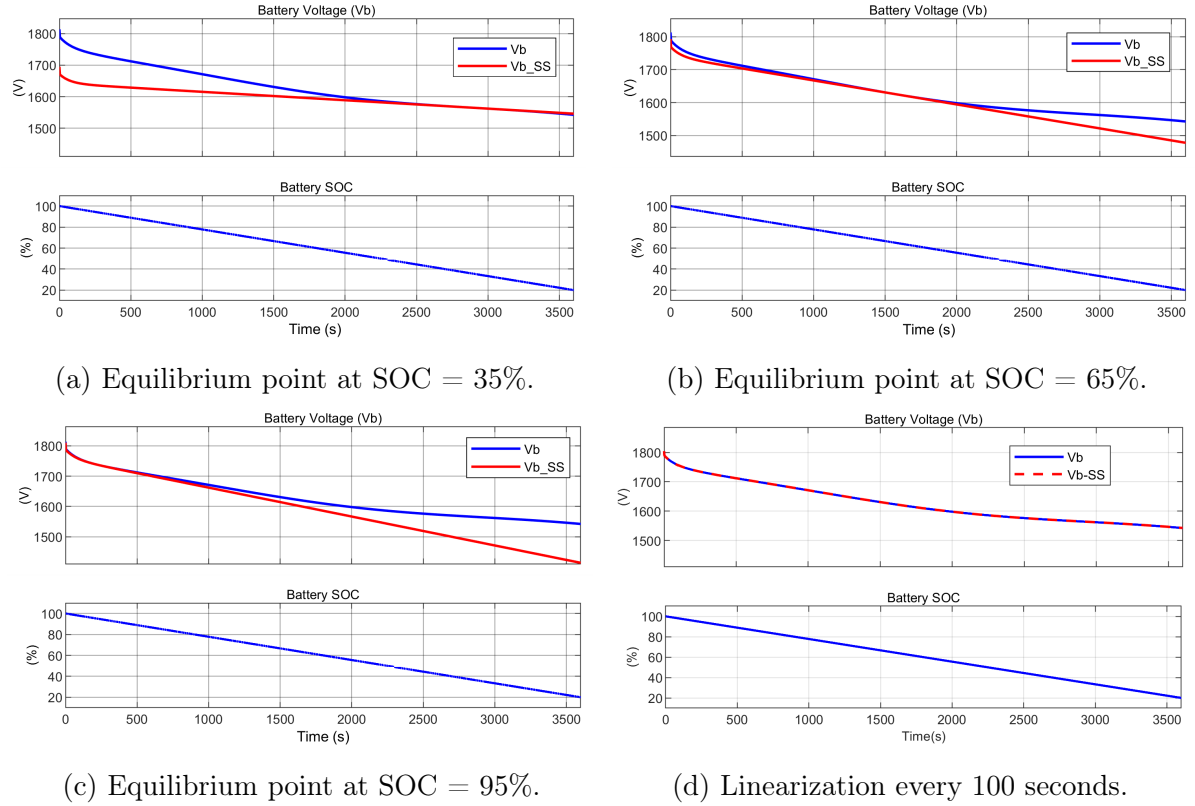


Figure 5.3: Modeling accuracy of the battery output voltage for linearizations at different equilibrium points.

functions of SOC, current, temperature, and number of cycles. Nevertheless, the model can still present satisfactory performance for most application if a certain error tolerance is acceptable. Because the main focus of this work is not on obtaining an extremely accurate battery model, it is assumed the parameters are constant within the 20-100% SOC range.

#### 5.1.4 Hybrid PV Plant State-Space

This section describes the SS modeling of the hybrid PV plant for implementation in a model predictive controller (MPC) is presented. The SS is designed with five state variables: the battery SOC ( $x_1$ ), the battery short-term internal voltage drop  $V_{\text{Cts}}$  ( $x_2$ ), the battery long-term internal voltage drop  $V_{\text{Ctl}}$  ( $x_3$ ), the battery current  $I_b$  ( $x_4$ ), and the PV dc output power  $P_{\text{pv}}$  ( $x_5$ ). It is worth mentioning the battery current and the PV output power are set as state variables so constraints can be established for them in the MPC solver, which is required to ensure their physical limitations are respected during operation.

The hybrid PV plant has two main control inputs: change in battery output current ( $u_1$ ) and change in PV dc output power ( $u_2$ ). The control inputs are set as derivatives instead of the actual battery current and PV output power so that state variables can be assigned to the actual battery current and PV output power. Furthermore, the system also contains one input disturbance, corresponding to the maximum available PV dc power,  $P_{\text{mp}}$  ( $u_3$ ). The disturbance is a measurable signal that comes from the MPPE algorithm presented in Chapter 4. It is used to provide the MPC with constraints for the maximum PV power available. More about this is discussed in the upcoming section, regarding the MPC design. Inputs  $u_1$  and  $u_2$  are constrained within the ramp-up and ramp-down rate limits of the BESS and PV system. It is assumed that the same ramping

limit is implemented for both upwards and downwards power setpoint changes.

$$u_1 = \frac{dI_b}{dt}, \quad -I_{b,\text{rate}} \leq u_1 \leq I_{b,\text{rate}} \quad (5.15)$$

$$u_2 = \frac{dP_{\text{pv}}}{dt}, \quad -P_{\text{pv},\text{rate}} \leq u_2 \leq P_{\text{pv},\text{rate}} \quad (5.16)$$

$$u_3 = P_{\text{mp}}, \quad \text{from (5.4)} \quad (5.17)$$

The model is designed with five output variables: the hybrid plant output power ( $y_1$ ), the battery current ( $y_2$ ), the battery SOC ( $y_3$ ), the plant fast dispatch power reserves ( $y_4$ ), and the PV output power ( $y_5$ ). The output variables  $y_2$ ,  $y_3$ , and  $y_5$ , corresponding to  $I_b$ ,  $SOC$ , and  $P_{\text{pv}}$ , are defined to allow the implementation of constraints to the respective state variables when designing the MPC. The hybrid PV plant output power is given by (5.18), whereas the plant fast dispatch power reserves are given by (5.19).

$$y_1 = P_{\text{out}} = \eta_{\text{bess}} \left[ V_{oc}(x_1) - V_{ts} - V_{tl} - R_s I_b \right] I_b + \eta_{\text{pv}} P_{\text{pv}} \quad (5.18)$$

$$y_4 = P_{\text{res}} = \eta_{\text{bess}} \left[ P_{\text{bess}}^N - (V_{oc}(x_1) - V_{ts} - V_{tl} - R_s I_b) I_b \right] + \eta_{\text{pv}} (P_{\text{mp}} - P_{\text{pv}}) \quad (5.19)$$

The PV and BESS unit efficiencies ( $\eta_{\text{pv}}$ ,  $\eta_{\text{bess}}$ ) include the inverter and output transformer losses, and the BESS efficiency factor is based on the charging or discharging operation of the battery by (5.20).

$$\eta_{\text{bess}} = \begin{cases} \eta_{\text{discharge}} & \text{if } I_b \geq 0 \\ \eta_{\text{charge}} & \text{if } I_b < 0 \end{cases} \quad (5.20)$$

Thus, the SS of the system in the traditional form is defined as follows.

$$\begin{aligned} \dot{\mathbf{x}} &= A\mathbf{x} + B\mathbf{u} \\ \mathbf{y} &= C\mathbf{x} + D\mathbf{u} \end{aligned} \quad (5.21)$$

$$\begin{bmatrix} \dot{x}_1 \\ \dot{x}_2 \\ \dot{x}_3 \\ \dot{x}_4 \\ \dot{x}_5 \end{bmatrix} = \begin{bmatrix} 0 & 0 & 0 & -\frac{1}{C_c} & 0 \\ 0 & \frac{-1}{R_{ts}C_{ts}} & 0 & \frac{1}{C_{ts}} & 0 \\ 0 & 0 & \frac{-1}{R_{tl}C_{tl}} & \frac{1}{C_{tl}} & 0 \\ 0 & 0 & 0 & 0 & 0 \\ 0 & 0 & 0 & 0 & 0 \end{bmatrix} \begin{bmatrix} x_1 \\ x_2 \\ x_3 \\ x_4 \\ x_5 \end{bmatrix} + \begin{bmatrix} 0 & 0 & 0 \\ 0 & 0 & 0 \\ 0 & 0 & 0 \\ 1 & 0 & 0 \\ 0 & 1 & 0 \end{bmatrix} \begin{bmatrix} u_1 \\ u_2 \\ u_3 \end{bmatrix} \quad (5.22)$$

$$\begin{bmatrix} y_1 \\ y_2 \\ y_3 \\ y_4 \\ y_5 \end{bmatrix} = \begin{bmatrix} 0 & 0 & 0 & \eta_{\text{bess}} [V_{\text{oc}}(x_1) - x_2 - x_3 - R_s x_4] & \eta_{\text{pv}} \\ 0 & 0 & 0 & 1 & 0 \\ 1 & 0 & 0 & 0 & 0 \\ 0 & 0 & 0 & -\eta_{\text{bess}} [V_{\text{oc}}(x_1) - x_2 - x_3 - R_s x_4] & -\eta_{\text{pv}} \\ 0 & 0 & 0 & 0 & 1 \end{bmatrix} \begin{bmatrix} x_1 \\ x_2 \\ x_3 \\ x_4 \\ x_5 \end{bmatrix} + \quad (5.23)$$

$$\begin{bmatrix} 0 & 0 & 0 \\ 0 & 0 & 0 \\ 0 & 0 & 0 \\ 0 & 0 & \eta_{\text{pv}} \\ 0 & 0 & 0 \end{bmatrix} \begin{bmatrix} u_1 \\ u_2 \\ u_3 \end{bmatrix} + \begin{bmatrix} 0 \\ 0 \\ 0 \\ \eta_{\text{bess}} P_{\text{bess}}^N \\ 0 \end{bmatrix}$$

$V_{\text{oc}}(x_1)$  is defined by (5.10). Note the controllability matrix of the proposed SS model, given by  $R = [B \ AB \ A^2B \ \dots \ A^{n-1}B]$ , presents full rank, confirming that all states of the system are controllable.

### 5.1.5 Model Predictive Control Design

In this work, the optimal operation of the hybrid PV plant is achieved by the implementation of a MPC, which utilizes feedback control to solve for the optimal operation of the system while maintaining inputs and outputs within constraints that respect the physical limitations of the components. The objective of the optimal control problem is to find admissible control trajectories,  $z_k$ , that follow admissible output trajectories,  $y_j$ , that minimize the cost  $J(z_k)$ , given in (5.24).

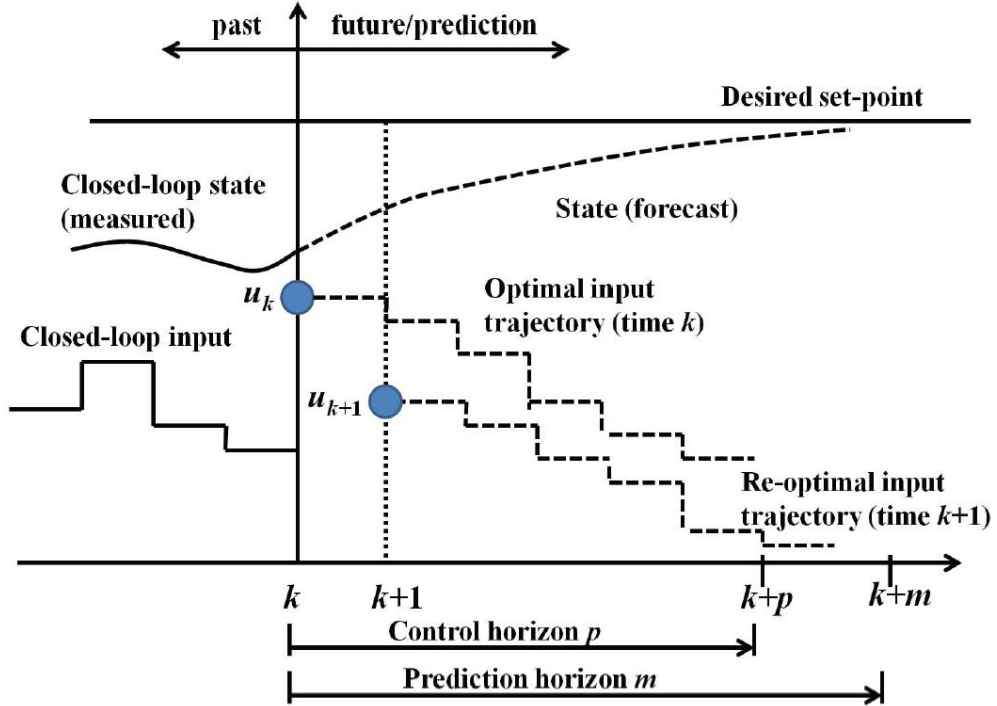


Figure 5.4: Illustration of MPC prediction and control horizons. From [4].

$$J(z_k) = J_y(z_k) + J_{\Delta u}(z_k) + J_\epsilon(z_k) \quad (5.24)$$

Figure 5.4 exemplifies the operation of a MPC. The prediction horizon represents how many steps ahead the controller considers for the optimization, whereas the control horizon corresponds to how many control steps are optimized within a given prediction horizon. If the control horizon is lesser than the prediction horizon, the control inputs is fixed at the last optimized value until the end of the prediction horizon.

In the cost function given by (5.24),  $J_y(z_k)$  corresponds to the tracking error cost;  $J_{\Delta u}(z_k)$ , defined in (5.27), is the cost associated with penalizing aggressive control moves, and  $J_\epsilon$  is a penalty factor associated with constraint violations. The constraint violation cost ensures the solver can maintain numerical stability during real-time operation by violating soft constraints if the solution becomes unfeasible. Therefore, to avoid numerical

instabilities caused by hard constraints, the battery current, battery SOC, and the fast dispatch power reserves are set with soft constraints. Nevertheless, they are not designed with the same level of constraint softness, since in our case it is important to maintain both the battery SOC and current values within their physical limits at all times. More details on the penalty factor for handling constraint violations are given in [74].

The tracking error cost is defined by (5.25),

$$J_y(z_k) = \sum_{j=1}^{n_y} \sum_{i=1}^p \left\{ \frac{w_j^y}{s_j^y} \left[ (y_j^*(k+i|k) - y_j(k+i|k)) \right] \right\}^2 \quad (5.25)$$

where  $w_j^y$  and  $s_j^y$  are the cost weights and scale factors for the  $j$ th plant output ( $y_j$ ), respectively,  $k$  is the current control interval,  $p$  is the size of the prediction horizon,  $n_y$  is the number of plant output variables, and  $z_k$  is the solution for the optimal control signals, given by (5.26).

$$z_k^T = [u(k)^T \ u(k+1|k)^T \ \dots \ u(k+p|k)^T] \quad (5.26)$$

The tracking cost weights must be tuned so the desired operation performance is achieved. For the hybrid PV plant, the main goal is to track an output power reference defined in (5.18), hence its weight is set with the highest value. Moreover, some of the weights will always be zero, such as the battery current weight ( $w_2^y$ ) and the PV output power weight ( $w_5^y$ ), because there is no specific goal for each of them individually. The actual objective is the overall output power of the system.

The SOC weight ( $w_3^y$ ) could be set as zero as well, because that will allow the MPC to optimize the operation without taking into account any given setpoint for the battery SOC. However, that approach has two drawbacks. First, by not having an SOC setpoint, the initial SOC value for each new operating cycle cannot be controlled, which can be a problem if a new cycle starts with the battery fully discharged. Second, during moments

of high forecast error, if the battery is at low SOC levels, it may not be available to help boost the power output during PV drops, thus it would be preferred to maintain the SOC at higher levels when possible, considering that downward regulation can always be easily achieved by curtailing the PV.

Consequently, the SOC weight can be set to a very small value (in comparison to the power output weight) with a high setpoint value (e.g., 90%). With those settings, the MPC will boost the battery SOC to higher levels when possible, but it will significantly prioritize the power setpoint tracking during operation. It is also worth mentioning that leaving a lithium-ion battery to linger at a fully charged state will accelerate their aging process [75]; therefore, it may be preferred to not set the BESS SOC setpoint to 100%.

The aggressive control moves penalization cost is defined as

$$J_{\Delta u}(z_k) = \sum_{j=1}^{n_u} \sum_{i=0}^{p-1} \left\{ \frac{w_j^{\Delta u}}{s_j^u} \left[ (u_j(k+i|k) - u_j(k+i-1|k)) \right]^2 \right\} \quad (5.27)$$

where  $w_j^{\Delta u}$  and  $s_j^u$  are the cost weights and scale factors for the  $j$ th control input ( $u_j$ ), respectively, and  $n_u$  is the number of plant control signals. Note that in this case, the cost weights are maintained the same within a given prediction horizon. The penalization of aggressive control moves incentivizes the controller to maintain a smooth operation when trying to optimize the tracking error cost, and helps maintaining good numerical conditioning.

Due to the nonlinear characteristics of the hybrid plant SS model, such as the battery open-circuit voltage, a linear MPC design is not appropriate for this application. That is because a traditional MPC method is modeled with a linearized version of the plant around an equilibrium point. Yet, as displayed in Figs. (5.3a)-(5.3c), if the battery deviates from the linearization point, significant errors in its output voltage (and consequently, in its expected output power) will occur. Thus, a MPC implementation

that can handle nonlinearities must be used. The MPC Toolbox from [74] is compatible with the eMEGASIM environment utilized for real-time simulations and provides multiple options for the implementation of MPCs that can handle nonlinear models, such as Adaptive MPC, Gain-Scheduled MPC, and Nonlinear MPC. These different methods can be summarized as follows:

- **Adaptive MPC:** the model structure is fixed, but the model parameters can evolve with time. At each control interval, the MPC updates the plant model based on the current nominal conditions. Hence, at every new prediction horizon and control step calculation, the controller linearizes the plant for that corresponding step. The main advantage is that the controller still solves a linear quadratic programming problem with linear inequality constraints, which can significantly reduce the computational burden.
- **Gain-Scheduled MPC:** built by combining multiple traditional MPCs, each designed for a specific operating region of the nonlinear plant. It is similar to an Adaptive MPC in the sense that it also utilizes multiple linearizations of the plant to account for different operating regions. However, the main differences are (i) the MPC designed must be performed a prior, requiring more online storage, and (ii) the number of MPC designs required for proper operation may increase significantly depending on the plant nonlinear characteristics.
- **Nonlinear MPC:** the most powerful method. Its prediction horizon can include time-varying parameters, it can include nonlinear constraints, and the cost function to be minimized can be a nonquadratic function of the decision variables. Its main drawback is obviously the computational effort associated with its constrained nonlinear optimization problem that must be solved in real-time.

During the development of this work, both the adaptive MPC and the nonlinear MPC were tested. However, it was soon observed that the computational burden from the nonlinear MPC would significantly limit the prediction horizon's length, forcing it to be up to nine times smaller than the prediction horizon of the adaptive MPC for a similar computational processing time. Because a significantly smaller prediction horizon would not be able to manage the BESS SOC due to its slow dynamics, the nonlinear MPC approach was discarded.

Figure 5.5 displays the proposed control strategy utilizing an Adaptive MPC. The Adaptive MPC sends the power setpoints to the plant comprised of the PV and BESS units. Sensors measure the PV output power as well as the battery voltage and current, which are inserted in an EKF that estimates the system states. PV forecasts and information about the instantaneous maximum available PV power (from the algorithm presented in [60]) are also inputs of the adaptive MPC. The MPC receives setpoints for the output power, minimum power reserves, and battery SOC. In the figure, it is assumed that the setpoints are generated by an external energy management system (EMS).

Three main parameters must be defined when designing the MPC: timestep ( $T_{\text{mpc}}$ ), prediction horizon, and the control horizon. The timestep should be small enough for the method to respond to external disturbances (irradiance changes) and properly respond to the system's dynamics, but it cannot be too small or the computational burden will be too high for real-time operation. Higher prediction and control horizons will also increase the computational effort required, and will not necessarily improve the system performance. For example, if the prediction horizon is too long, part of its results may be useless if unexpected disturbances occur.

After several tests, the timestep was selected as three seconds and the prediction horizon was selected as 400 steps (20 minutes), which is long enough to include a good portion of the battery charging/discharging cycle. The timestep could be reduced to 2 or

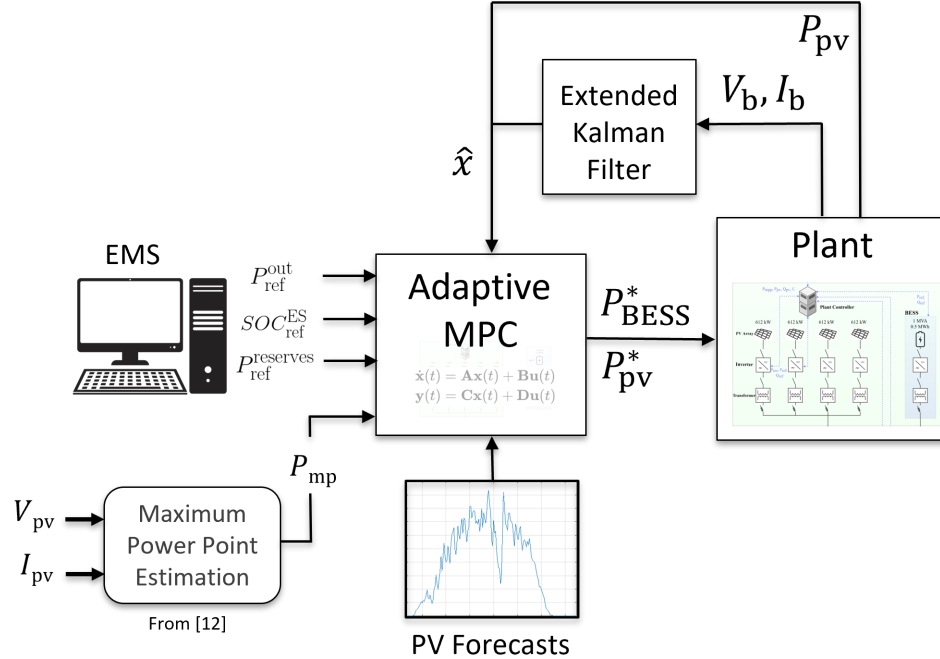


Figure 5.5: Proposed control strategy.

even 1 second(s) if real-time operation can be maintained, but it should not be increased further, as this would cause the response to irradiance transients will deteriorate. The control horizon has also been heuristically designed, with a proposed value of 20 steps, which was set based on the PV forecasting.

One major factor that can impact the performance of the MPC optimization is its knowledge about the PV power availability in the future. As previously mentioned, the PV power output ( $x_5$ ) is set as a system output ( $y_5$ ) so that it can be subjected to soft constraints. By utilizing information about the available maximum PV power from the unified PV power curtailment algorithm introduced in Chapter 4, the  $P_{mp}$  can be inserted into the adaptive MPC not only as a disturbance ( $u_3$ ), but also as an upper constraint to  $y_5$ .

By actuating as an upper constraint being updated in real-time,  $P_{mp}$  forces the MPC to consider what is the actual available PV power when solving for the optimal control

commands  $u_1$  and  $u_2$ . Moreover, by applying the constraint to an output variable, the constraint can be established with a small degree of softness, hence avoiding numerical instabilities that could occur when a hard constraint is violated. Admittedly, the small degree of softness may cause the MPC controller to command a few extra kWs from the PV plant when the irradiance oscillates; however, those small errors are insignificant considering that (i) if the command is larger than the available power, the PV will output the maximum power available, and (ii) modeling errors will always occur in practice.

Moreover, there will be an issue if  $P_{mp}$  is utilized as a disturbance that updates the upper constraint of the PV power in real-time. At every MPC step, the controller will calculate an optimal control sequence (5.26) for the control horizon to optimize the cost (5.24) over a prediction horizon assuming that the PV output power upper constraint is fixed at the given measured disturbance. As a result, because the irradiance is constantly changing, both the optimized control and prediction horizons rendered by the MPC will be useless due to major estimation errors.

This problem is tackled by utilizing time-varying upper bounds that can be established with customized lengths, ranging from a few steps to the entire prediction horizon. Here, the time-varying upper bound is set as the length of the control horizon. That means the solver assumes the upper bound to be constant from between the end of the control horizon until the end of the prediction horizon (see Fig. 5.4). It is worth mentioning that the implementation of time-varying upper bounds capable of being updated in real-time is a feature that was only introduced into the MPC Toolbox on MATLAB R2020b version [76]. Furthermore, for the implementation in a real-time simulator for realistic day-long tests including detailed EMT models, the MATLAB R2020b version must also be compatible to the real-time simulator host (RT-LAB). RT-LAB only became compatible with MATLAB R2020b in its 2021.2 version, released on November 30, 2021. Consequently, the approach proposed here was not possible prior to that date, and

it can only be carried out in RT-LAB versions 2021.2 or above.

## Real-Time PV Forecast

Once the upper bound of the available PV output power is implemented with online time-varying capability, a realistic approach must be developed to represent how the future PV availability will be forecasted by the MPC. The more accurate the forecast, the closer the MPC performance will be to its optimal solution. In this work, we consider the employment of two forecast techniques: (i) an ultra-short-term forecast (also referred as “nowcasting”) of the available PV power with skycams (Fig. 5.6), and a 20 minutes ahead forecast of the average available PV power.

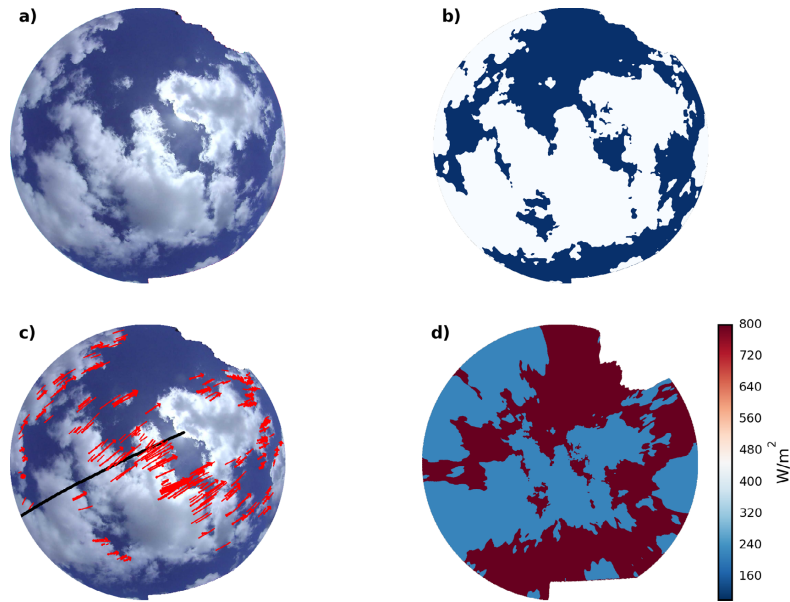


Figure 5.6: Basic steps in sky image processing: (a) raw masked image, (b) binary cloud detection, (c) cloud tracking with final cloud motion path, and (d) projected irradiance map. From [5].

As displayed in Fig. 5.6, the ultra-short-term forecasting method relies on the coordination of multiple sensors combined with statistical analysis to predict how the cloud movement will impact the overall available PV power in the next few minutes.

The approach to represent the performance of a 15 to 30-minutes ahead average PV power forecaster is straightforward. Based on the actual available PV power value, a forecast error is added to represent the typical forecaster accuracy, and the error magnitude is updated for every new estimation. On the other hand, more considerations need to be given to represent the performance of an ultra-short-term forecaster. Here, it is assumed that the PV plant runs the nowcasting algorithm proposed in [6], which has been experimentally validated with 70 inverters of the 48 MWdc plant displayed in Fig. 5.7 for a total of 171 days of operation, not including clear sky days to focus on the performance under days with high irradiance intermittency.

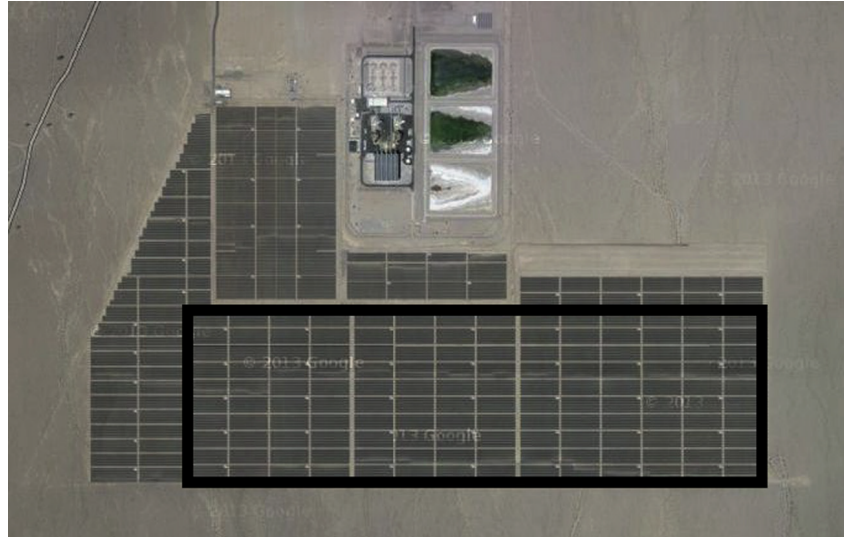


Figure 5.7: Google maps picture of the Sempra US Gas and Power CMS1 Solar Plant near Henderson, NV. From [6].

In its performance analysis, the method reported a relative root mean square error (rRMSE) of 3.2% for its 20-seconds ahead forecast, and an approximately linear error increase up to 8.2% at its 60-seconds ahead forecast. After the first minute, the error relation to the prediction length is no longer linear. In this work, we utilize ultra-short-term forecasting only for the first 60 seconds, which is also the length of the control horizon of the adaptive MPC. By utilizing the forecast for the entire duration of the

control horizon, the control trajectory can be optimized based on realistic upper bound constraints for what the maximum available PV power is. The rRMSE is defined by (5.28).

$$rRMSE = \frac{1}{P_{\text{real}}} \sqrt{\frac{1}{n} \sum_{i=1}^n [P_{\text{forecast}}(i) - P_{\text{real}}(i)]^2} \quad (5.28)$$

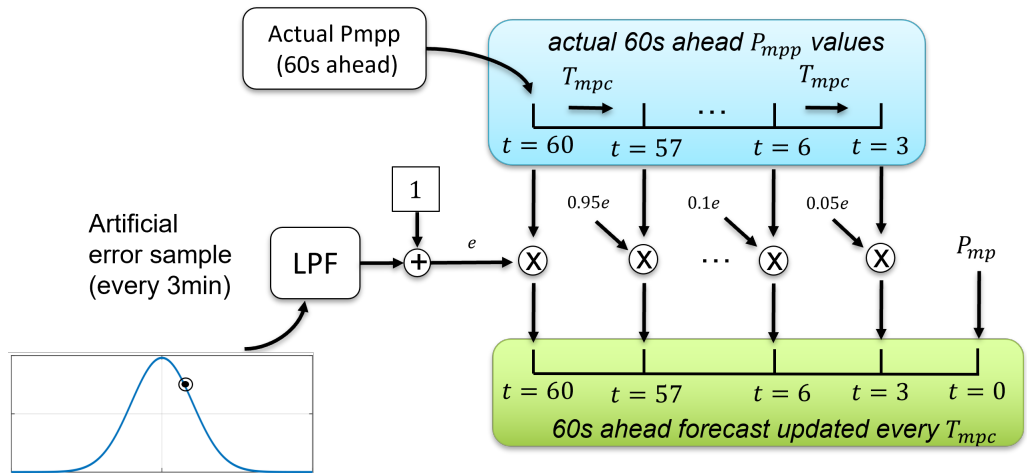


Figure 5.8: Illustration of how the nowcasting performance is replicated in real-time.

Figure 5.8 demonstrates how the performance of the ultra-short-term forecasting method is simulated for a system with an MPC step of 3 seconds and a control horizon of 60 seconds. First, a normal distribution is sampled every few minutes to generate an artificial error that will correspond to the overall forecaster performance. Next, the new error value is filtered by a low-pass filter (LPF) with a time constant of one minute. The filter ensures the estimations will not be instantaneously stepped up or down as new error values are sampled, providing a more realistic transition between different estimation errors. Then, the filtered error factor ( $e$ ) is applied to the actual  $P_{mp}$  values, which are constantly being stored and updated in an auxiliary vector. By reducing the error factor ( $e$ ) from its full value at the 60-seconds ahead forecast down to  $0.05e$  at the 3-seconds ahead forecast, the estimation accuracy is linearly improved as the prediction

length is reduced. Figure 5.9 shows an example of the performance at the 60-seconds ahead estimation.

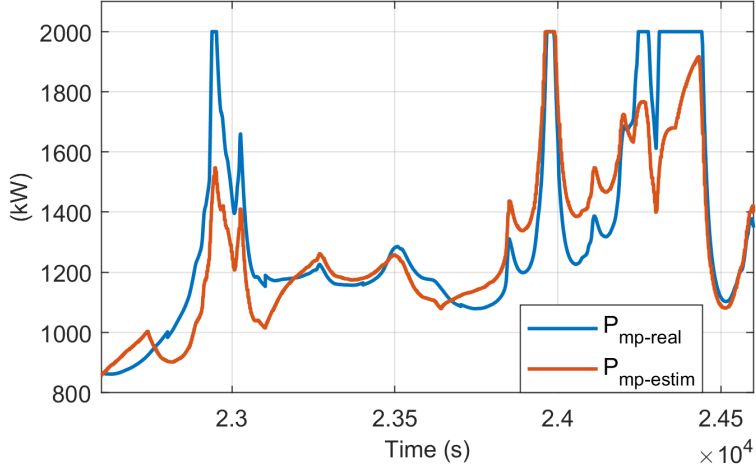


Figure 5.9: Example of nowcasting simulated error estimating 60-seconds ahead for a 2 MW plant.

Notice that the PV available power is saturated at the plant's rated power; therefore, during PV clipping events (when the available power is larger than the plant's ratings), the forecast error might reduce or even become insignificant depending on the degree of PV clipping.

### Extended Kalman Filter

In order to optimally control the system over a prediction horizon, the adaptive MPC requires knowledge about the current system states. Because the battery states cannot be directly measured, in this work, they are estimated with an EKF. The implemented EKF receives measurements of the battery voltage and current, and estimates the battery's internal states from (5.22). Hence, the states of interest for the estimation are the battery SOC and the internal voltage drops  $V_{ts}$  and  $V_{Ctl}$ . For a more realistic performance, Gaussian noises are added to the  $V_b$  and  $I_b$  measurements to match the signal-to-noise (SNR)

ratios expected from basic dc sensors. Figure 5.10 displays the EKF block diagram, where  $(w, Q)$  and  $(v, R)$  represent process and measurement noises, defined in (5.29)<sup>2</sup>. Note that because this work does not involve experimental tests, the process noise  $w_k$  is not considered.

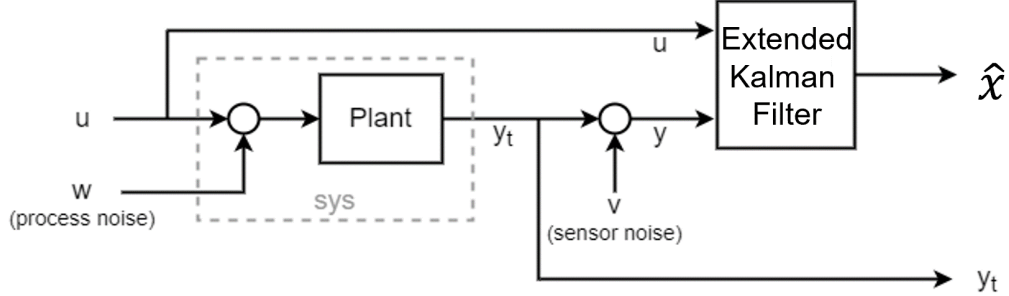


Figure 5.10: Extended Kalman Filter block diagram.

$$w_k \sim N(0, Q(t))$$

$$v_k \sim N(0, R_k) \quad (5.29)$$

The basis of the EKF strategy is to use information from available sensors combined with a mathematical model of the system to predict an optimal estimate for the system states. As shown in Fig. 5.10, the EKF required inputs include (i) measurements from available sensors ( $y$ ) and (ii) information about the inputs applied to the system ( $u$ ), whereas its outputs are the system estimated states ( $\hat{x}$ ). The main difference between the EKF when compared to the traditional KF is that in the EKF, the system is linearized at each timestep, and the resulting Jacobian matrices are used for the prediction and update of the states. The EKF algorithm can be summarized in the following main steps.

First, the system mathematical model and the system input information is used to estimate the next system states (5.30) and a corresponding error covariance  $P_k$ , which

---

<sup>2</sup> $Q$  and  $R$  are the covariance matrices of the process and measurement noises.

represent a measure of uncertainty related to the estimated state due to process noise and errors in the initial state estimate  $\hat{x}_{k-1}$ .

$$\hat{x}_k^- = A\hat{x}_{k-1} + Bu_k \quad (5.30)$$

$$\hat{P}_k^- = f_k P_{k-1} f_k^T + Q_k \quad (5.31)$$

$$f_k = \frac{\partial}{\partial x} (Ax_k + Bu_k) |_{\hat{x}_k^-} \quad (5.32)$$

Next, a Kalman gain ( $K_k$ ) is calculated (5.33), and a new state estimation  $\hat{x}_k$  is obtained by adding the measurements information ( $y_k$ ) to the previous estimated state ( $\hat{x}_k^-$ ) via the Kalman gain (5.33). The Kalman gain is also utilized to reduce the error covariance  $P_k^-$  (5.34), reducing the uncertainty associated with the new state estimation  $\hat{x}_k$ .

$$K_k = \frac{P_k^- C^T}{C P_k^- C^T + R_k} \quad (5.33)$$

$$\hat{x}_k = \hat{x}_k^- + K_k (y_k - C \hat{x}_k^-) \quad (5.34)$$

$$P_k = P_k^- - K_k C P_k^- \quad (5.35)$$

Afterwards, the new  $P_k$  and  $\hat{x}_k$  are used in 5.30-5.31, and the process repeats. It is worth mentioning that the Kalman gain correction term  $R_k$  is used to tune the weights of the system model and the measurements when predicting the new state  $\hat{x}_k^-$ . For instance, by reducing  $R_k$ , we increase the trust in the system measurements, increasing the impact

of  $y_k$  in (5.33).

## 5.2 Real-Time Simulation Results

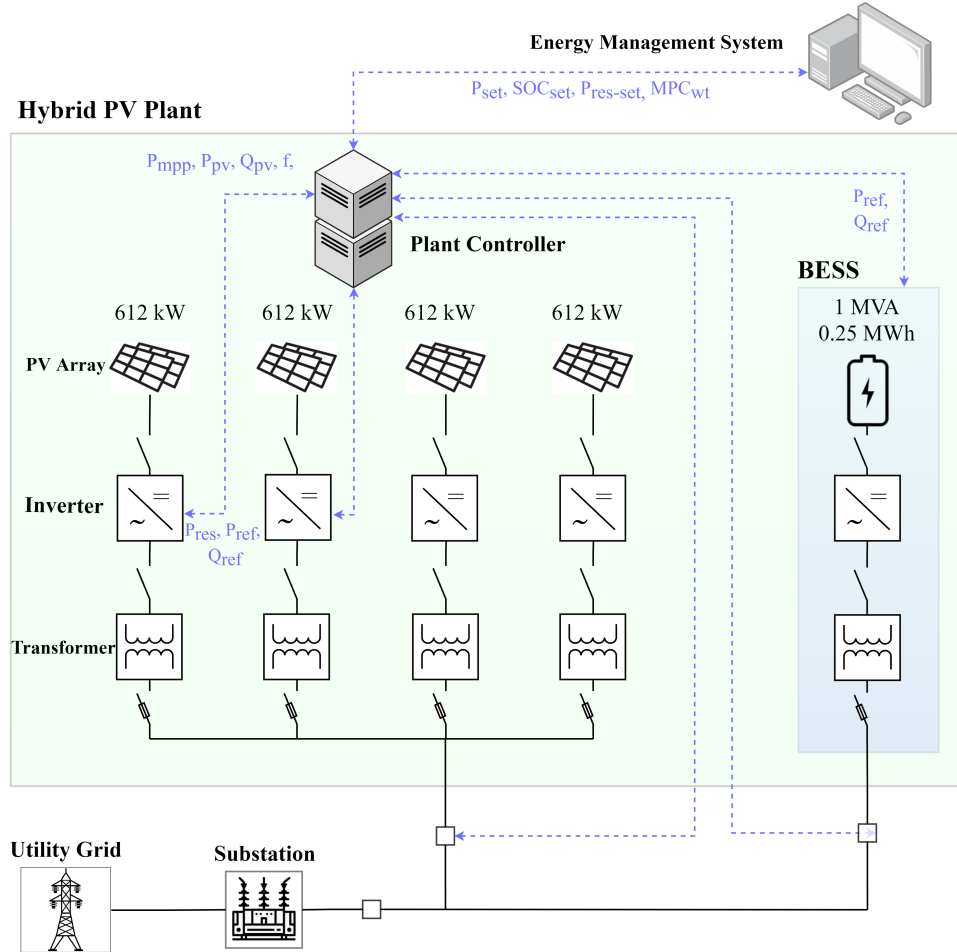


Figure 5.11: Configuration of a hybrid PV plant.

To validate the proposed algorithm, a testbed is set up in an OPAL-RT real-time simulation platform. Figure 5.11 displays the configuration of the hybrid PV plant developed in this work. The system consists of four equal 612 kWdc PV arrays, a plant controller, and a 1.2 MVA grid-following BESS equipped with a 1 MW/0.25 MWhdc lithium-ion battery unit that assists the system with the intra-minute power management.

For the battery model, we utilize the battery cell discussed in [77], which has a design suitable for high power applications. The battery rated capacity is 20 Ah, with a maximum discharge current of 100 A. In addition, it has a maximum voltage charge of 4.15 V, and a discharge of 3 V. For this application, the battery is designed with 441 cells in series, and 9 cells in parallel, such that the maximum discharge current is 800 A, at which rate the system would deplete in 12 minutes. Note that if the current is fixed, the battery output power is reduced as the voltage drops due to the discharge and the voltage drop inside the battery, hence the battery is more efficient at higher SOC values. For instance, at an SOC of 65%, with the battery operating at 626 A, the battery terminal voltage is approximately 1543 V, the dc output power is measured as 967 kW, and the ac output power after inverter and transformer losses is 934 kW. At a constant discharge of 650 A, the battery can supply a total of 0.256 MWhdc, whereas at a discharge of 250 A, it can supply 0.282 MWhdc. Noticeably, this is a small storage capability. This is because the focus here is not on optimizing the battery design, but rather on developing an optimal operation for an existing system with high power-to-storage ratio.

To avoid violating inverter limits and operating at very high current values, in this work the battery current is limited to 650 A when in discharging mode, and 550 A when in charging mode. This gives the BESS system a power regulation capability of around 1 MW on its AC side (after losses). Furthermore, it is assumed that the adaptive MPC is implemented in an external computer where the plant controller is located. The plant controller is responsible for communicating with the PV and BESS inverters and an external energy management system (EMS). Figures 5.12 and 5.13 display the data utilized. A comprehensive list of the simulation parameters designed for the work in this chapter is given in the appendix.

Note the irradiance and temperature measurements correspond to the incident irradiance on the PV panels (compensated), and the PV panels' cell temperature. Both

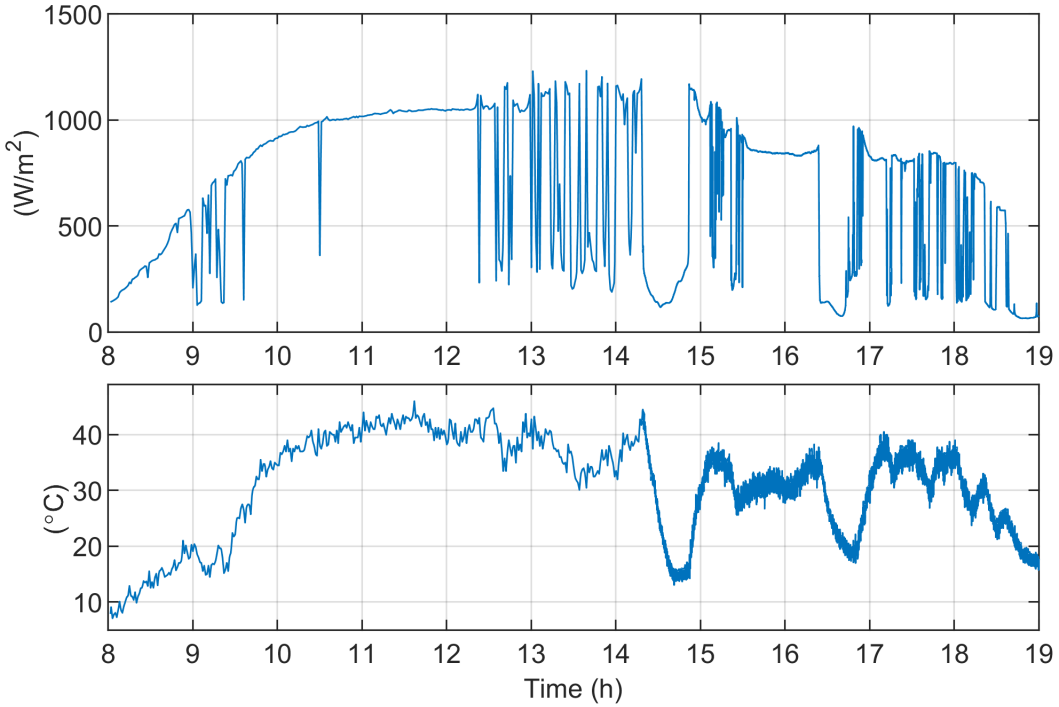


Figure 5.12: One-second resolution irradiance and temperature data utilized (day 1).

datasets were collected by the industry partner Strata Solar, corresponding to the operation of a 5.04 MW PV plant located in North Carolina, USA, during April 8th, 2022 (day 1) and April 9th, 2022 (day 2).

### 5.2.1 Extended Kalman Filter Performance

In this work, the EKF is implemented with a timestep of 1 second. This value can be increased up to the adaptive MPC timestep to reduce the computational burden if necessary. Figure 5.14 demonstrates the performance of the EKF when estimating the battery SOC utilizing voltage and current dc sensors with an SNR of 71dB . The results show that if an accurate mathematical model of the battery is utilized in the EKF, its performance is highly accurate.

Figures (5.15a)-(5.15d) present zoomed in plots of the EKF SOC estimation. Note that the largest estimation errors occur at inflection points in the SOC curve. This is because

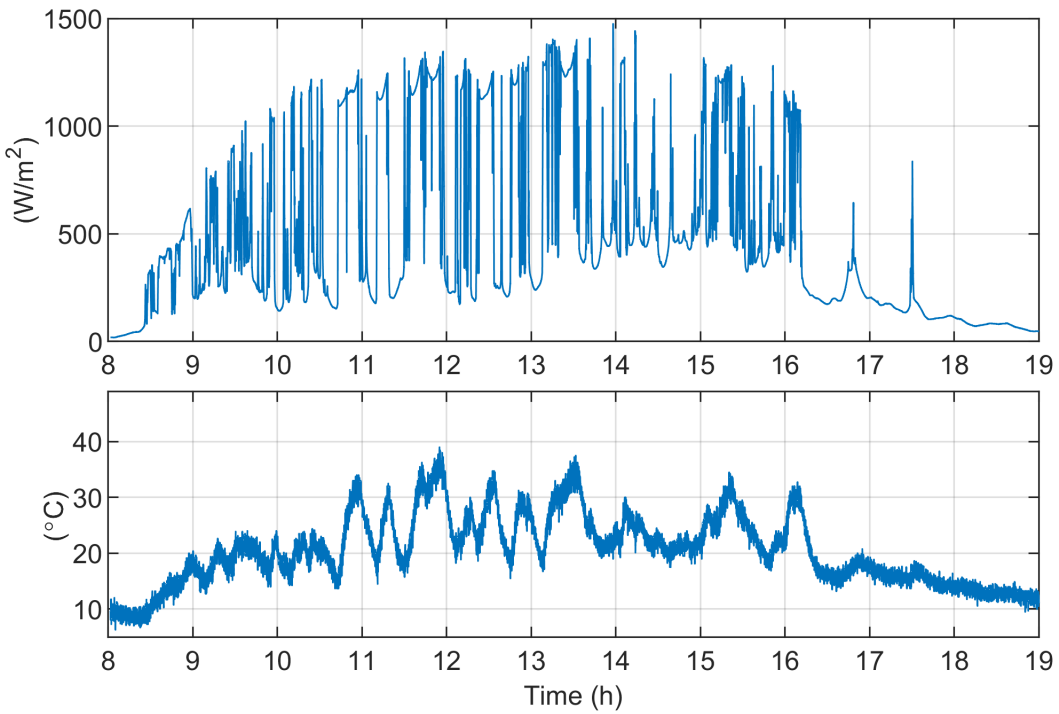


Figure 5.13: One-second resolution irradiance and temperature data utilized (day 2).

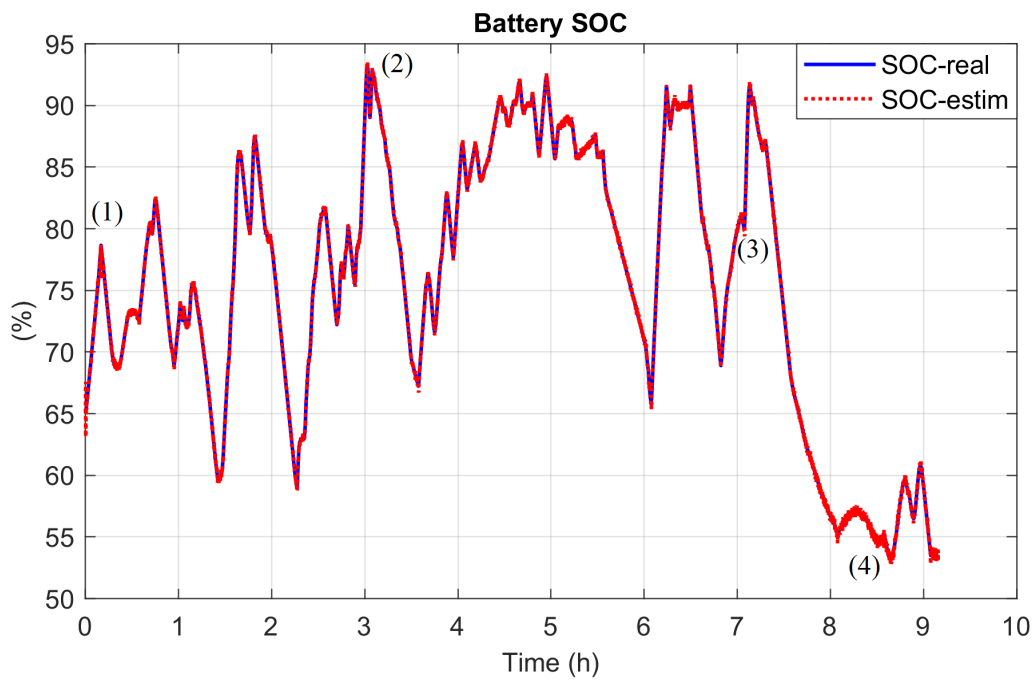


Figure 5.14: SOC estimation performance from a 9-hour long real-time simulation.

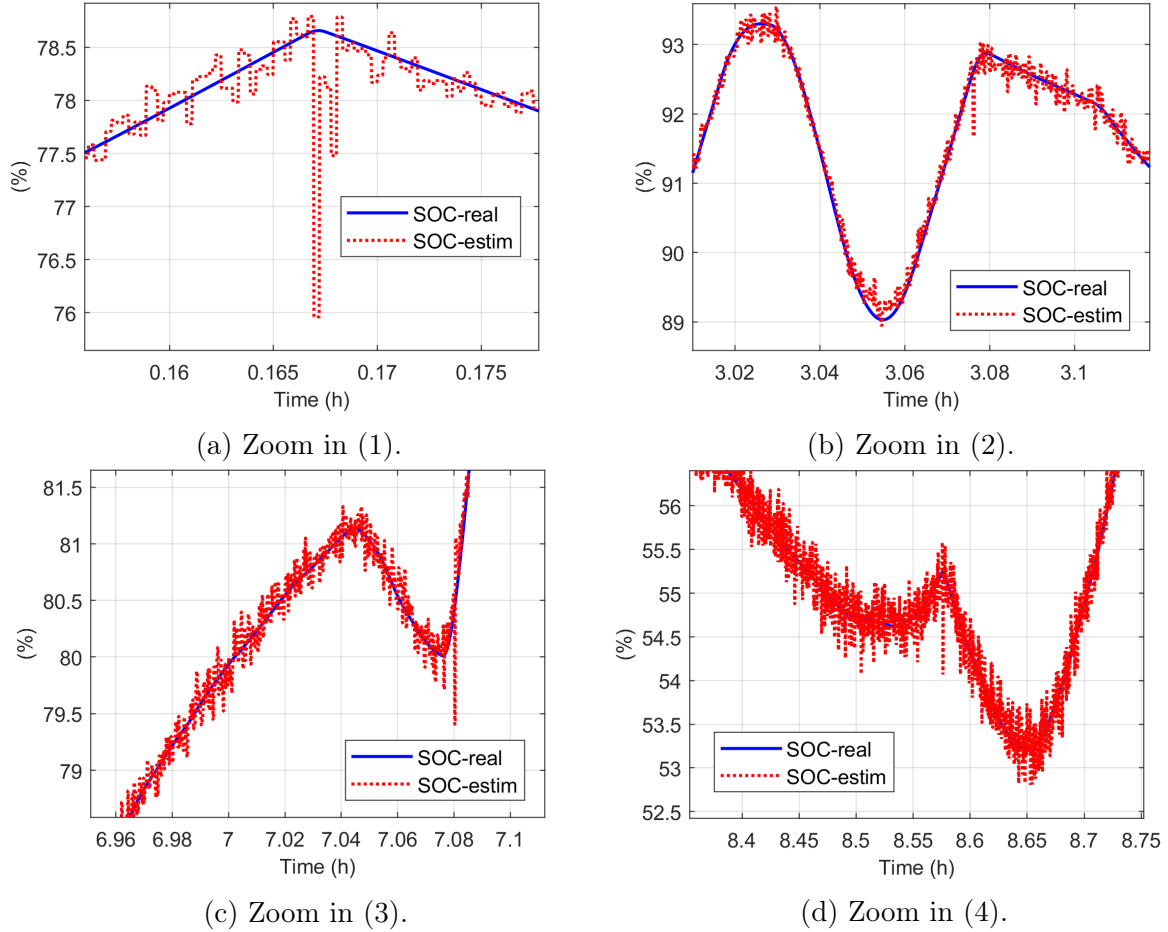


Figure 5.15: Modeling accuracy of the battery SOC estimation.

the EKF reacts to the battery's non-linearities by performing constant linearizations around the nominal operating. Therefore, at moments when the battery current changes from discharging to charging modes (or vice-versa), there is a strong non-linearity caused by the change in the efficiency gain between the modes, which cannot be instantly captured by the EKF, and may cause transient error spikes in its estimation. Nevertheless, these fast transient spikes can be easily filtered by passing the EKF SOC estimation through a LPF with a time constant equivalent to the adaptive MPC timestep.

In reality, as the parameters from the EKF SS mathematical model are further from the actual battery parameters, the estimation errors will increase. Therefore, an error

sensitivity analysis is carried out for the EKF SOC estimation.

In this test, the parameters from the battery's mathematical model given by (5.22) are modified to represent modeling errors. Note that the errors are only inserted in the battery model implemented in the Kalman filter, hence the original battery parameters inside the plant are kept the same. This represents a scenario in which the method utilized for extracting the battery parameters has inaccuracies.<sup>3</sup> Two tests are executed: (i) all battery parameters, i.e., ( $R_s$ ,  $R_{ts}$ ,  $R_{tl}$ ,  $C_c$ ,  $C_{ts}$ , and  $C_{tl}$ ) are modeled with +5% errors, (ii) all parameters are modeled with -5% errors.

Results from the error sensitivity test are displayed in Fig. 5.16. It was found that the RMSE errors presented a close match between (i) and (ii), with case (i) having slightly higher errors. Moreover, in (i), the SOC estimation was usually above the actual SOC during discharging modes (positive battery current), and below the actual SOC during charging modes (negative battery current). The opposite was found for case (ii). Considering a perfect extraction of the battery parameters is never possible, and that the battery parameters will also be a function of temperature, aging, etc, it must be acknowledged that the EKF estimation will always present an error margin. Consequently, the BESS should always be designed not to reach the actual battery maximum limit of 100%.

From the results, it was found that neither the transient error spike caused by the change between battery charging or discharging modes, nor the error offset caused by including modeling errors inside the EKF battery SS model caused the EKF to lose its convergence.

---

<sup>3</sup>An example of a method to extract second-order lithium-ion battery parameters is presented in [77].

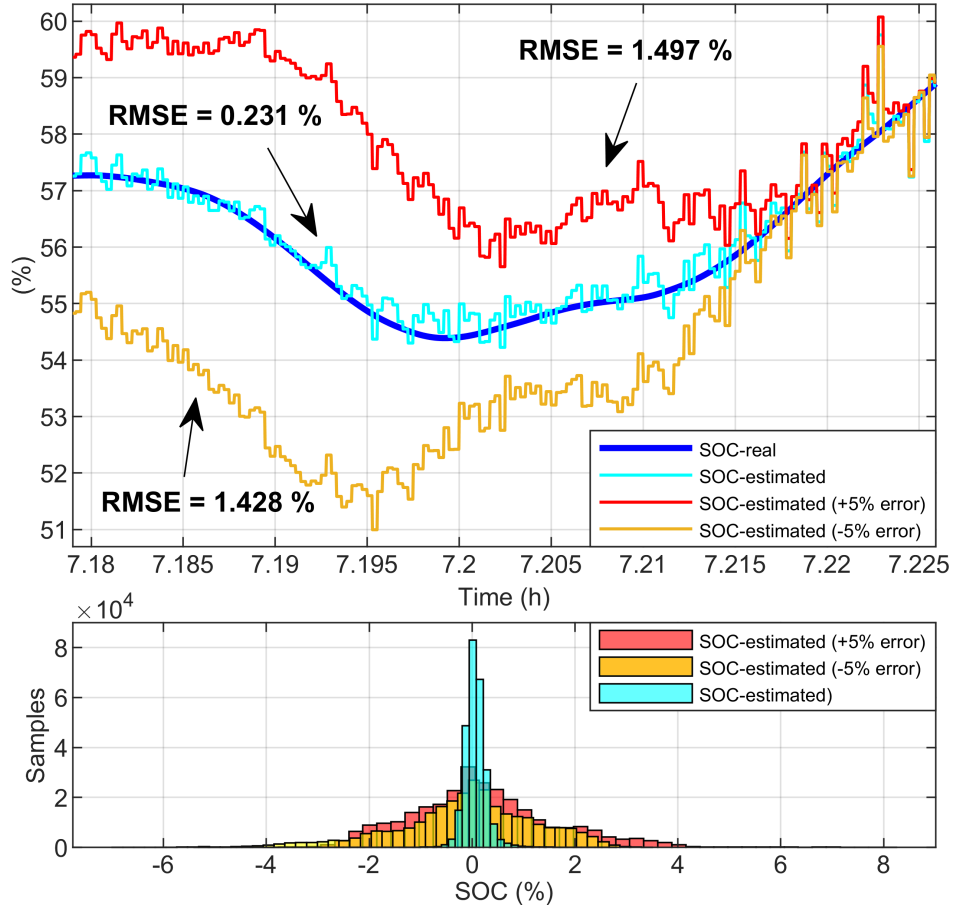


Figure 5.16: SOC estimation performance under parameter errors.

### 5.2.2 Power Regulation Performance

In this section, we analyze the capability of the hybrid PV plant to follow power setpoints given by an external EMS and maintain power reserves while operating under the high irradiance intermittency conditions from Figs. 5.12 and 5.13. For this test, the power setpoint is built based on two sources: (i) a forecast of what the available PV average output power will be in intervals of 30 minutes with  $\pm 10\%$  forecast errors, and (ii) a PJM regulation D signal with 1 MW range (0.5 MW up/0.5 MW down) with 2-seconds resolution. Figures 5.17 and 5.18 display the actual maximum available PV power ( $P_{mp}$ ), the average  $P_{mp}$  in intervals of 30 minutes, and the estimated  $P_{mp}$  (including forecast

errors). Moreover, the estimated  $P_{mp}$  with forecast errors is capped at the PV maximum output power of 2 MW, hence forecast errors may be smaller during PV clipping events. Note the forecast errors are inserted here to represent a more realistic scenario, in which the actual average available power from the plant does not match the expectations.

When the PV availability is lower than expected, the BESS is used to help the system maintain its power setpoint tracking, and it can also be used to provide downward power regulation if the power setpoint becomes negative. In addition, the power reserves setpoint ( $P_{ref}^{reserves}$ ) of the hybrid PV plant, which represents a headroom to be maintained at all times, starts at 500 kW, and is reduced down to 0 or increased up to 0.5 MW as the regulation signal ranges from +500 kW down to 0 or below. This means that when providing upward regulation, the power reserves constraint is alleviated. Alternatively, the plant could have been set to provide only downward regulation while continuously maintaining power reserves for FFR.

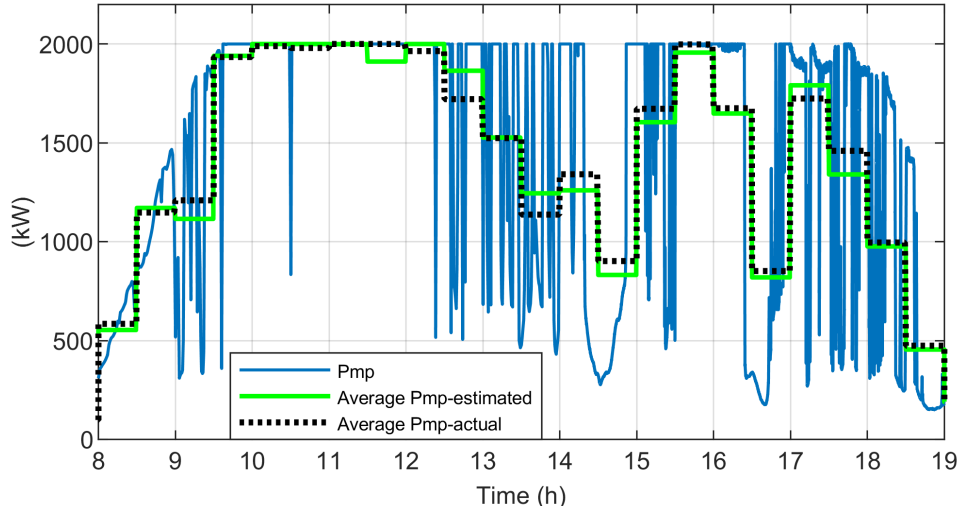


Figure 5.17: PV maximum available power for day 1.

Figure 5.19 displays the regulation signal utilized for each day. As previously mentioned, the power setpoint signal sent to the hybrid PV plant in each day is built by combining the regulation signal from Fig. 5.19 with the estimated average PV power for

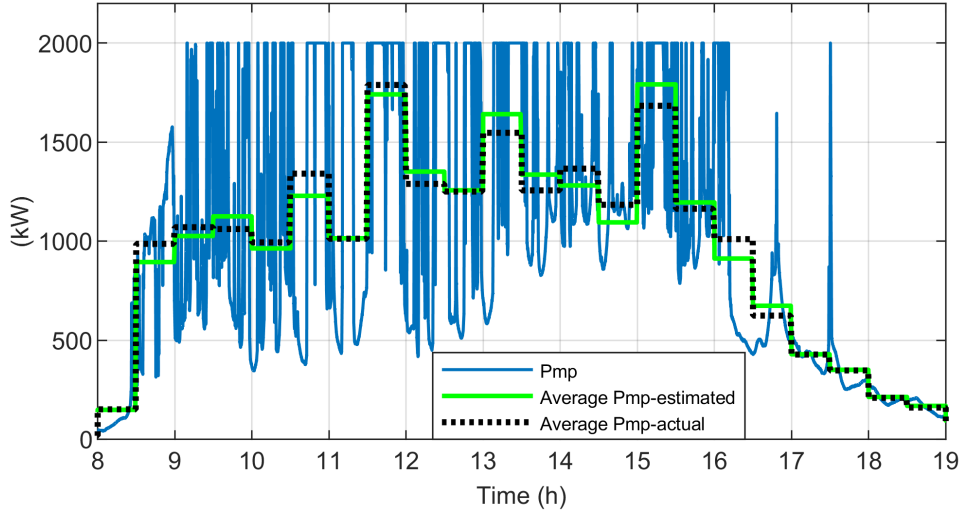


Figure 5.18: PV maximum available power for day 2.

30-minutes intervals from Figs. 5.17 and 5.18.

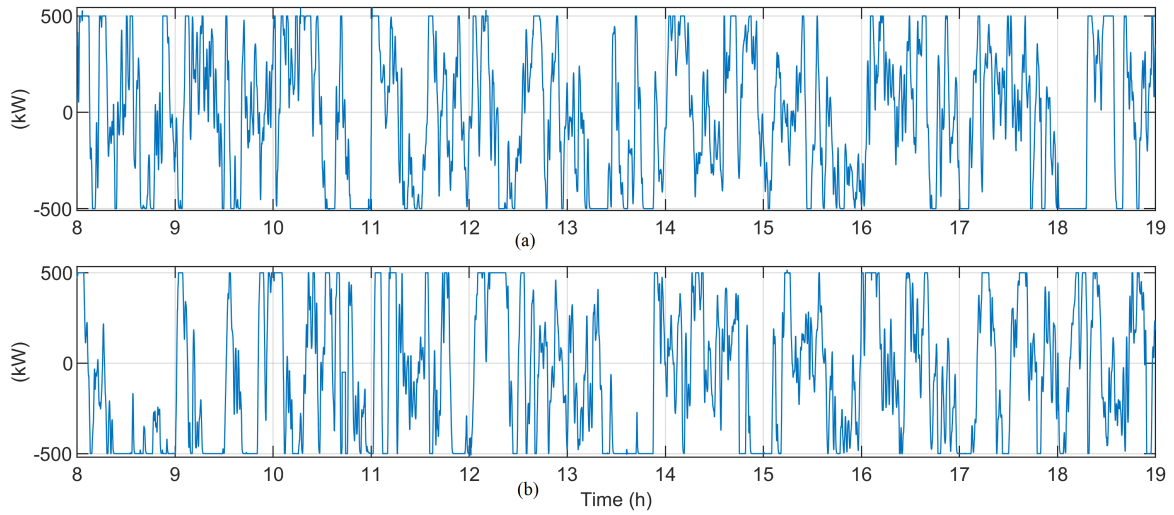


Figure 5.19: PJM regulation D signal: (a) day 1, (b) day 2.

If there were no forecast errors or components losses, the average power setpoint would match the average available PV power with zero-mean oscillations added by the regulation signal, and as long as the BESS charge was sufficient to handle the regulation oscillations and PV intermittency, the system would be able to track the power setpoints

perfectly.<sup>4</sup> Nevertheless, due to ac/dc conversion losses, battery losses, transformer losses, and errors in the PV forecast, the actual available AC power will be less than the expected average PV available power. To address the losses, in this work, the part of the power setpoint corresponding to the average available PV from Figs. 5.17 and 5.18 is reduced by a reliability factor ( $K_r$ ), set to 0.95 in this case. That is a necessary compromise for maintaining adequate power setpoint tracking. An example of a case in which this factor is reduced further for providing a larger regulation service is presented later in this Chapter.

Results from the hybrid PV plant operation for day 1 are presented in Figs. 5.20 and 5.21. In this case, the hybrid PV plant was able to match the power setpoint with an RMSE of 103.38 kW, and a maximum power output error of 835.23 kW. As shown in Fig. 5.20(c), during certain moments, large errors can be observed throughout the day-long simulation. There are three main reasons for power output errors: (i) the BESS SOC is considerably depleted, and the MPC is unable to match the power setpoint while enforcing the BESS SOC minimum constraint of 30% SOC; (ii) due to a clouding event, the PV output power is reduced to a point where even with the BESS operating at nominal power, the power setpoint cannot be reached, and (iii) if a power reserves violations occur due to a severe clouding condition.

The third case can happen if high clouding events coincide with moments of high power setpoint request. When this happens, if the hybrid PV plant is asked to maintain power reserves, the problem becomes infeasible and either the power setpoint or the power reserves must be violated. The trade-off between these two can be adjusted by increasing the power reserves constraint softness. This case is discussed in the results for the second day.

Errors originated from battery SOC depletion can be observed in Fig. 5.20(b) around

---

<sup>4</sup>Ignoring scenarios in which high power reserves are requested.

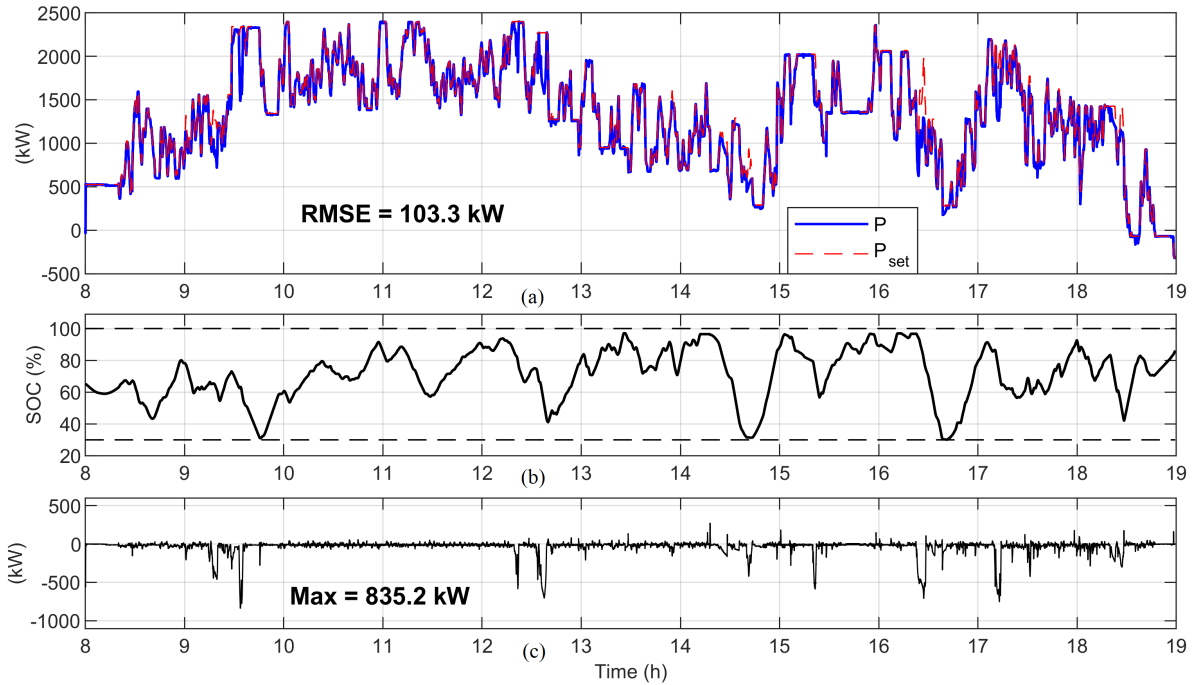


Figure 5.20: Hybrid PV Plant performance in day 1: (a) power output, (b) battery SOC, (c) power output error.

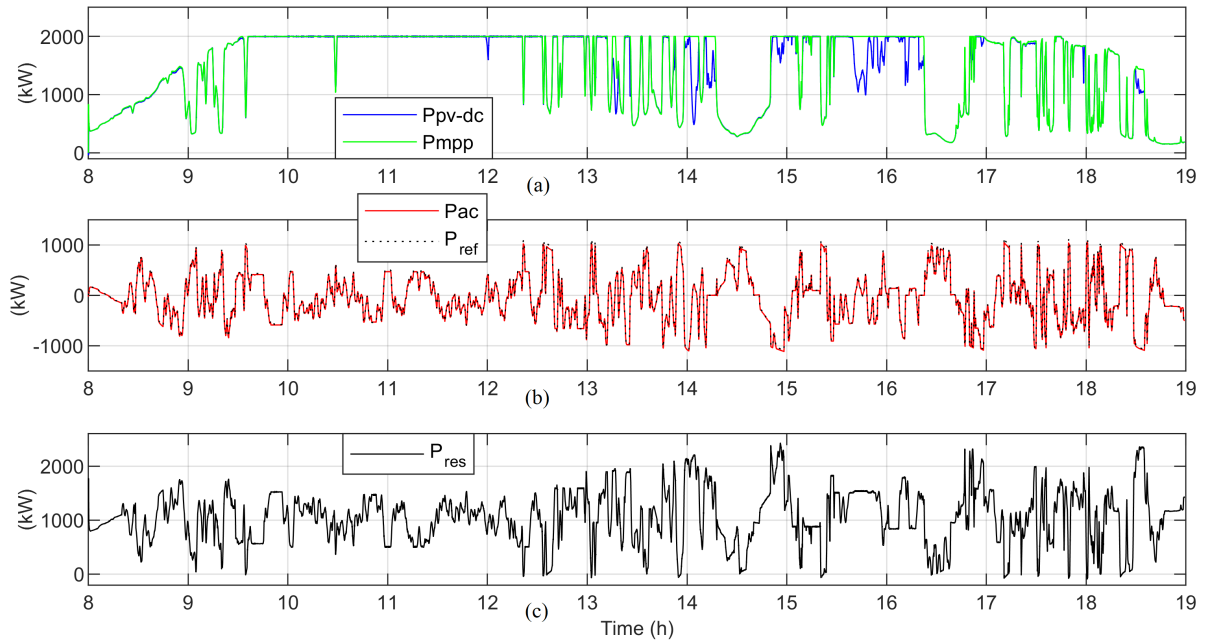


Figure 5.21: Hybrid PV Plant performance in day 1: (a) PV output power, (b) BESS output power, (c) power reserves.

hours 9.75, 14.75, and 16.6, whereas errors due to the hybrid PV plant reaching its output power limits can be noticed at hours 9.6, 12.6, 16.4, and 17.25. At hour 17.25, for example, the PV availability drops below 500 kW, and even though the battery operates at nominal output power (1 MW), the power setpoint of 2 MW cannot be maintained, causing a large output error. It is important to mention that the BESS output power is limited by the battery current constraints (650 A during discharge, and 550 A during charge). Therefore, as the SOC drops, the actual maximum power that can be provided by the BESS is reduced due to the voltage drop.

Next, we analyze the impact of reducing the average output power setpoint request by a factor of 0.75, corresponding to a case in which the expected power from the plant assumes a more conservative approach. Figures 5.22 and 5.23 display the results. The results reveal that the plant can provide a much closer power setpoint tracking if a less aggressive request is demanded from it. In this case, the plant power output achieved an RMSE of 28.9 kW, close to four times smaller, and a maximum error of 372.4 kW. The error corresponded to the end of the simulation, when the system was asked to provide negative output power regulation, causing the battery to reach its upper SOC constraint.

It is worth mentioning that this issue can be avoided by reducing the battery SOC setpoint once negative power outputs might be required. However, here it is kept the same for a more equal comparison. The main drawback of this scenario, when compared to the previous one, is the reduction of the average output power. Nevertheless, this example highlights how oversizing the plant (or requesting a less aggressive power output) can allow the system to provide very accurate power regulation services. Furthermore, by comparing Fig. 5.20(c) with 5.22(c), it can be noticed how in the second case the system is able to maintain higher power reserves due to the extra PV power curtailment.

Figures 5.24 and 5.25 display the hybrid PV plant performance for the second day. Despite the high irradiance intermittency, the hybrid PV plant presented smaller power

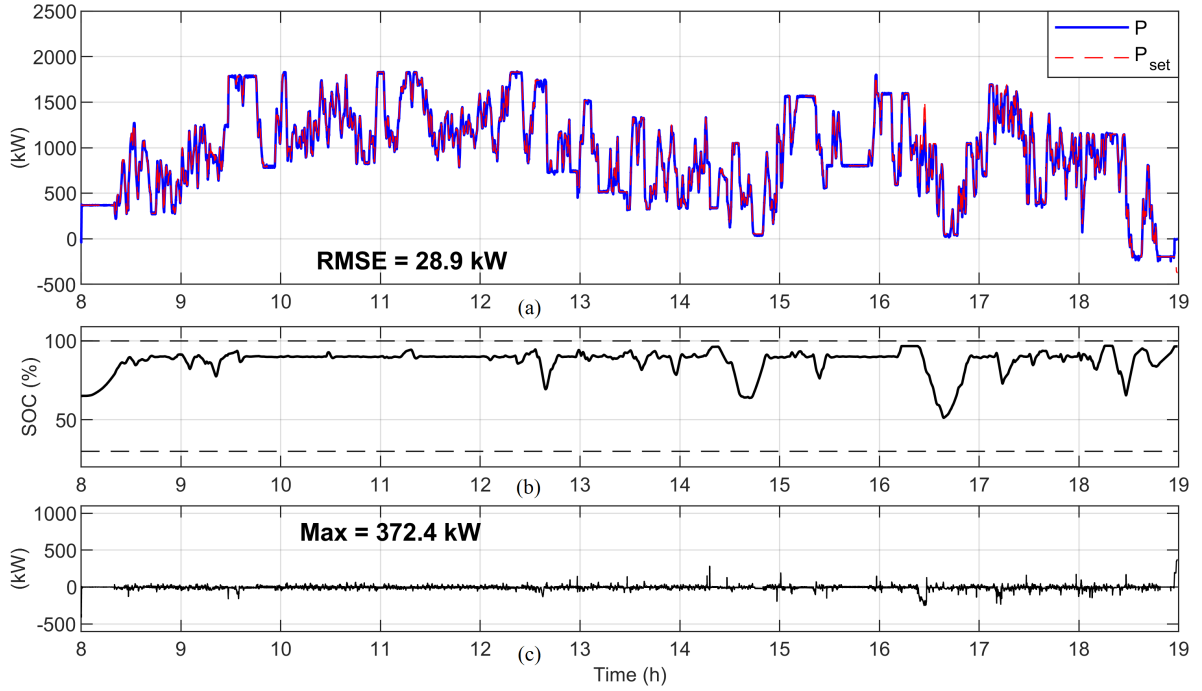


Figure 5.22: Hybrid PV Plant performance in day 1 with a lower power request: (a) power output, (b) battery SOC, (c) power output error.

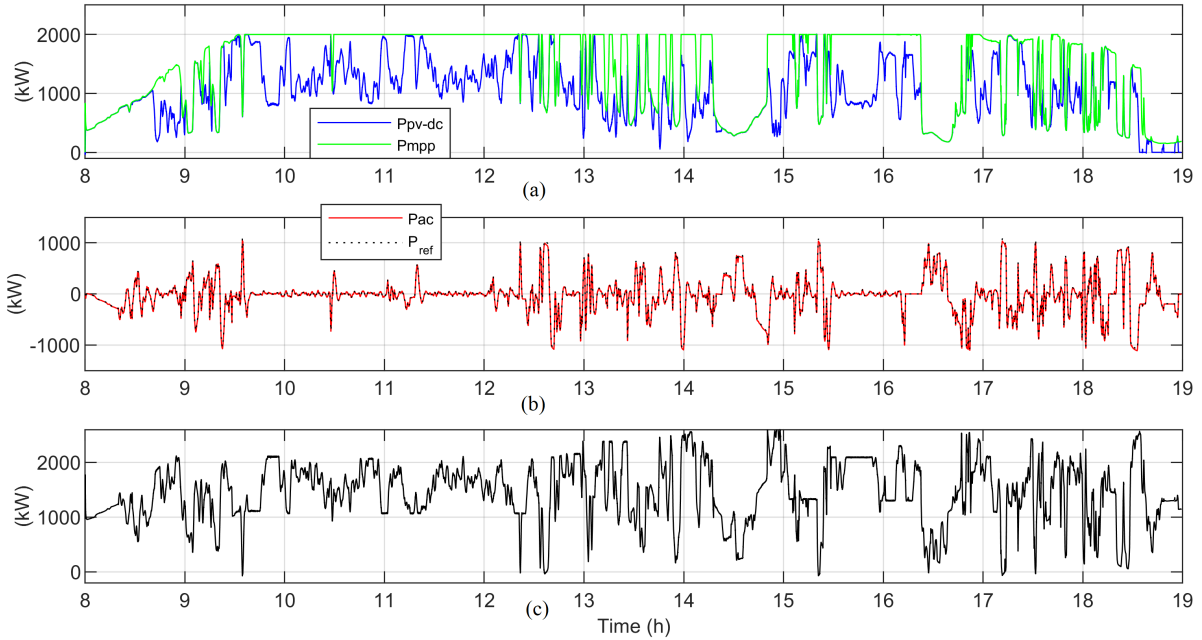


Figure 5.23: Hybrid PV Plant performance in day 1 with a lower power request: (a) PV output power, (b) BESS output power, (c) power reserves.

output errors in the second day, with an RMSE of 56.04 kW (around 2.6% of the PV capacity), and a maximum error of 529.35 kW. A fast error transient is observed around hour 8.4. That error occurs because the regulation signal from Fig. 5.19(b) is only activated after 1200 seconds of simulation. When it activates, its initial value of  $-500$  kW causes an instantaneous error (soon compensated by the system).

The main errors observed for the second day of operation happen near hours 11.1, 12, 14.5 and 14.8. The errors between hours 14.5 and 14.8 are related to battery SOC depletion, in which the MPC starts to degrade its power tracking performance to avoid SOC violations. Note that around hour 14.25 the SOC pushes the BESSs SOC up to its highest possible value to prepare for the upcoming demand.

On the other hand, during hours 11.1, 12, and 13, there is sufficient SOC reserves, and the battery is not reaching its nominal ratings; however, there are power output errors. Those occur due to the MPC compromise to maintain robust power reserves. Here, the MPC power reserves constraints are implemented with a degree of softness (specifics in the appendix) to allow violations under unfeasible scenarios. Due to the significant PV irradiance drop, the system reaches its minimum power reserves constraints, and its softness is weighted to decide how much of the power output should be sacrificed in exchange for smaller violations. An example is shown in Fig. 5.26. During that moment of low irradiance availability, increasing the BESS output power would violate the constraint further; therefore, a compromise between constraint violation and output power errors is maintained. This relation can be tuned as needed by adjusting the minimum and maximum output variables ECR gains ( $y_{i,\text{ECR}}^{\min}, y_{i,\text{ECR}}^{\max}$ ).

In addition, a positive error is observed close to hour 17.8. It occurred because the battery was at its maximum SOC, so the hybrid PV plant was incapable of absorbing power for a downward regulation, even though the PV output was set to zero. Note that in this work the actual battery maximum SOC is set to 97.5% (given in the appendix), to

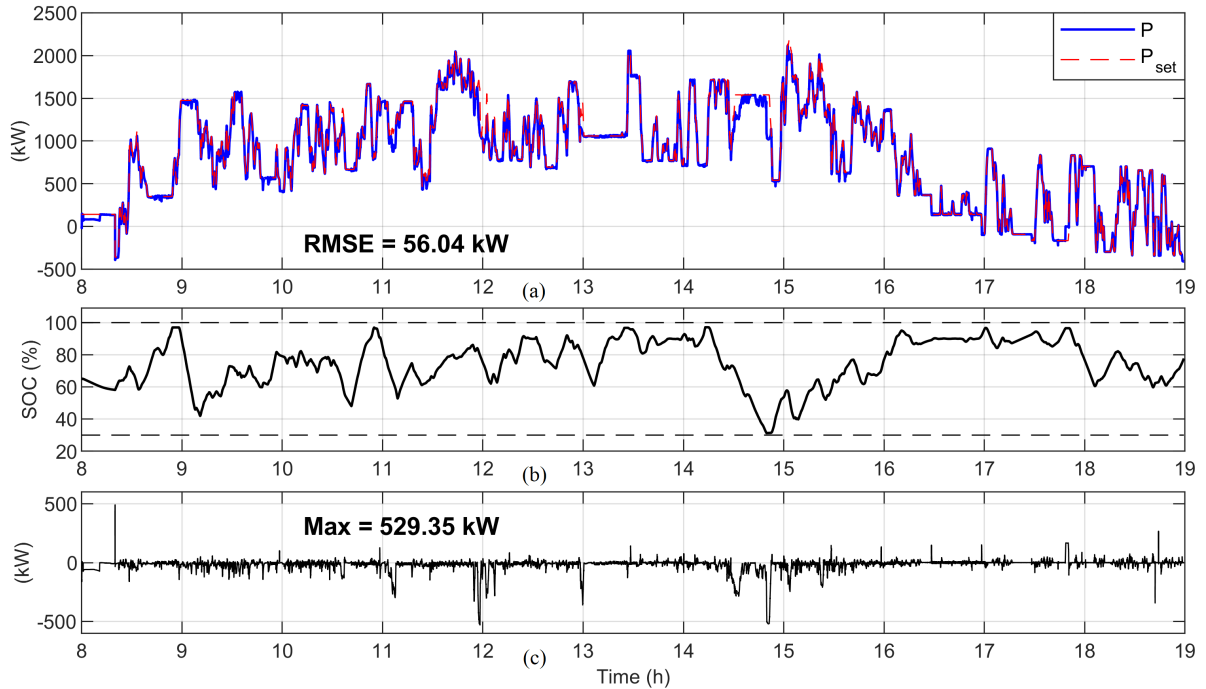


Figure 5.24: Hybrid PV Plant performance in day 2: (a) power output, (b) battery SOC, (c) power output error.

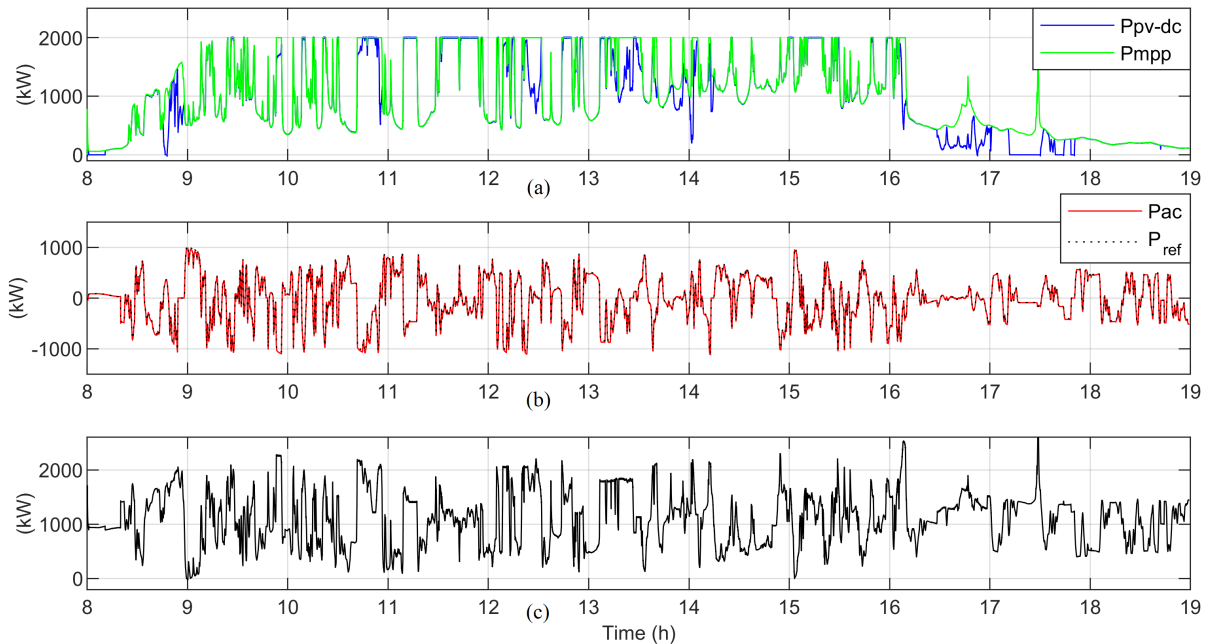


Figure 5.25: Hybrid PV Plant performance in day 2: (a) PV output power, (b) BESS output power, (c) power reserves.

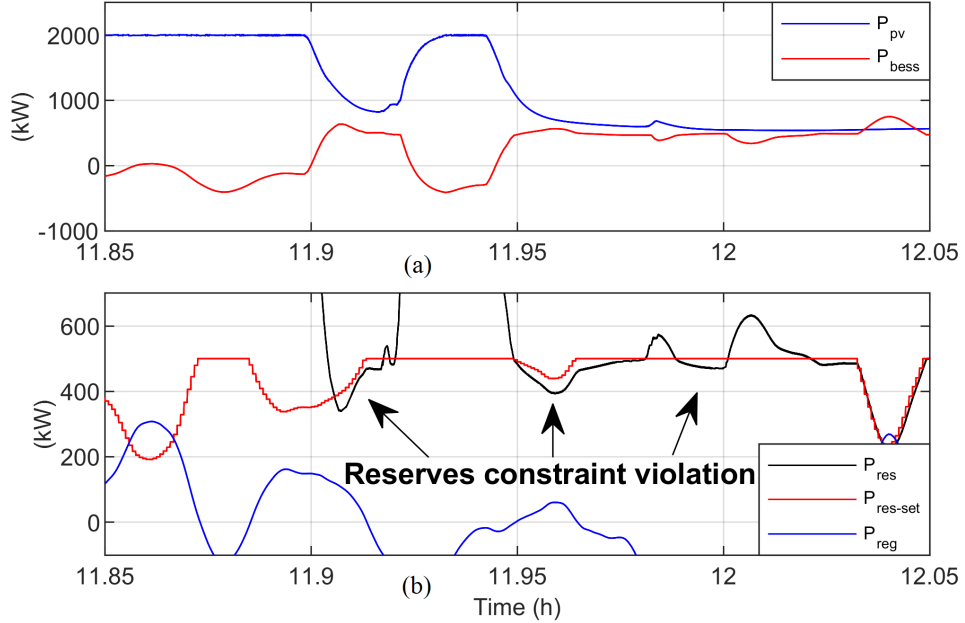


Figure 5.26: Moment of power reserves violations (a) PV and BESS output power, (b) power reserves and regulation D signal.

account for errors in the EKF estimation, and a hard threshold is set at SOC 96% so that whenever the battery SOC reaches 96%, its maximum current constraint is updated to zero with a ramp rate limiter of 50 A per second, such that until the SOC drops, the battery cannot be charged further. Once the charge is below 96%, the constraint is once again ramped back to the original setting (-550 A, in this work). The hard threshold can slightly reduce the MPC optimization performance, since it will expect the BESS SOC to reach up to 97.5%, but it is important to avoid numerical instabilities in the solver in case a small violation in the battery SOC occurs.<sup>5</sup>

Figure 5.27 displays the the battery voltage and current through the second day. Clearly, the battery maximum and minimum current constraints are tightly maintained throughout operation.

---

<sup>5</sup>Recall that the battery SOC constraints are designed with a small degree of softness.

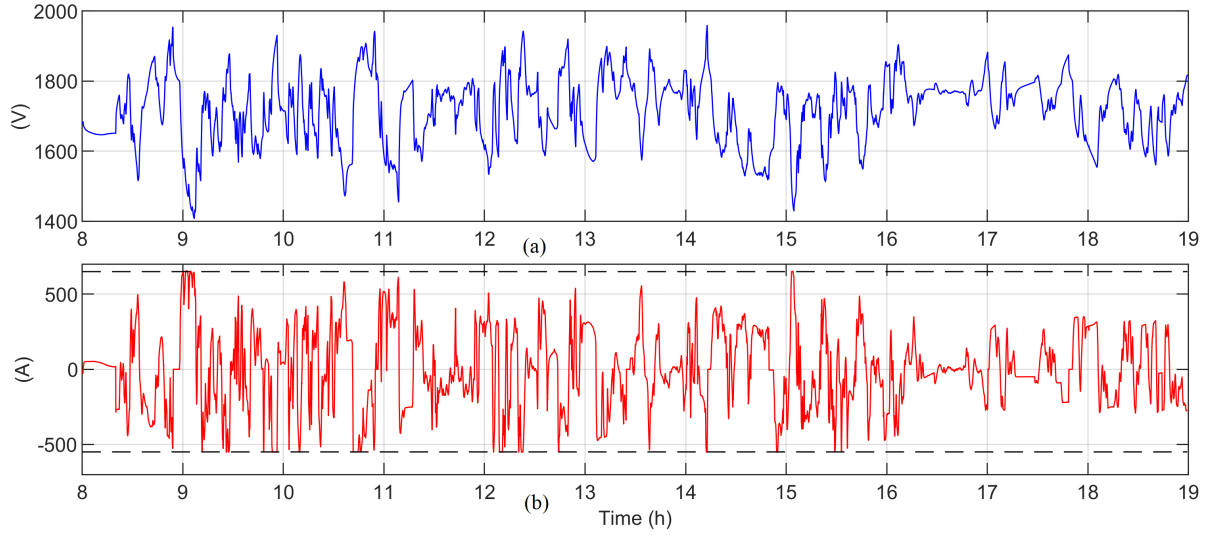


Figure 5.27: Battery measurements in day 2: (a) Voltage, (b) Current.

### 5.2.3 Comparison Against a Thermal Unit

In this section, the power regulation of the hybrid PV plant is compared to the regulation capability of a typical thermal unit from PJM. A thermal generator has a typical ramping capability of 0.01 p.u. per minute. In [78], Kirby et al. analyzed the total ramping capability of CAISO (California ISO), PJM, and WAPA (Western Area Power Administration's). The study showed that PJM has the largest ramping capability among the areas, with an average unit ramping (up/down) of 0.8 MW per minute, and an average unit size of 121 MW. The machine model is built with governor, turbine, and reheater time constants given in [79], and its power setpoint ramping capability is set to 0.8 MW per minute. Then, it is requested to follow the power setpoint established for the hybrid PV plant for the second day of operation under a power regulation signal of 1.5 MW (750 kW up/750 kW down). Because the thermal unit cannot absorb power, the power setpoint from Fig. 5.24(a) is raised by 750 kW for the entire operation. Results are displayed in Fig. 5.28. The overall maximum power error is a close match to the error of the hybrid PV plant, with a slightly better performance. Nevertheless, due to its slower response to

transients, the thermal machine presents a more significant power output RMSE.

For this comparison, the hybrid PV plant is set to follow a power regulation signal of 1.5 MW. Furthermore, the SOC setpoint is dropped from 90% to 80% to have more room for downward regulation, and the reliability gain  $K_r$  is reduced to 0.8 to reduce the impact of SOC avoiding cases of SOC depletion. Results are shown in Fig. 5.29. It can be seen that the hybrid PV plant can present a smoother tracking while there is enough SOC available to maintain the regulation. However, due to the lower power setpoint requested around hours 17 to 18, the battery reached its upper SOC limit, being then unable to provide downward regulation.

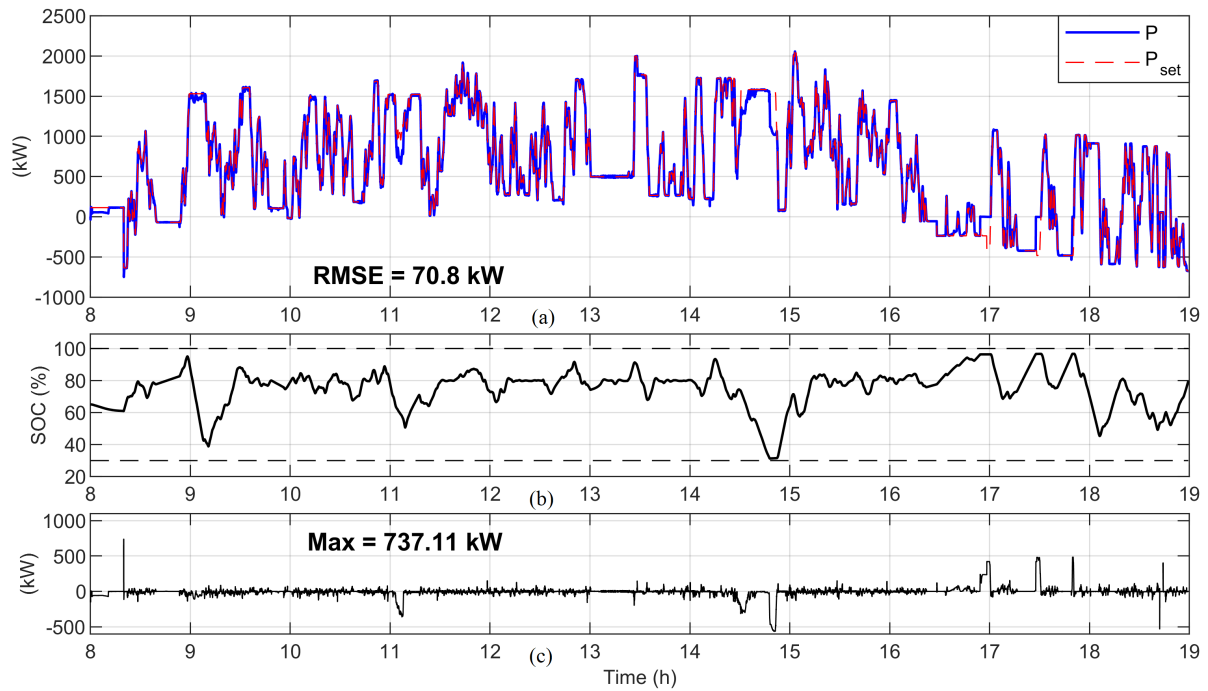


Figure 5.28: Hybrid PV Plant performance in day 2 with a regulation signal of 1.5 MW: (a) power output, (b) power output error.

The results confirm the expectations that the hybrid PV plant can provide superior regulation performance due to its fast IBR controls. While the thermal unit has a typical ramping of 0.8 MW per minute with a response time constant of 10 seconds or more, the

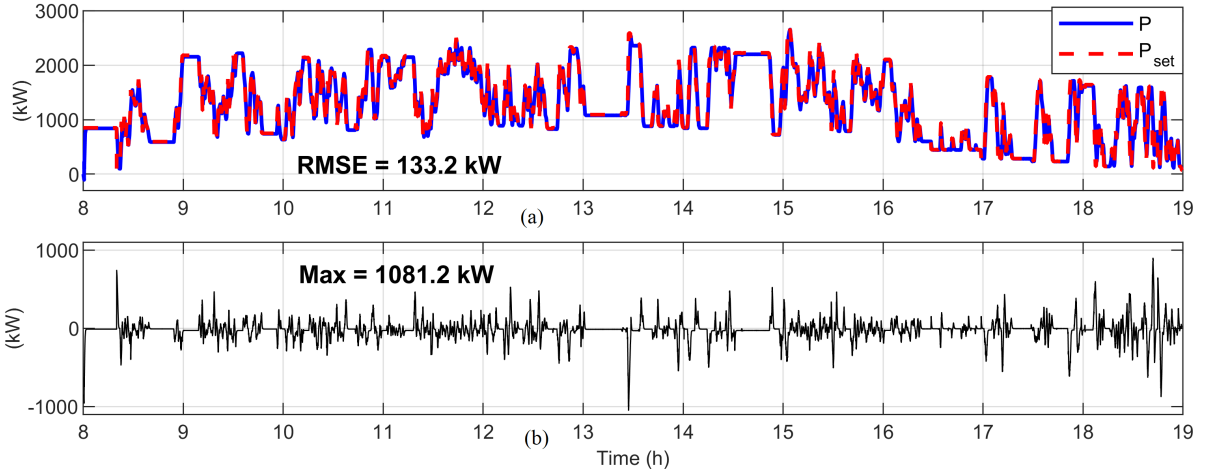


Figure 5.29: Thermal generator performance following same power setpoint from day 2 with a regulation signal of 1.5 MW: (a) power output, (b) power output error.

hybrid PV plant implemented can provide a ramping of 0.6 MW per second.

### 5.3 Conclusion

In this chapter, a feedback control strategy to optimally operate a hybrid PV plant while considering power reserves has been presented. The system combines optimal control with the advanced power curtailment algorithm presented in Chapter 3 to form a PV plant capable of maintaining reserves for providing both regulation and/or FFR services for grid support. An adaptive MPC is developed to handle the nonlinearities of the plant model. Detailed EMT models are developed for the PV systems, grid-following inverter, and lithium-ion battery model to provide an accurate representation of their losses and limitations. Furthermore, an EKF is implemented for estimating the battery SOC, and an error sensitivity is executed to assess its limitations. Day-long simulations with realistic datasets are executed in a real-time simulator to validate the performance of the method under days of high irradiance intermittency. Results demonstrate the system can provide high quality power regulation services as well as maintain robust power reserves as long as

its requested setpoints do not violate its constraints. Furthermore, constraint softness and tunable control objective weights can be adjusted in real-time to shift priorities between power regulation, power reserves, or battery SOC management.

# Chapter 6

## Summary and Future Work

This research has focused on three main sub-topics related to grids with high DER participation: advanced power curtailment algorithms for PV systems with FFR capabilities, methods to implement real-time co-simulation testbeds that can simulate distribution feeders under high DER participation, and an optimal operation of a hybrid PV system capable of providing regulation services as well as high-quality fast dispatching power reserves for supporting low-inertia grids.

In Chapter 2, a P&O-based power curtailment technique was introduced to improve the power setpoint tracking performance of a PV system during fast transients. The technique was developed specifically for PV systems that operate without power reserves, making it suitable for systems with low complexity. Chapter 2 also described the implementation of an EMT model of a single-stage PV system that is compatible with real-time simulators.

In Chapter 3, a more complex power curtailment technique was presented, allowing a PV system to not only provide fast power setpoint tracking, but also to estimate its maximum available power in real-time for maintaining fast-dispatchable power reserves. In addition, a new tracking method was also introduced, which utilizes information from

the MPPE to improve the power setpoint tracking performance both in transient and steady-state conditions.

In order to simulate PV models with advanced GSFs in the EMT domain and study their performance when integrated to distribution feeders, it is necessary to develop new modeling techniques. This is because TS simulations are not fast enough to capture the control performance from IBRs during transients. On the other hand, simulating an entire feeder in the EMT domain can demand unrealistic computational capabilities for real-time or faster-than-real-time tests. Therefore, Chapter 4 proposed a new real-time EMT-TS modeling architecture that allows the simulation of selected IBRs in the EMT domain while simulating the rest of a distribution feeder in the phasor domain. The testbed was found to reduce the computational burden up to eight times, while maintaining a close match with an EMT-domain benchmark. This testbed can be used to simulate PV systems running the algorithm from Chapter 3 while integrated to a distribution feeder, for example.

Even though PV systems can operate with the algorithm explained in Chapter 3 to provide power reserves with FFR capabilities, they are still susceptible to drop either their power output or their power reserves during moments of fast irradiance intermittency. Therefore, by integrating a GFL BESS to a PV plant, a hybrid PV plant with robust power reserves can be built. In Chapter 5, the optimal operation of a hybrid PV plant running the algorithm from Chapter 3 is presented, demonstrating its capability to follow upward and downward regulation signals during days with very high irradiance intermittency while taking into account power reserves constraints.

## 6.1 Future Work

As previously mentioned, this work was divided into three main sub-topics: power curtailment of PV systems with advanced GSFs, real-time simulation of feeders with high participation of IBRs with advanced GSFs, and the optimal operation of a hybrid PV plant with advanced GSFs.

Inside the topic of power curtailment of PV systems, there are several challenges related to the performance of power setpoint tracking and MPPE algorithms under partial shading conditions. Therefore, one direction is in the improvement of algorithms from Chapter 2 and 3 with a focus on operating under partial shading conditions.

For the real-time co-simulation, there are multiple tests that can be carried out to further validate the performance of the testbed. For instance, the validation of the proposed testbed against its EMT benchmark for an operation under multiple grid-forming BESS units is an excellent next step. Moreover, a coupling method that allows the simulation of units that can switch between grid-forming and grid-following modes must be developed. An additional possibility is to test the performance of the proposed testbed under fault scenarios, which has not been analyzed and will require further work. Such analyses will help answering important questions in the area of real-time EMT-TS simulations.

Finally, regarding the optimal performance of a hybrid PV plant, in this work, the objective function only included the plant output power and battery SOC. Further improvements and more complex scenarios can be undertaken in which the objective function also includes the voltage profile, and/or the inclusion of a slower MPC loop that is focused on finding the most appropriate SOC and power setpoints to be sent as references to the MPC presented here. An outer MPC can be used to reduce the impact of PV forecast errors and to ensure that the power setpoints and/or power reserves are always maintained.

## REFERENCES

- [1] V. Gevorgian, “Highly accurate method for real-time active power reserve estimation for utility-scale photovoltaic power plants,” National Renewable Energy Lab.(NREL), Golden, CO (United States), Tech. Rep., 2019.
- [2] H. D. Tafti, A. Sangwongwanich, Y. Yang, J. Pou, G. Konstantinou, and F. Blaabjerg, “An adaptive control scheme for flexible power point tracking in photovoltaic systems,” *IEEE Transactions on Power Electronics*, vol. 34, no. 6, pp. 5451–5463, 2018.
- [3] F. Plumier, P. Aristidou, C. Geuzaine, and T. Van Cutsem, “Co-simulation of electromagnetic transients and phasor models: A relaxation approach,” *IEEE Transactions on Power Delivery*, vol. 31, no. 5, pp. 2360–2369, 2016.
- [4] L. Dai, Y. Xia, M. Fu, and M. Mahmoud, “Discrete-time model predictive control,” *Advances in Discrete Time Systems*, pp. 77–116, 2012.
- [5] T. Schmidt, M. Calais, E. Roy, A. Burton, D. Heinemann, T. Kilper, and C. Carter, “Short-term solar forecasting based on sky images to enable higher PV generation in remote electricity networks,” *Renewable Energy and Environmental Sustainability*, vol. 2, p. 23, 2017.
- [6] M. Lipperheide, J. Bosch, and J. Kleissl, “Embedded nowcasting method using cloud speed persistence for a photovoltaic power plant,” *Solar Energy*, vol. 112, pp. 232–238, 2015.
- [7] I. C. Change *et al.*, “The physical science basis,” 2021.
- [8] W. J. Cole, B. A. Frew, P. J. Gagnon, J. Richards, Y. Sun, R. M. Margolis, and M. A. Woodhouse, “Sunshot 2030 for photovoltaics (PV): Envisioning a low-cost PV future,” National Renewable Energy Lab.(NREL), Golden, CO (United States), Tech. Rep., 2017.
- [9] G. Barbose, S. Weaver, and N. Darghouth, “Tracking the sun vii: An historical summary of the installed price of photovoltaics in the united states from 1998 to 2013,” Lawrence Berkeley National Lab.(LBNL), Berkeley, CA (United States), Tech. Rep., 2014.
- [10] S. Zhang, Y. Fu, X. Yang, and W. Xu, “Assessment of mid-to-long term energy saving impacts of nearly zero energy building incentive policies in cold region of china,” *Energy and Buildings*, vol. 241, p. 110938, 2021.

- [11] I. S. Association *et al.*, “IEEE Std. 1547-2018,” *Standard for Interconnection and Interoperability of Distributed Energy Resources with Associated Electric Power Systems Interfaces*, 2018.
- [12] California Public Utilities Commission *et al.*, “Electric rule no. 21 generating facility interconnections,” 2016.
- [13] K. Ishaque, Z. Salam, M. Amjad, and S. Mekhilef, “An improved particle swarm optimization (PSO)-based MPPT for PV with reduced steady-state oscillation,” *IEEE Transactions on Power Electronics*, vol. 27, no. 8, pp. 3627–3638, 2012.
- [14] A. Hoke and D. Maksimović, “Active power control of photovoltaic power systems,” in *2013 1st IEEE Conference on Technologies for Sustainability (SusTech)*. IEEE, 2013, pp. 70–77.
- [15] R. G. Wandhare and V. Agarwal, “Precise active and reactive power control of the PV-DGS integrated with weak grid to increase PV penetration,” in *2014 IEEE 40th Photovoltaic Specialist Conference (PVSC)*. IEEE, 2014, pp. 3150–3155.
- [16] W. Cao, Y. Ma, J. Wang, L. Yang, J. Wang, F. Wang, and L. M. Tolbert, “Two-stage PV inverter system emulator in converter based power grid emulation system,” in *2013 IEEE Energy Conversion Congress and Exposition*. IEEE, 2013, pp. 4518–4525.
- [17] A. Sangwongwanich, Y. Yang, F. Blaabjerg, and H. Wang, “Benchmarking of constant power generation strategies for single-phase grid-connected photovoltaic systems,” *IEEE Transactions on Industry Applications*, vol. 54, no. 1, pp. 447–457, 2017.
- [18] A. Narang, H. D. Tafti, C. D. Townsend, G. Farivar, J. Pou, G. Konstantinou, and S. Vazquez, “An algorithm for fast flexible power point tracking in photovoltaic power plants,” in *IECON 2019-45th Annual Conference of the IEEE Industrial Electronics Society*, vol. 1. IEEE, 2019, pp. 4387–4392.
- [19] V. Gevorgian and B. O’Neill, “Advanced grid-friendly controls demonstration project for utility-scale PV power plants,” National Renewable Energy Lab.(NREL), Golden, CO (United States), Tech. Rep., 2016.
- [20] A. Sangwongwanich, Y. Yang, F. Blaabjerg, and D. Sera, “Delta power control strategy for multistring grid-connected PV inverters,” *IEEE Transactions on Industry Applications*, vol. 53, no. 4, pp. 3862–3870, 2017.
- [21] A. Sangwongwanich, Y. Yang, and F. Blaabjerg, “A sensorless power reserve control strategy for two-stage grid-connected PV systems,” *IEEE Transactions on Power Electronics*, vol. 32, no. 11, pp. 8559–8569, 2017.

- [22] E. I. Batzelis, G. E. Kampitsis, and S. A. Papathanassiou, “Power reserves control for PV systems with real-time MPP estimation via curve fitting,” *IEEE Transactions on Sustainable Energy*, vol. 8, no. 3, pp. 1269–1280, 2017.
- [23] Y. Zhu, H. Wen, G. Chu, Y. Hu, X. Li, and J. Ma, “High-performance photovoltaic constant power generation control with rapid maximum power point estimation,” *IEEE Transactions on Industry Applications*, vol. 57, no. 1, pp. 714–729, 2020.
- [24] X. Li, H. Wen, Y. Zhu, L. Jiang, Y. Hu, and W. Xiao, “A novel sensorless photovoltaic power reserve control with simple real-time MPP estimation,” *IEEE Transactions on Power Electronics*, vol. 34, no. 8, pp. 7521–7531, 2018.
- [25] A. F. Hoke, M. Shirazi, S. Chakraborty, E. Muljadi, and D. Maksimovic, “Rapid active power control of photovoltaic systems for grid frequency support,” *IEEE Journal of Emerging and Selected Topics in Power Electronics*, vol. 5, no. 3, pp. 1154–1163, 2017.
- [26] H. D. Tafti, G. Konstantinou, C. D. Townsend, G. G. Farivar, A. Sangwongwanich, Y. Yang, J. Pou, and F. Blaabjerg, “Extended functionalities of photovoltaic systems with flexible power point tracking: recent advances,” *IEEE Transactions on Power Electronics*, vol. 35, no. 9, pp. 9342–9356, 2020.
- [27] Mathworks, “PV Array Model,” <https://www.mathworks.com/help/physmod/sps/powersys/ref/pvarray.html>, 1, accessed: 2020-08-10.
- [28] A. Yazdani and R. Iravani, *Voltage-Sourced Converters in Power Systems: modeling, control, and applications*. John Wiley & Sons, 2010.
- [29] V. Paduani, “Design, modeling, and simulation of a bidirectional three-phase PWM AC/DC converter,” Master’s thesis, Villanova University, 2019.
- [30] EPRI, “Distributed PV Monitoring and Feeder Analysis,” [https://dpv.epri.com/measurement\\_data.html](https://dpv.epri.com/measurement_data.html), 1, accessed: 2020-08-10.
- [31] M. G. Villalva, J. R. Gazoli, and E. Ruppert Filho, “Comprehensive approach to modeling and simulation of photovoltaic arrays,” *IEEE Transactions on Power Electronics*, vol. 24, no. 5, pp. 1198–1208, 2009.
- [32] E. I. Batzelis, “Simple PV performance equations theoretically well founded on the single-diode model,” *IEEE Journal of Photovoltaics*, vol. 7, no. 5, pp. 1400–1409, 2017.
- [33] C. Mole, “The Lambert W function,” <https://www.mathworks.com/matlabcentral/fileexchange/43419-the-lambert-w-function>, MATLAB Central File Exchange. Retrieved: December 23, 2020.

- [34] E. I. Batzelis, A. Junyent-Ferre, and B. C. Pal, “MPP estimation of PV systems keeping power reserves under fast irradiance changes,” in *IEEE Power & Energy Society General Meeting (PESGM)*. IEEE, 2020, pp. 1–5.
- [35] H. P. Gavin, “The Levenberg-Marquardt algorithm for nonlinear least squares curve-fitting problems,” *Department of Civil and Environmental Engineering, Duke University* <http://people.duke.edu/~hpgavin/ce281/lm.pdf>, pp. 1–19, 2019.
- [36] B. Marion, A. Anderberg, C. Deline, J. del Cueto, M. Muller, G. Perrin, J. Rodriguez, S. Rummel, T. J. Silverman, F. Vignola *et al.*, “New data set for validating PV module performance models,” in *2014 IEEE 40th Photovoltaic Specialist Conference (PVSC)*. IEEE, 2014, pp. 1362–1366.
- [37] J. Marcos, L. Marroyo, E. Lorenzo, D. Alvira, and E. Izco, “From irradiance to output power fluctuations: the PV plant as a low pass filter,” *Progress in Photovoltaics: Research and Applications*, vol. 19, no. 5, pp. 505–510, 2011.
- [38] H. B. Nielsen *et al.*, *Damping parameter in Marquardt’s method*. IMM, 1999.
- [39] Q. Long, H. Yu, F. Xie, N. Xie, and D. Lubkeman, “Diesel generator model parameterization for microgrid simulation using hybrid box-constrained Levenberg-Marquardt algorithm,” *IEEE Transactions on Smart Grid*, vol. 12, no. 2, pp. 943–952, 2020.
- [40] E. I. Batzelis and S. A. Papathanassiou, “A method for the analytical extraction of the single-diode PV model parameters,” *IEEE Transactions on Sustainable Energy*, vol. 7, no. 2, pp. 504–512, 2015.
- [41] V. Paduani, L. Song, B. Xu, and N. Lu, “Maximum power reference tracking algorithm for power curtailment of photovoltaic systems,” in *2021 IEEE Power & Energy Society General Meeting (PESGM)*. IEEE, 2021, pp. 01–05.
- [42] E. Saloux, A. Teyssedou, and M. Sorin, “Explicit model of photovoltaic panels to determine voltages and currents at the maximum power point,” *Solar Energy*, vol. 85, no. 5, pp. 713–722, 2011.
- [43] Mouser Electronics, “Texas Instruments AMC1303x high-precision delta-sigma modulators”, <https://www.mouser.it/new/TexasInstruments/ti-amc1303-modulators/>, retrieved: March 31, 2021.
- [44] F. Edstrom, J. Rosenlind, P. Hilber, and L. Soder, “Modeling impact of cold load pickup on transformer aging using Ornstein-Uhlenbeck process,” *IEEE Transactions on Power Delivery*, vol. 27, no. 2, pp. 590–595, 2012.
- [45] A. Sangwongwanich, Y. Yang, D. Sera, H. Soltani, and F. Blaabjerg, “Analysis and modeling of interharmonics from grid-connected photovoltaic systems,” *IEEE Transactions on Power Electronics*, vol. 33, no. 10, pp. 8353–8364, 2018.

- [46] D. Pattabiraman, J. Tan, V. Gevorgian, A. Hoke, C. Antonio, and D. Arakawa, “Impact of frequency-watt control on the dynamics of a high der penetration power system,” in *2018 IEEE Power & Energy Society General Meeting (PESGM)*. IEEE, 2018, pp. 1–5.
- [47] V. Paduani, M. Kaban, and P. Singh, “Small-signal stability of islanded-microgrids with dc side dynamics of inverters and saturation of current controllers,” in *2019 IEEE Power & Energy Society General Meeting (PESGM)*. IEEE, 2019, pp. 1–5.
- [48] J. Matevosyan, J. MacDowell, N. Miller, B. Badrzadeh, D. Ramasubramanian, A. Isaacs, R. Quint, E. Quitmann, R. Pfeiffer, H. Urdal, T. Prevost, V. Vittal, D. Woodford, S. H. Huang, and J. O’Sullivan, “A future with inverter-based resources: Finding strength from traditional weakness,” *IEEE Power and Energy Magazine*, vol. 19, no. 6, pp. 18–28, 2021.
- [49] V. Paduani and N. Lu, “Implementation of a two-stage PV system testbed with power reserves for grid-support applications,” in *2021 North American Power Symposium (NAPS)*. IEEE, 2021, pp. 1–6.
- [50] H. Jain, B. A. Bhatti, T. Wu, B. Mather, and R. Broadwater, “Integrated transmission-and-distribution system modeling of power systems: State-of-the-art and future research directions,” *Energies*, vol. 14, no. 1, p. 12, 2021.
- [51] D. Shu, X. Xie, Q. Jiang, Q. Huang, and C. Zhang, “A novel interfacing technique for distributed hybrid simulations combining EMT and transient stability models,” *IEEE Transactions on Power Delivery*, vol. 33, no. 1, pp. 130–140, 2017.
- [52] A. Shirsat, V. Muthukaruppan, R. Hu, N. Lu, M. Baran, D. Lubkeman, and W. Tang, “Hierarchical multi-timescale framework for operation of dynamic community microgrid,” *arXiv preprint arXiv:2011.10087*, 2020.
- [53] R. S. Mongrain, Z. Yu, and R. Ayyanar, “A real-time simulation testbed for hierarchical control of a renewable energy-based microgrid,” in *2019 IEEE Texas Power and Energy Conference (TPEC)*. IEEE, 2019, pp. 1–6.
- [54] D. Athaide, J. Qin, and Y. Zou, “MATLAB/Simulink-based electromagnetic transient-transient stability hybrid simulation for electric power systems with converter interfaced generation,” in *2019 IEEE Texas Power and Energy Conference (TPEC)*. IEEE, 2019, pp. 1–6.
- [55] H. Konara Mudiyanselage, “Interfacing a transient stability model to a real-time electromagnetic transient simulation using dynamic phasors,” Master’s thesis, University of Manitoba, 2020.

- [56] X. Song, H. Cai, T. Jiang, T. Sennewald, J. Kircheis, S. Schlegel, L. N. Martinez, Y. Benzetta, and D. Westermann, “Research on performance of real-time simulation based on inverter-dominated power grid,” *IEEE Access*, vol. 9, pp. 1137–1153, 2020.
- [57] IEEE 123 Node Test Feeder. [Online]. Available: <http://sites.ieee.org/pes-testfeeders/resources/>
- [58] C. Dufour, J. Mahseredjian, and J. Bélanger, “A combined state-space nodal method for the simulation of power system transients,” *IEEE Transactions on Power Delivery*, vol. 26, no. 2, pp. 928–935, 2010.
- [59] B. Xu, V. Paduani, D. Lubkeman, and N. Lu, “A novel grid-forming voltage control strategy for supplying unbalanced microgrid loads using inverter-based resources,” *arXiv preprint arXiv:2111.09464*, 2021.
- [60] V. D. Paduani, H. Yu, B. Xu, and N. Lu, “A unified power-setpoint tracking algorithm for utility-scale PV systems with power reserves and fast frequency response capabilities,” *IEEE Transactions on Sustainable Energy*, vol. 13, no. 1, pp. 479–490, 2021.
- [61] F. Xie, C. McEntee, M. Zhang, and N. Lu, “An asynchronous real-time co-simulation platform for modeling interaction between microgrids and power distribution systems,” in *2019 IEEE Power & Energy Society General Meeting (PESGM)*. IEEE, 2019, pp. 1–5.
- [62] A. Shirsat, V. Muthukaruppan, R. Hu, V. Paduani, B. Xu, L. Song, Y. Li, N. Lu, M. Baran, D. Lubkeman *et al.*, “Sa-hmts: A secure and adaptive hierarchical multi-timescale framework for resilient load restoration using a community microgrid,” *arXiv preprint arXiv:2202.05252*, 2022.
- [63] H. Yuan, J. Tan, Y. Zhang, S. Murthy, S. You, H. Li, Y. Su, and Y. Liu, “Machine learning-based PV reserve determination strategy for frequency control on the WECC system,” in *2020 IEEE Power & Energy Society Innovative Smart Grid Technologies Conference (ISGT)*. IEEE, 2020, pp. 1–5.
- [64] J. Chang, Y. Du, E. G. Lim, H. Wen, X. Li, and L. Jiang, “Coordinated frequency regulation using solar forecasting based virtual inertia control for islanded microgrids,” *IEEE Transactions on Sustainable Energy*, vol. 12, no. 4, pp. 2393–2403, 2021.
- [65] V. Gevorgian, R. Wallen, P. Koralewicz, E. Mendiola, S. Shah, and M. Morjaria, “Provision of grid services by PV plants with integrated battery energy storage system,” National Renewable Energy Lab.(NREL), Golden, CO (United States), Tech. Rep., 2020.

- [66] S. Teleke, M. E. Baran, A. Q. Huang, S. Bhattacharya, and L. Anderson, “Control strategies for battery energy storage for wind farm dispatching,” *IEEE Transactions on Energy Conversion*, vol. 24, no. 3, pp. 725–732, 2009.
- [67] M. Z. Daud, A. Mohamed, and M. Hannan, “An improved control method of battery energy storage system for hourly dispatch of photovoltaic power sources,” *Energy Conversion and Management*, vol. 73, pp. 256–270, 2013.
- [68] S. Teleke, M. E. Baran, S. Bhattacharya, and A. Q. Huang, “Optimal control of battery energy storage for wind farm dispatching,” *IEEE Transactions on Energy Conversion*, vol. 25, no. 3, pp. 787–794, 2010.
- [69] U. R. Nair, M. Sandelic, A. Sangwongwanich, T. Dragičević, R. Costa-Castelló, and F. Blaabjerg, “An analysis of multi objective energy scheduling in pv-bess system under prediction uncertainty,” *IEEE Transactions on Energy Conversion*, vol. 36, no. 3, pp. 2276–2286, 2021.
- [70] M. Lei, Z. Yang, Y. Wang, H. Xu, L. Meng, J. C. Vasquez, and J. M. Guerrero, “An mpc-based ess control method for PV power smoothing applications,” *IEEE Transactions on Power Electronics*, vol. 33, no. 3, pp. 2136–2144, 2017.
- [71] X. Li, D. Hui, and X. Lai, “Battery energy storage station (bess)-based smoothing control of photovoltaic (PV) and wind power generation fluctuations,” *IEEE Transactions on Sustainable Energy*, vol. 4, no. 2, pp. 464–473, 2013.
- [72] H. Cha, T.-K. Vu, and J.-E. Kim, “Design and control of proportional-resonant controller based photovoltaic power conditioning system,” in *2009 IEEE Energy Conversion Congress and Exposition*. IEEE, 2009, pp. 2198–2205.
- [73] M. Chen and G. A. Rincon-Mora, “Accurate electrical battery model capable of predicting runtime and iv performance,” *IEEE Transactions on Energy Conversion*, vol. 21, no. 2, pp. 504–511, 2006.
- [74] A. Bemporad, M. Morari, and N. L. Ricker, “Model predictive control toolbox user’s guide,” *The Mathworks*, 2010.
- [75] J. Vetter, P. Novák, M. R. Wagner, C. Veit, K.-C. Möller, J. Besenhard, M. Winter, M. Wohlfahrt-Mehrens, C. Vogler, and A. Hammouche, “Ageing mechanisms in lithium-ion batteries,” *Journal of Power Sources*, vol. 147, no. 1-2, pp. 269–281, 2005.
- [76] MATLAB, “Model predictive control toolbox release notes,” <https://www.mathworks.com/help/mpc/release-notes.html>, MATLAB. Retrieved: March 10, 2022.

- [77] Z. Chen, Y. Fu, and C. C. Mi, “State of charge estimation of lithium-ion batteries in electric drive vehicles using extended kalman filtering,” *IEEE Transactions on Vehicular Technology*, vol. 62, no. 3, pp. 1020–1030, 2012.
- [78] B. Kirby and M. Milligan, “Method and case study for estimating the ramping capability of a control area or balancing authority and implications for moderate or high wind penetration,” National Renewable Energy Lab., Golden, CO (US), Tech. Rep., 2005.
- [79] S. Abd-Elazim and E. Ali, “Firefly algorithm-based load frequency controller design of a two area system composing of PV grid and thermal generator,” *Electrical Engineering*, vol. 100, no. 2, pp. 1253–1262, 2018.
- [80] Texas Instruments, “TMS320C28x floating point unit and instruction set reference guide,” 2008.

## Appendix

Table 6.1: Testbed Parameters from Chapter 3

PV Array	Power	612 kW
	Module	CS6P-250P
	Size (parallel $\times$ series)	153 $\times$ 16
	$V_{mpp}$ , $I_{mpp}$	481.6 V, 1270 A
Inverter	Power, Frequency	500 kVA, 60 Hz
	$L_f$ , $r_L$	100 $\mu$ H, 3 m $\Omega$
	$C_{dc}$	5000 $\mu$ F
	PI ( $v_{dc}$ )	$K_p = 1$ , $K_i = 250$
	PI ( $i_d$ , $i_q$ )	$K_p = 0.7$ , $K_i = 50$
Maximum Power Point Estimation	$\Delta G_{max}$	200 W/m <sup>2</sup> /s
	$\Delta T_{max}$	3 °C/min
	Measurement window	100 samples
	$a$ ( $\eta$ gain)	3
	Damping $\eta$ range	[ $10^{-6}$ , $10^{-3}$ ]
	Sampling freq. ( $f_s = 1/T_s$ )	20 Hz
	LM period ( $T_{LM}$ )	5 s
Flexible Power Point Tracking	Frequency ( $f_{step} = 1/T_{step}$ )	4 Hz
	$V_{step-min}$ / $V_{step-b}$	0.75 / 2 V
	$K_{tr}$	0.002
	Threshold $\Delta P_{ref,th}$	50 kW/s
	Threshold $dp_{th}$	15 kW
	Threshold $dp/dv$	667 W/V
Diesel Generator	Power, Frequency	3.125 MVA, 60 Hz
	Voltage (line-line)	2400 V (RMS)
	Droop	5%
	Inertia (H)	1.07 p.u.
	Governor ( $T_g$ )	0.2
	Turbine ( $T_t$ )	0.35

## Levenberg-Marquardt Computational Cost

The computational cost of the LM parameter update process that corresponds to the slowest period of the proposed algorithm ( $T_{LM}$ ) is summarized in Table 6.2. The number of operations for each LM iteration is a function of the size of the measurement window,  $N$ . The number of CPU cycles required to execute each operation on a Texas Instrument TMS320C28x Floating Point Unit [80] is used as a benchmark. The Lambert  $W$  and the logarithmic functions are not included because their calculations should be substituted by look-up tables for the implementation in a microprocessor.

Table 6.2: Required CPU cycles for one LM iteration.

Operation	Cycles	No of Operations	Total Cycles
+ / -	2	$40 + N \times 30$	$80 + N \times 60$
$\times$	24	$56 + N \times 51$	$1344 + N \times 1224$
$\div$	63	$12 + N \times 6$	$756 + N \times 378$
Max / Min	7	$6 + N \times 3$	$42 + N \times 21$
Comparator	1	7	7
Absolute	2	12	24

## MPC Parameters

Prediction horizon = 400, control horizon = 20,  $T_{mpc} = 3$  s.  $w_1^y = 3$ ,  $w_2^y = 0$ ,  $w_3^y = 0.1$ ,  $w_4^y = 0$ ,  $w_5^y = 0$ ,  $s_1^y = 2$  MVA,  $s_1^y = 1200$  A,  $s_3^y = 1$ ,  $s_4^y = 4$  MVA,  $s_5^y = 2$  MVA,  $w_1^{\Delta u} = 0.01$ ,  $w_2^{\Delta u} = 0.002$ ,  $s_1^{\Delta u} = 280$  A/s,  $s_2^{\Delta u} = 800$  kVA/s,  $y_{1,ECR}^{\min} = 1$ ,  $y_{1,ECR}^{\max} = 1$ ,  $y_{2,ECR}^{\min} = 0.5$ ,  $y_{2,ECR}^{\max} = 0.5$ ,  $y_{3,ECR}^{\min} = 0.5$ ,  $y_{3,ECR}^{\max} = 0.5$ ,  $y_{4,ECR}^{\min} = 4$ ,  $y_{4,ECR}^{\max} = 5$ ,  $y_{5,ECR}^{\min} = 0.3$ ,  $y_{5,ECR}^{\max} = 0.3$ ,  $u_1^{\min} = -130$  A,  $u_1^{\max} = 130$  A,  $u_2^{\min} = -400$  kVA,  $u_2^{\max} = 400$  kVA,  $y_1^{\min} = -1$  MVA,  $y_1^{\max} = 3$  MVA,  $y_2^{\min} = -550$  A,  $y_2^{\max} = 650$  A,  $y_3^{\min} = 0.295$ ,  $y_3^{\max} = 0.975$ ,  $y_4^{\min} = -3$  MVA,  $y_4^{\max} = 3$  MVA,  $y_5^{\min} = 0$ ,  $y_5^{\max} = 2$  MVA,

Table 6.3: Testbed Parameters From Chapter 5

PV Arrays	Power	$4 \times 612 \text{ kW}$
	Module	CS6P-250P
	Size (parallel $\times$ series)	$153 \times 16$
	$V_{mp}, I_{mp}$	$481.6 \text{ V}, 1270 \text{ A}$
PV Inverter	Power, Frequency	$500 \text{ kVA}, 60 \text{ Hz}$
	Voltage (line-line)	$200 \text{ V (RMS)}$
	$\eta_{pv}$	96.5%
	Ramp Rate	0.2 p.u./s
	$L_f, r_L$	$100 \mu\text{H}, 3 \text{ m}\Omega$
	$C_{dc}$	$5000 \mu\text{F}$
	PI ( $v_{dc}$ )	$K_p = 1, K_i = 250$
	PI ( $i_d, i_q$ )	$K_p = 0.7, K_i = 50$
BESS	Power, Frequency	$1.2 \text{ MVA}, 60 \text{ Hz}$
	Voltage (line-line)	$480 \text{ V (RMS)}$
	Ramp Rate	0.2 p.u./s
	$C_f, L_f$	$2 \text{ mF}, 100 \mu\text{H}$
	PR	$K_p = 2, K_r = 100$
	$\eta_{charge}$ (dc/ac)	96.5%
	$\eta_{discharge}$ (ac/dc)	96.5%
Battery	Power, Capacity	$1 \text{ MW} / 0.25 \text{ MWh}$
	Voltage	$1600 \text{ V}$
	Cells (series $\times$ parallel)	$441 \times 7$
	$C_{ts}, R_{ts}$ (per cell)	$440.57 \text{ F}, 2 \text{ m}\Omega$
	$C_{tl}, R_{tl}$ (per cell)	$17111 \text{ F}, 4.2 \text{ m}\Omega$
	$R_s$ (per cell)	$1.3 \text{ m}\Omega$
	$Q_c$ (represents Ah)	$160 \text{ F}$